Title
Rational Design and Fundamental Studies of Nanomaterials-Microorganism Hybrid Systems for Solar Energy Conversion

Author
Zhang, Hao

Publication Date
2019

Peer reviewed|Thesis/dissertation

Rational Design and Fundamental Studies of Nanomaterials-Microorganism Hybrid Systems for Solar Energy Conversion

by

Hao Zhang

A dissertation submitted in partial satisfaction of the

requirements for the degree of

Doctor of Philosophy

in

Chemistry

in the

Graduate Division

of the

University of California, Berkeley

Committee in charge:

Professor Peidong Yang, Chair

Professor Gabor A. Somorjai

Professor Junqiao Wu

Rational Design and Fundamental Studies of Nanomaterials-Microorganism Hybrid Systems for Solar Energy Conversion

by

Hao Zhang

Abstract

Rational Design and Fundamental Studies of Nanomaterials-Microorganism Hybrid Systems for Solar Energy Conversion

by

Hao Zhang

Doctor of Philosophy in Chemistry

University of California, Berkeley

Professor Peidong Yang, Chair

The subject of this dissertation focuses on designing biohybrid systems for efficient solar-fuel conversion. As the unlimited energy source for the ecosphere, solar energy could be captured *via* various devices to meet the rising demand on Earth's energetic hungry. Among all efforts, solar-driven conversion of carbon dioxide to value-added multi-carbon products is an ambitious objective, which recycles the waste CO_2 back into useful chemicals as the energy fuel, polymer, and pharmaceutical precursor. However, pure inorganic CO_2 (photo)electrocatalysts suffer from low selectivity, high overpotential, and poor mass transfer. Therefore, we proposed integrating inorganic semiconducting nanomaterials that harvesting solar energy with biological organisms to microbial fix CO_2 into target product. By taking advantage of solar energy harvesters, the metabolic pathway in the living organism is essentially powered by solar energy. This work herein explores the novel nanomaterial-biological photosynhtetic biohybrid system for efficient artificial photosynthesis, as well as cytoprotective strategy for further developments. Additionally, elucidation of charge transfer mechanisms at abiotic-biotic interface remains challenge, and this work delves into model system to probe the possible charge transfer process.

Chapter 1 introduces a brief history of new emerging biohybrid system. The diversity of possible biohybrid architectures has been thoroughly discussed, depicting the microorganisms coupled with photovoltaic devices, interfaced with photoelectrodes, and membrane-bound photocatalysts. The synergistic biohybrid design is capable to address the grand challenges for the efficient generation of solar fuels and chemicals. In parallel, the living anaerobe with less oxidative stress tolerance has been carefully treated with various cytoprotective strategies. To get insight of modern nano-biotechnology, the current progress on energy transfer mechanism and the challenges associated with this technology has been examined.

Chapter 2 presents one type of biohybrid system with gold nanoclusters as the photosensitizers. Gold nanocluster with discrete energy levels is regard as the light absorber, and translocation of these gold nanoclusters into nonphotosynthetic bacteria, *Moorella thermoacetica*, enabled photosynthesis of acetic acid from CO_2. Due to the small-size, gold nanocluster enables strong

direct interface between organism, which could circumvent the sluggish kinetics of electron transfer for existing biohybrid systems. Besides, biocompatible gold nanoclusters also serve as reactive oxygen species inhibitors to maintain high bacterium viability, realizing CO_2 fixation continuously over several days.

Chapter 3 introduces a uniformly cyprotective strategy for anaerobes using metal-organic framework (MOF) monolayer. Biohybrid system has recently being taken as a promising approach to sustainable energy. Among these chemical-producing microbes are anaerobic bacteria, inherently susceptible to O_2 and reactive oxygen species that are inevitably generated on anodes. *Moorella thermoacetica* as the strict anaerobic bacteria was dynamically wrapped by single MOF layer. The high definition of the MOF-bacteria interface involves direct bonding between phosphate units on the cell surface and zirconium clusters on MOF monolayer, enabling cell elongation and separation. The catalytic activitly of MOF enclosure toward decomposition of reactive oxygen species reduces the death of bacteria by fivefold.

Chapter 4 discusses the possible electron transfer process based on the work in chapter 2. The excited states behavior of gold nanoclusters attracts more and more attention due to their vast applications in artificial photosynthesis. The influence of charge-state on the cluster was studied by transient absorption spectroscopy, and interesting correlation between the core-gold and shell-gold relaxation was observed. The long-lived excited states components have been identified as ligand-to-metal transfer of gold nanoclusters with two different sizes. Their photocatalytic activity was evidenced from the electron transfer to methyl viologen. The elucidation of excited states and transfer process in model system could facilitate the understanding of complex biohybrid system.

To my parents and Ziang

Table of Contents

List of Figures and Tables
Acknowledgment

Chapter 1. Introduction

Section 1.1 Abiotic and biotic approaches for artificial-photosynthesis……...1
Section 1.2 Integrated photoelectrochemical cell with microbes…….....2
Section 1.3 Coupling inorganic photocatalysts with living cells…….....3
Section 1.4 Cytoprotected hybrid systems with high O2 tolerance…….....5
Section 1.5 Electron transfer pathway at biotic-abiotic interface…….7
Section 1.6 Conclusions……9
Section 1.5 References……9

Chapter 2. Intracellular Au nanocluster photosensitized bacteria for solar fuel production

Section 2.1 Abstract……12
Section 2.2 Introduction……13
Section 2.3 Experimental details……13
Section 2.3.1 Au nanoclusters synthesis……13
Section 2.3.2 Growth of *M. thermoacetica*/Au NCs ……..15
Section 2.3.3 Photosynthesis measurements……16
Section 2.3.4 Viability and ROS assay test……..16
Section 2.3.5 Microscope sample preparations……17
Section 2.4 Results and discussion……17
Section 2.4.1 The characterization of intracellular biohybrid system……17
Section 2.4.2 Photosynthesis of *M. thermoacetica*/Au nanoclusters hybrid system …….20
Section 2.4.3 Cell viability characterization……28
Section 2.5 Conclusions……29
Section 2.6 References……30

Section 3. Cytoprotective Metal-Organic Frameworks for Anaerobic Bacteria

Section 3.1 Abstract……33
Section 3.2 Introduction……..33
Section 3.3 Experimental details……34
Section 3.3.1 Synthesis of MOF monolayer $Zr_6O_4(OH)_4(BTB)_2(OH)_6(H_2O)_6$……..34
Section 3.3.2 Anaerobic bacteria culturing……35
Section 3.3.3 Wrapping MOF monolayer around *M. thermoacetica* ……35
Section 3.3.4 Physical and chemical characterization……35
Section 3.3.5 Oxidative stress and cell viability test……36
Section 3.3.6 Photosynthesis characterization……37
Section 3.4 Results and discussion……...37
Section 3.4.1 Wrapping structural characterization of MOF-bacteria system……..37
Section 3.4.2 Cell viability characterization of MOF-bacteria system……..41
Section 3.4.3 Mechanism of cytoprotective property……43
Section 3.5 References……47
Appendix……50

Section 4. Ultrafast Studies of Photoinduced Excited States of Au Nanocluster in Model System

Section 4.1 Introduction……..55
Section 4.2 Experimental details……..55
Section 4.2.1 Au nanoclusters synthesis ……55
Section 4.2.2 Au nanoclusters characterization……..56
Section 4.2.3 Femtosecond and nanosecond transient absorption setup……57
Section 4.3 Results and discussion……57
Section 4.3.1 Ultrafast excited states of $Au_{22}(SG)_{18}$……..57
Section 4.3.2 Photoinduced electron transfer within $Au_{22}(SR)_{18}$ ……..62
Section 4.3.3 Excited states properties of $Au_{18}(SR)_{14}$……64
Section 4.4 Conclusions……66
Section 4.5 References……66

List of Figures and Tables

Chapter 1

Fig. 1.1 The configuration of PEC biohybrid systems……3
Fig. 1.2. Phorocatalyst based biohybrid systems. ……...……4
Fig. 1.3. Metal–Organic Frameworks as the cytoprotective layers for living cells……..…6
Fig. 1.4 Silica-encapsulation cytoprotective shell for anaerobes…….6
Fig. 1.5. Wood-Ljungdahl pathway and involved proteins with their subcellular locations……..7
Fig. 1.6. The spectroscopic studies of biohybrid system……...…….8

Chapter 2

Fig. 2.1. The schematic diagram of the *M. thermoacetica*/Au NCs hybrid system……..12
Fig. 2.2. Purification of $Au_{22}(SG)_{18}$ NCs *via* polyacrylamide gel electrophoresis……14
Fig. 2.3. The characterization of *M. thermoacetica*/Au NCs hybrid system and deletional controls……..…16
Fig. 2.4. The microscopy images of the *M. thermoacetica*/Au NCs hybrid system……..19
Fig. 2.5. SIM images of deletional controls……...20
Fig. 2.6. ^{1}H-NMR and ^{13}C-NMR spectra of acetate labeled with ^{13}C……..21
Fig. 2.7. Photosynthesis behavior of different systems……23
Fig. 2.8. The acetyl-CoA pathway as resolved from *M. thermoacetica*……..25
Fig. 2.9. Stability of Au NCs and intracellular Au NCs……..28
Fig. 2.10. The viability measurements……29
Table 2.1. Wolfe's Vitamin Mix……..15
Table 2.2. Trace Mineral Mix……..15
Table 2.3. Components of the ET chain and their subcellular locations in *M. thermoacetica*. ……24

Chapter 3

Fig. 3.1. Design and synthesis of the *M. thermoacetica*-MOF wrapping system……..38
Fig. 3.2. Structural characterization of *M. thermoacetica*-MOF……..39
Fig. 3.3. SEM images of *M. thermoacetica*-MOF..……..39
Fig. 3.4. Optical characterization of MOF wrapping systems……..40
Fig. 3.5. Structural characterization of *M. thermoacetica*-MOF……..41
Fig. 3.6. MOF monolayer enclosure allows for the reproduction of bacteria……..42
Fig. 3.7. MOF monolayer enhances the bacteria viability under oxidative stress.……..43
Fig. 3.8. The mechanism of protection against oxidative stress by MOF enclosure.……..44
Fig. 3.9. Kinetics of H_2O_2 decomposition catalyzed by MOF monolayer..……46
Fig. 3.10. The Yield of acetate in the half photosynthetic reaction……47

Chapter 4

Fig. 4.1. Optical properties of $Au_{22}(SR)_{18}$……...58
Fig. 4.2. Electrospray ionization mass spectrometry (ESI-MS) spectrum of $Au_{22}(GS)_{18}$……59
Fig. 4.3. The time-resolved PL spectrum of $Au_{22}(SR)_{18}$ at 630 nm……59
Fig. 4.4. The fsTA spectra mapping……..……...60
Fig. 4.5. Absorption-time profile at different wavelength. ……..……61
Fig. 4.6. Pump power-dependent electron dynamics of $Au_{22}(SR)_{18}$ power dependent spectra…62
Fig. 4.7. $Au_{22}(SR)_{18}$ nsTA spectra……..…….....62
Fig. 4.8. The scheme of possible electron transfer process between AuNCs and MV^{2+}…….....63
Fig. 4.9. nsTA map of $Au_{22}(SR)_{18}$ and $Au_{22}(SR)_{18}$ with MV^{2+} systems……..…….....64
Fig. 4.10. nsTA spectra of $Au_{22}(SR)_{18}$ and MV^{2+} systems.……..…….....64
Fig. 4.11. nsTA spectra of $Au_{18}(SR)_{14}$……..…….....65

Acknowledgements

I would first like to thank my advisor Professor Peidong Yang for the opportunity to work with him in the past few years. Your guidance and mentorship has made me a better and more thoughtful researcher. Science was like a lighthouse standing far away from me, and I was like a boat floating on the sea when I started my journal at UC Berkeley. It is you who helped me build up my courage to overcome barriers when I tried to approach my destination. Your enthusiasm for science over your extensive career is a constant source of inspiration for me going forward. Critical thinking is one of the best treasure I have got from you, and all your help is gratefully appreciated.

I would also like to thank Professor Omar Yaghi for his support. I collaborated with his group on the metal-organic-framework, expanding my research background and interests. His patient guidance to students and hands-on mentorship impressed me. For other faculty members, I am also deeply grateful to Professor Gabor Somorjai for being my qualify-exam chair, and his keen interest and passion in science motivated me to always strive further in approaching scientific problems. I would also want to express my gratitude to Professor Kristie Boering and Professor Junqiao Wu for being my qualify-exam committee members.

I am always grateful for working with so many incredibly talented and friendly researchers at UC Berkeley. I am thankful to Dr. Joaquin Resasco, and Dr. Kelsey K. Sakimoto for being me mentor on photoelectrochemistry and biological reduction. Mr. Zhe Ji collaborated with me on the cytoprotective project, and his endless energy to explore scientific issue inspired me. Dr. Hao Liu taught me the synthesis of gold nanoclusters, and Dr. Yi Yu always helped me with the TEM characterization. I want to thank Dr. Dylan Lu for his help on PL and transient absorption measurements. Dr. Nigel Becknell and Dr. Chenlu Xie helped a lot on the experiments at Advanced Light Source, and we have spent many day and night shifts for the experiments together with Mr. Qiao Kong. To Dr. Yude Su, Dr. Yuexiao Shen, Stefano Cestellos-Blanco, Minliang Lai, thank you for being my great labmates. The time I spent working with all of you has made my graduate research enjoyable and educational, and I wish you all the best in the future.

To all of my friends, both the ones I made in Berkeley, and my friends from home, thank you for being there.

I would not be here were it not for my wonderful family. I owe my greatest gratitude to my parents for their unfailing support and love. To my mom, thank you for your selfless love and guidance when I was lost. To my dad, you are my role model and thank you for all your support. Back to my undergraduate, it was my fortunate to meet Ziang, the love of my life. He is extraordinary supportive, encouraging, and considerate, sharing all my happiness and sadness. As he said ‘you are my sunshine’ when proposed, I would say you are the one who always cheer me up and delight my life. I look forward to a life of adventures with you.

Chapter 1. Introduction

Section 1.1 Abiotic and biotic approaches for artificial-photosynthesis

With the increasing human population, the finite food and fossil fuels challenge the world to develop the technologies to address this issue. The indiscriminate utilization of fossil fuels causes the significant harmful effects on the environment, such as water pollution, and large quantity green-house gas emission. Besides being the main driver for climate changes, CO_2 is also a renewable resource and a major carbon source for living organism. Therefore, sustainable and economically converting CO_2 into fuel and other target chemicals with renewable energy source has become one of the main current technology topics. In terms of the renewable energy, sunlight radiation density on the surface of earth is approximately 1.4 kw/m^2, providing the abundant energy to multiple systems[1]. Indeed, the natural photosynthesis powers the plants or photosynthetic microorganisms by converting the solar energy into hole and electron equivalents in the form of adenosine triphosphate (ATP) and nicotinamide adenine dinucleotide phosphate (NADPH) *via* Calvin cycle, which combined with CO_2 to provide carbohydrates[2]. However, these systems suffer from the low solar-to-energy conversion efficiency, where most plants have less than 1% annual conversion and microalgae in bioreactors with ~3% conversion[3]. Therefore, designing the platform that efficient harness the sunlight galvanizes the generation of artificial photosynthesis.

Compared to the natural biological photosynthesis, light absorption materials employed photoelectrochemical (PEC) cell and solid-state photovoltaic (PV) own higher solar-to-fuel conversion efficiency. To date, the solar-to-hydrogen efficiency of photoelectrochemical cells from 12.4 % for a tandem cell and 18% for a multijunction cell has been achieved[4-6]. In the meanwhile, the solar-to-electricity efficiency of photovoltaic cells can be high to 46% for GaInP/GaAs multijunction cells[7,8]. As for the CO_2 reduction, photoelectrochemical reactor developed till now for this purpose produced mostly C_1 compounds such as carbon monoxide, methane, methanol and formate[9.10]. In this regard, the natural photosynthesis producing broad long chain carbon molecules with high selectivity is superior than completely material-based artificial PEC cells[11-13]. Thus, the inorganic material and microorganism hybrid systems(PBSs) emerges for selective fixing CO_2 into multicarbon products with high solar-to-fuel conversion efficiency[14-24].

The photosynthetic biohybrid systems profit the metabolic versatility of microorganisms and the efficiency of inorganic light harvesting devices or materials. An alternative benefit of PBS is that it could enable the nonphotosynthetic microorganism to utilize the solar energy, expanding the applicable microbe library. In addition, the availability of genetically technology, could facilitate the rational design of target chemicals. Particularly, the metabolic products encompass fuel, polymer, C_2-C_5 alcohols, and the pharmaceutical precursors [25, 26].

Therefore, thoroughly discussion on recent advances made in the field of photosynthetic biohybrid systems benefits expanding the application of such systems in the near future. This introduction will place an emphasis on the evolution of PBSs with diversified architectures, depicting the microorganisms coupled with photovoltaic devices, interfaced with photoelectrodes, membrane-bound photocatalys, and intercellular photosensitizers. In order to get better insight of modern nano-biotechnology, the possible energy transfer mechanism and the challenges associated with this technology have been examined.

Section 1.2 Integrated photoelectrochemical cell with microbes

The generation of PEC cell, normally with photoanode and photocathode, aims for solar-driven oxidation and reduction reaction, respectively. The electro-microorganism hybrid systems could be achieved that directly incorporate microorganism on the electrodes or indirectly submerge the electrode into microorganism culture[16, 27]. This work relies on the ability of electrotrophic bacteria to take up reducing equivalents from inorganic sources, including electrons or H_2. These organisms are commonly paired with a cathode in photoelectrochemical systems where they consume electrons to power the conversion of CO_2 into upgradeable carbon products. Exemplarily, acetogens receive reducing equivalents from solar harvesting electrodes and secrete acetate as a by-product of CO_2 fixation. Liu and coworkers have developed the functional PEC biohybrid system, where CO_2 was reduced to n-butanol, isoprenoids, and polymers as shown in Fig. 1.1b[13]. The light-absorbing Si nanowires as photocathode was separated by the cation-exchange membrane from photoanode TiO_2, consisting a complete PEC cell. Several modifications of high-aspect-ratio Si nanowires had been carried out, such as, heavily doped n^+ layer to improve photovoltage, a thin TiO_2 passivation layer deposition to increase the stability, and a Ni and Pt layer as the cocatalysts to accelerate charge transfer. The acetogen *Sporomusa ovata* (*S. ovata*), as the well-studied microorganism reducing CO_2 into acetate, was selected as the microbial catalysts and injected into the photocathode chamber [28,29]. Due to the weak electron flux from photocathode, *S. ovata* moves freely to the Si nanowire surface for such energy source, forming a biofilm between the inorganic nanowire surface and cell membrane. With the directed nanowire-bacteria interface, there is the chance for *S. ovata* to obtain the electrons directly from photocathode or indirectly from the generated H_2 during the hydrogen-evolution-reaction (HER) process. Under simulated sunlight, nanowire-bacteria biohybrid system was stable to fix CO_2 with a photocurrent of 0.3 mA/cm^2 for 120 h, where the solar energy to acetate efficiency is around 0.38%. Such collected acetate was further used as the feedstock to *Escherichia coli* (*E. coli*) in the downstream bioprocess to build up value chemicals with longer carbon chains. However, the bio-inorganic interface varies in different electrodes configuration, and therefore, systematically study the biohybrid interface spread the new photosynthetic applications and could improve the overall solar energy conversion efficiency.

Besides the combination of direct electron charge transfer and H_2, purely H_2 as efficient energy source was achieved by splitting water into molecular hydrogen and oxygen (H_2 and O_2) at low driving voltages. Such process involves a biocompatible earth-abundant inorganic catalyst system, where current density could be high to 8 mA/cm^2. The employed reactive-oxygen-species resistant cobalt-phosphorus (Co-P) alloy cathode could drive the HER with a faradic efficiency of $99 \pm 2\%$. The *Ralstonia eutropha* (*R. eutropha*) consumed the produced H_2 to synthesize biomass and fuels or chemical products from low CO_2 concentration. A ~50% CO_2 reduction efficiency of producing biomass and liquid fusel alcohols reveals the potential in scaling up such biohybrid systems. When coupled biohybrid device to photovoltaic systems, the solar-to-energy conversion efficiency is up to ~10%, far above the natural photosynthesis efficiency[16].

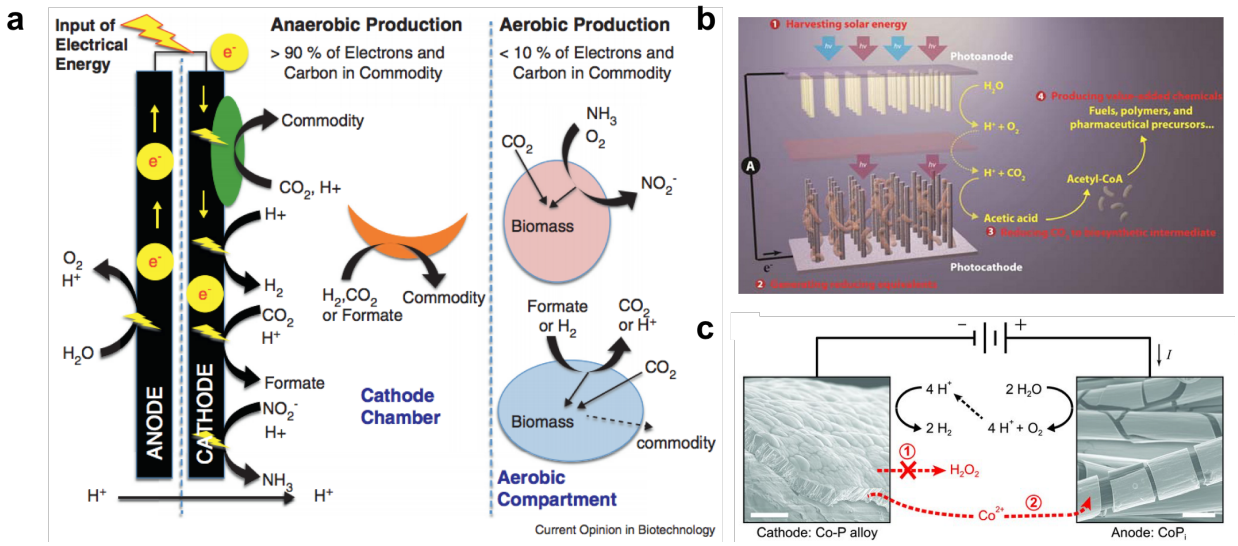

Fig. 1.1. The configuration of PEC biohybrid systems. a. PEC based biohyrbid system where cathode could pump energy source to microbes[19] (Copyright © 2013 Elsevier Ltd.). **b.** Si nanowires as photocatode incorporated with *S. ovata* for CO_2 reduction, and the generated acetate used as the feedstock for the following genetic engineered *E. coli* to achieve C_3-C_5 products[13] (Copyright © 2015 American Chemical Society). **c.** Water splitting based electrochemical biohybrid system, and the generated H_2 boosts the overall energy conversion efficiency to ~10 % with long stability[16] (Copyright © 2016 American Association for the Advancement of Science).

While these efforts confirm the applicability of PEC biohybrid systems, the emerging systems are still at an early stage of development. The using of whole cell as the microbial catalysts suffers from the low productivity and weak interface, and further improvement on the interface between the cell membrane and electrode could assist the overall efficiency. For instance, it is important to increase the CO_2 reducing current while at the same time maintaining a stable interface between the cells and the cathode. Whereas, increasing the CO_2 reducing current is hampered by the fact that high currents create a local basic environment around the proton-consuming cathode. The cell-semiconductor interface could be irreparably damaged with basic local environment. Moreover, the challenge that optimizing the biocompatible photocathodes for both sunlight capture and suitable electron transfer must be overcame to attain the practical systems.

Section 1.3 Coupling inorganic photocatalysts with living cells

Instead of coupling the living cells with electrodes in the whole PEC setup, the photocatalytic reducing CO_2 into value-added products with more simple reaction cells attracts more and more attention. Recently, Sakimoto and coworkers have developed two biohybrid photosynthetic systems comprising phtocatalyst nanoparticles driving the microbial reduction of CO_2 into multi-carbon products. *Moorella thermoacetica* (*M. thermoacetica*), an acetogen mainly

reducing CO_2 into acetate, was employed as the microbial catalysts. In this biohybrid system, the energy source to drive autotrophic metabolism of *M. thermoacetica* came from the semiconductor CdS nanoparticles under illumination, where the photogenerated electrons were passed onto Wood–Ljungdahl pathway (WLP)[15]. The CdS nanoparticles were self-precipitated by bacteria with released S^{2-} in the culture media, and membrane-bound to the cell surface. The overall reaction could be regard as the half reaction with hole scavengers, and the leftover photogenerated holes oxidize the redox mediator cysteine to cystine. The photocatalytic biohybrid system generates ~1.2 mM acetic acid in 2.5 days under low-intensity-simulated sunlight. Moreover, the same authors have improved their system to the full reaction with CO_2 reduction and oxygen generation reaction[17]. On the photoanode side, TiO_2 nanoparticles coated with manganese(II) phthalocyanine (MnPC) as the cocatalyst oxidized the water into O_2, where cysteine as the redox mediators. The "Z-scheme" architecture was formed between TiO_2 nanoparticles and living cell that with membrane-bound CdS. Due to the generated oxygen, the *M. thermoacetica,* a type of anaerobic bacterium, can only partially survive with low viability, resulting the overall 0.6 mM acetic acid within half a day of illumination. Compared with the PV and PEC based biohybrid systems, the photocatalysts biohybrid system is easily achieved in half reaction with low productivity. However, in terms of the cost and setup requirements, this approach appears the significant advantages.

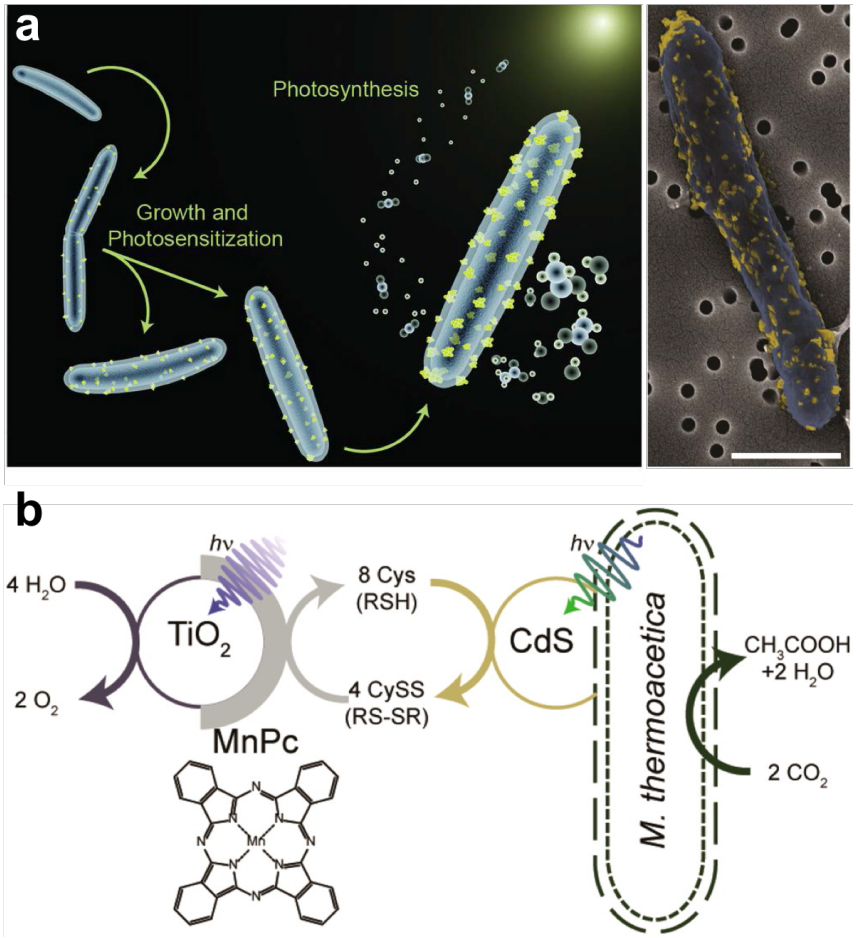

Fig. 1.2. Phorocatalyst based biohybrid systems. a. Membrane-bound CdS as the photosensitizer to drive the microbial CO_2 reduction, *M. thermoacetica* reduced CO_2 into acetate with electrons from CdS (Copyright © 2016 American Association for the Advancement of Science). **b**. In a tandem system with Z scheme strategy, water is oxidized by TiO_2 photocatalyst. Electrons are transferred from TiO_2 to cystine via a MnPC cocatalyst. The resulting cysteine is then oxidized by a CdS photocatalyst (Copyright © 2016 American Chemical Society).

Section 1.4 Cytoprotected hybrid systems with high O_2 tolerance

Anaerobic bacteria have long been bred and used for fermenting organic matter in the absence of O_2 to produce value-added chemicals (ethanol, acetic acid, lactic acid, acetone, and butanol)[30]. The above biohybrid systems call for the usage of anaerobic living cell, for instance, the *S. ovata*, *M. thermoacetica*, and *R. eutropha* who belong to anaerobes. Therefore, the evolution of O_2 and reactive oxygen species (ROS) at the reaction chamber along with fuel generation are detrimental to the metabolism of anaerobic bacteria. The strategy to overcome such inherent vulnerability could expand the application of biohybrid systems, and implement a full artificial photosynthesis.

It is known that bacteria can be coated with polymers, inorganic nanoparticles, and MOFs to enhance their viability under radiation, thermal, and mechanical stress[31-37] . Liang and coworkers have worked on metal-organic-frameworks (MOFs) materials to protect yeast. MOFs are an emerging class of porous materials, that is biocompatible and robust building blocks. The supreme thermal and chemical stability enable them to facilitate the CO_2 gas absorption, electro catalysts under harsh conditions. As shown in Fig.1.3a. the biomolecule-rich cell membranes and walls could concentrate MOF precursors, proving an active interface for the crystallization of MOF. Thus, a porous exoskeleton encasing living cells has been formed. The authors have demonstrated the viability of cells to assess the bimcompability of MOF. Remarkably, the coated MOF could control the molecular diffusion to the cell cytoplasm, and prevent cell division to prolong the overall lifetime under extreme environment.

Another strategy biomimetic silica encapsulation that base on layer-by-layer (LBL) could create locally anaerobic environment, which has been widely used for the surface modification of living organisms[38]. The study of CdS–*E. coli* verified the concept of photosynthetic biohybrid system, where photocatalytic produced hydrogen under aerobic conditions by cells self-aggregation. In order to continuously generate H_2, the *E. coli* cells were coated with cationic polyelectrolyte poly (diallyldimethylammonium chloride) (PDADMAC) and anionic polyelectrolyte sodium polystyrene sulfonate (PSS), and then placed into silicic acid to form the silica-encapsulation. The encapsulated cells could gradually consume oxygen through aerobic respiration, consequently producing an anaerobic environment for the *E. coli* in the core. However, such modification suffers from complicated synthetic procedure that yields either poor coverage or stiff shells of hundreds of nanometers in thickness, which trap cells in dormant state. As such, the protection provided by these materials is only temporary as the material coating needs to be repeated every time a new batch of cells is introduced.

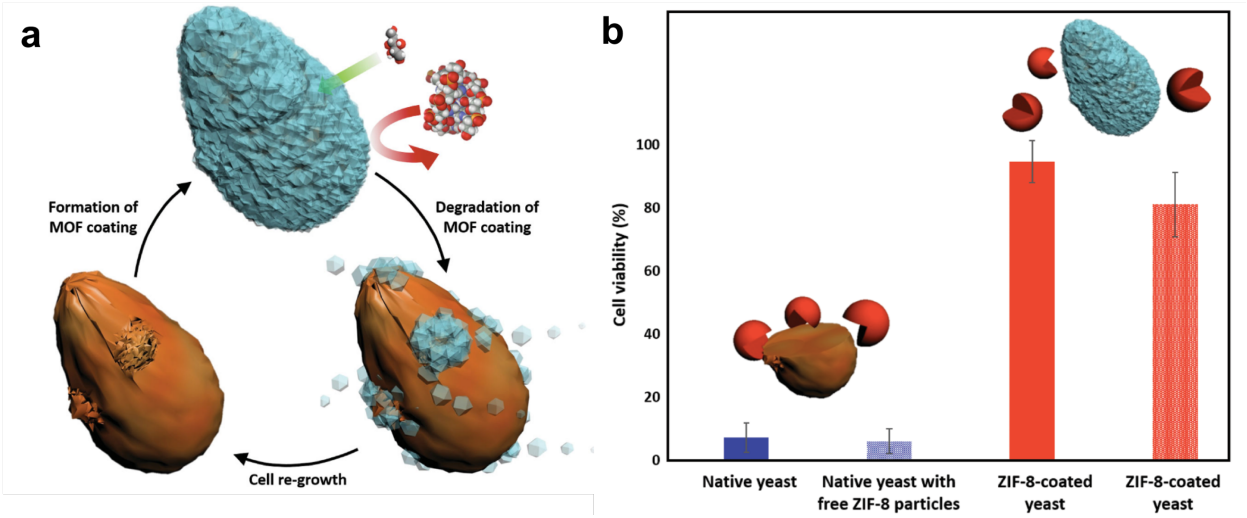

Fig. 1.3. Metal–Organic Frameworks as the cytoprotective layers for living cells. a. Schematic illustration of biomimetic crystallization of cytoprotective MOF coatings on living cells. **b.** The cell viability (%) of native yeast (blue) and native yeast with free ZIF-8 particles (patterned blue) in the presence of cell lysis enzyme lyticase for 3 h, and ZIF-8 coated yeast in the presence of lyticase for 3 h (red) and 24 h (patterned red), indicating the coating improve the cell viability under harsh environment[32] (Copyright © 1999-2019 John Wiley & Sons, Inc).

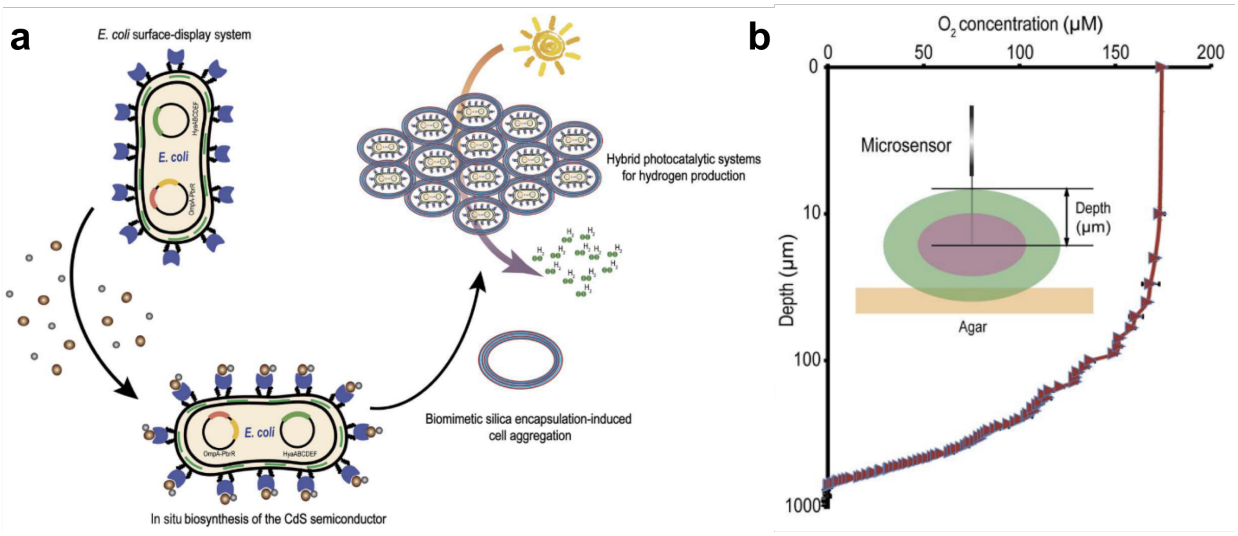

Fig. 1.4 Silica-encapsulation cytoprotective shell for anaerobe. a. The proposed surface-display biohybrid system for light-driven hydrogen evolution in air, where the *E. coli* encapsulated in the silica shell for anaerobic condition. **b.** O_2 concentration measurements based on microsensor in the various independent encapsulated cell aggregates, and the O_2 amount sharply decreased after depth of 100 μm (adopted with permission from ref. 38, Copyright © 2018 The Authors, some rights reserved; exclusive licensee American Association for the Advancement of Science).

Section 1.5 Electron transfer pathway at biotic-abiotic interface

The photosynthetic bihybrid system is a less understood system, and thus, the electron transfer between inorganic light harvesting nanoparticles and/or electrodes and the living cell mechanism is worth exploring. Compared to the bare enzyme systems, the direct light/electrical energy through the living cells' metabolic pathway can yield a host of complex products. The electron transfer in the whole cell system is more complicated due to the involvements of various proteins and enzymes. Most anaerobic bacteria conserve energy by substrate-level phosphorylation from the metabolism of glucose *via* the glycolytic fermentation. During this process, a transmembrane gradient of H^+ and Na^+ could be used by a membrane-bound ATP synthase to synthesize triphosphate (ATP) from ADP and inorganic phosphate(Pi). The main electron-transport (ET) systems include several important enzymes, such as, ferredoxin, rubredoxin, flavoprotein, and methylene-H_4F-reductase, existing in membrane or cytoplasm[39-42]. They link the soluble and membrane bound ET systems, synergic involving the WLP process.

The electron transfer process between a poised electrode and electrotrophic bacteria have been investigated, while those studies are limited by the inability to replicate and observe the processes in situ by spectroscopic means. The thorough charge transfer mechanism is not fully deciphered, while two possible mechanisms have been well accepted, including (1) direct electron transfer from energy source (electrode/semiconductors) to redox-active units such as membrane-bound protein, (2) H_2 or other soluble mediators facilitated charger transfer. The first demonstration of direct electron transfer from electrode to microorganism was carried out by Thrash and Coates in 2008.

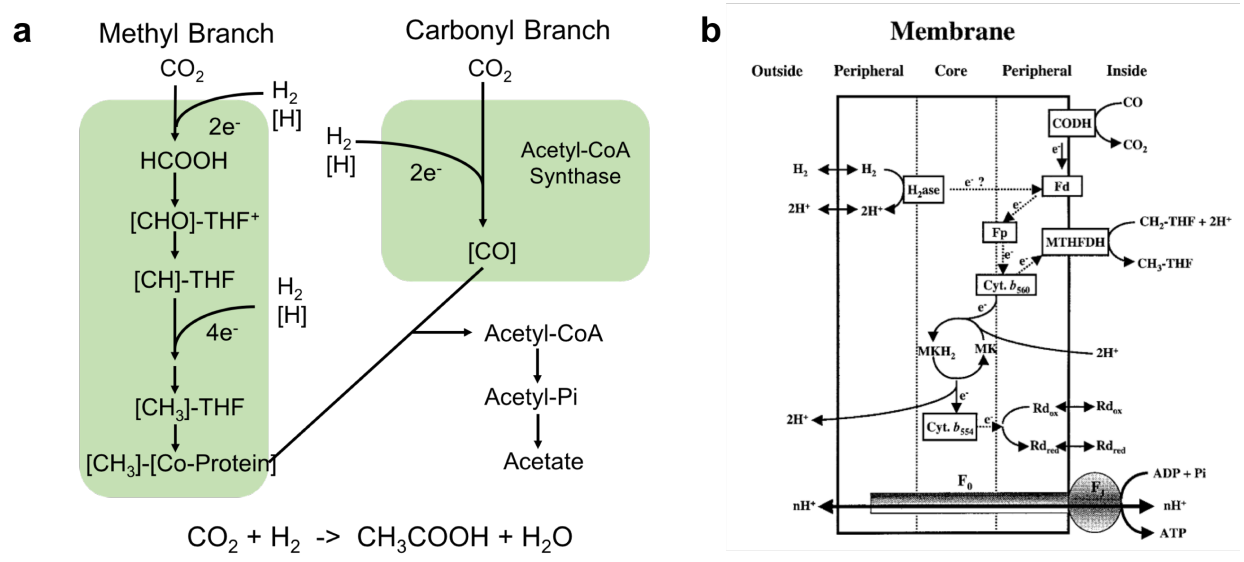

Fig. 1.5. Wood-Ljungdahl pathway and involved proteins with their subcellular locations[39]. (Copyright © 2003 Springer-Verlag New York, Inc.).

On the other hand, the photocatalyst biohybrid system has been studied *via* the spectroscopic tool. Nikolay and coworkers used the *M. thermoacetica*-CdS biohybrid system as the platform to undertake transient absorption (TA) and time-resolved infrared (TRIR) spectroscopy to elucidate the possible charge transfer[43]. Existing of hydrogenase (H_2ase), the photoinduced electrons from semiconductors are possible used by such membrane-bound H_2ase to product H_2, which, in turn, is utilized in the WLP to reduce CO_2 into acetate. Along the same line, some other membrane-bound proteins, like flavins and cytochrome, could serve as the electron acceptors in the metabolism process. The TA spectroscopy is the powerful tool to probe the excited states of semiconductors. By applying different H_2 incubation time, the excited charge carrier lifetime in biohybrid systems varies, as well as the photosynthetic acetic acid generation efficiency. Within the first 24 h of photosynthesis, the quantum efficiency of solar-to-fuel conversion increased with increasing H_2ase activity, resulting in shorter carrier lifetime in the meanwhile. However, the opposite trend that low H_2ase activity prompts the acetic acid generation has been observed. In samples with limited H_2ase activity, the electrons feed directly into membrane bound proteins accelerating acetate production but ultimately cannot sustain metabolic activity due to a lack of high energy reducing equivalents [H_2, NAD(P)H]. Whereas samples with sufficient H_2ase activity, a CdS-to-hydrogenase electron transfer pathway is established to produce high energy reducing equivalents. Based on two different trends related to enzyme activity, the authors proposed a two-pathway mechanism that matches well with previous direct and indirect charge transfer process.

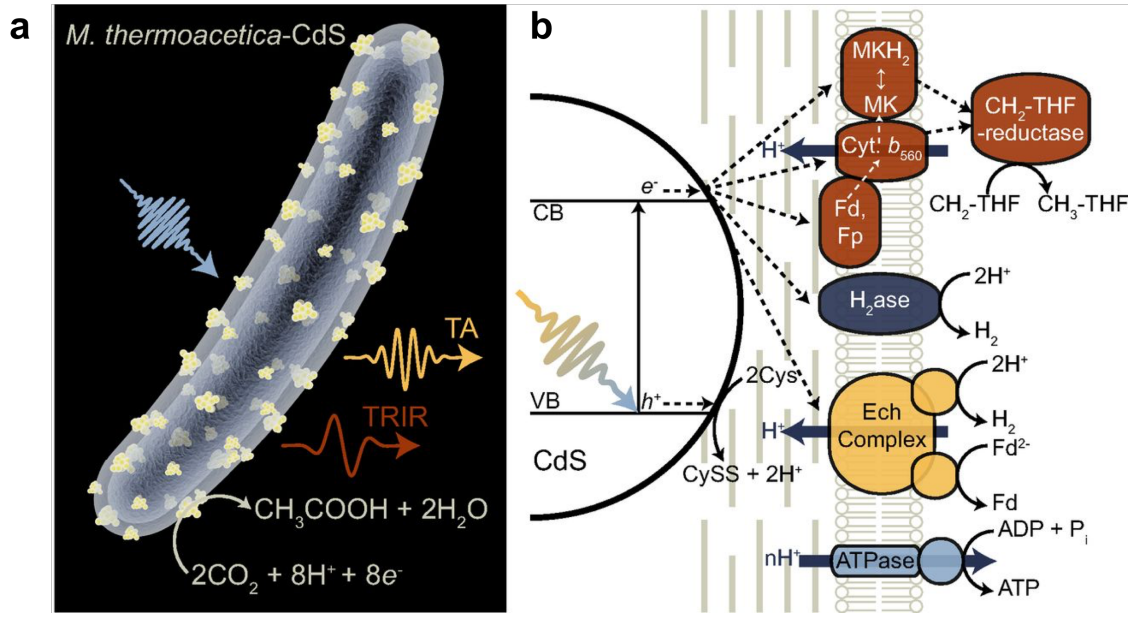

Fig. 1.6. The spectroscopic studies of biohybrid system. a. Conventional spectroscopy as the powerful tool to study the charge transfer process in photocatalyst biohybrid system. **b.** The proposed the direct electron transfer from CdS to the membrane-bound proteins, yet, this complex system is less understood compared to precise enzyme-quantum dots system[43] (Copyright © 2016 National Academy of Sciences).

Section 1.6 Conclusion

Photosynthetic biohybrid system is a novel technology still in its infancy, and after significant improvements in terms of efficiency, productivity, and stability, it could become the cost effective and universal strategy to solve the energy crisis. To address the issue of low efficiency, the biohybrid systems need seeking for the suitable light-harvesting inorganic materials with lots of optimization. Moreover, the synthetic biology approach could be carried out to accelerate the microbial catalytical reaction that reduces CO_2 into target products. In addition, understanding the charge transfer at biotic-abiotic interface is a key challenge that limits the photosynthesis efficiency. Model system that coupled inorganic nanomaterials and simple enzymes could be a good starting point to probe the inside charge transfer process, and thus, the spectroscopy spectra are capable to extract insights from such biohybrid systems for future investigation and improvements.

1.7 References

1. Lewis, Nathan S. Research opportunities to advance solar energy utilization. *Science.* **351**. 6271. aad1920 (2016).
2. Mallick, N., Bagchi, S. K., Koley, S., & Singh, A. K. Progress and challenges in microalgal biodiesel production. *Front. Microbiol*, ***7*****,** 1019 (2016).
3. Williams, P. Jl. B. & Laurens, L. M. L. Microalgae as biodiesel & biomass feedstocks: Review & analysis of the biochemistry, energetics & economics. *Energy Environ. Sci.* **3,** 554–590 (2010).
4. Green, Martin A., *et al.* "Solar cell efficiency tables (version 52)." *Progress in Photovoltaics: Research and Applications* **26.7**, 427-436 (2018).
5. Benick, Jan. *et al*. High-efficiency n-type HP mc silicon solar cells. *IEEE journal of photovoltaics* **7.5**, 1171-1175 (2017).
6. Yoshikawa, K. *et al.* Silicon heterojunction solar cell with interdigitated back contacts for a photoconversion efficiency over 26%. *Nature Energy*. **2.5,**17032 (2017).
7. NREL Press Release NR-4514, 16 December 2014.
8. Press Release, Fraunhofer Institute for Solar Energy Systems, 1 December 2014 (accessed at http://www.ise.fraunhofer.de/en/press-and-media/press-releases/press-releases-2014/new-world-record- for-solar-cell-efficiency-at-46-percent on 7 December 2014).
9. Barton, E. E., Rampulla, D. M., & Bocarsly, A. B. Selective solar-driven reduction of CO2 to methanol using a catalyzed p-GaP based photoelectrochemical cell. *J. Am. Chem. Soc.* ***130*****(20)**, 6342-6344 (2008).
10. Sahara, G. *et al.* Photoelectrochemical Reduction of CO_2 Coupled to Water Oxidation Using a Photocathode with a Ru (II)–Re (I) Complex Photocatalyst and a CoO_x/TaON Photoanode. *J. Am. Chem. Soc.* ***138*****(42)**, 14152-14158 (2016).
11. Wu, N. Plasmonic metal–semiconductor photocatalysts and photoelectrochemical cells: a review. *Nanoscale* **10.6**, 2679-2696 (2018).
12. Ma, S., & Kenis, P. J. Electrochemical conversion of CO_2 to useful chemicals: current status, remaining challenges, and future opportunities. *Curr Opin Chem Eng*. ***2*****(2),** 191-199 (2013).

13. Liu, C., Gallagher, J. J., Sakimoto, K. K., Nichols, E. M., Chang, C. J., Chang, M. C., & Yang, P. Nanowire–bacteria hybrids for unassisted solar carbon dioxide fixation to value-added chemicals. *Nano Lett.* ***15*****(5),** 3634-3639 (2015).
14. Sakimoto, K. K., Kornienko, N., Yang, P. Cyborgian material design for solar fuel production: the emerging photosynthetic biohybrid systems. *Acc Chem Res*. **50,** 476–81 (2017).
15. Sakimoto, K. K, Wong, A. B., Yang, P. Self‐photosensitization of nonpho‐ tosynthetic bacteria for solar‐to‐chemical production. *Science.* **351,** 74–7 (2016).
16. Liu, C., Colón, B. C., Ziesack, M., Silver, P. A., & Nocera, D. G. Water splitting–biosynthetic system with CO_2 reduction efficiencies exceeding photosynthesis. *Science*, **352,** 1210–1213 (2016).
17. Sakimoto, K. K, Zhang, S. J., Yang, P. Cysteine–cystine photoregeneration for oxygenic photosynthesis of acetic acid from CO_2 by a tandem inorganic‐biological hybrid system. *Nano Lett.* **16,** 5883–7 (2016).
18. Lovley, D. R. Powering microbes with electricity: Direct electron transfer from electrodes to microbes. *Environ. Microbiol. Rep.,* **3,** 27–35 (2011).
19. Lovley, D. R., Nevin, K. P. Electrobiocommodities: powering microbial pro‐ duction of fuels and commodity chemicals from carbon dioxide with electricity. *Curr Opin Biotechnol.* **24,** 385–90 (2013).
20. Nevin, K. P., Woodard, T. L., Franks, A. E., Summers, Z. M., & Lovley, D. R. Microbial electrosynthesis: feeding microbes electricity to convert carbon dioxide and water to multicarbon extracellular organic compounds. *MBio*, *1*(2), e00103-10 (2010).
21. Tremblay, P. L., & Zhang, T. Electrifying microbes for the production of chemicals. *Front Microbiol.* ***6*****,** 201 (2015).
22. Gong, Y., Ebrahim, A., Feist, A. M., Embree, M., Zhang, T., Lovley, D., & Zengler, K. Sulfide-driven microbial electrosynthesis. *Environ Sci Technol*. ***47*****(1),** 568-573 (2012).
23. Tremblay, P. L., Höglund, D., Koza, A., Bonde, I., & Zhang, T. Adaptation of the autotrophic acetogen Sporomusa ovata to methanol accelerates the conversion of CO_2 to organic products. *Sci Rep*. ***5*****,** 16168 (2015).
24. Bose, A., Gardel, E. J., Vidoudez, C., Parra, E. A., & Girguis, P. R. Electron uptake by iron-oxidizing phototrophic bacteria. *Nat Commun,* ***5*****,** 3391 (2014).
25. Lee, S. Y. *et al.* A comprehensive metabolic map for production of bio-based chemicals. *Nat. Catal.* ***2*****(1),** 18 (2019).
26. Rudroff, F., Mihovilovic, M. D., Gröger, H., Snajdrova, R., Iding, H., & Bornscheuer, U. T. Opportunities and challenges for combining chemo-and biocatalysis. *Nature Catalysis*, ***1*****(1),** 12 (2018).
27. Zhang, T., & Tremblay, P. L. Hybrid photosynthesis-powering biocatalysts with solar energy captured by inorganic devices. *Biotechnology for biofuels*, ***10*****(1),** 249 (2017).
28. Chen, L., Tremblay, P. L., Mohanty, S., Xu, K., & Zhang, T. Electrosynthesis of acetate from CO 2 by a highly structured biofilm assembled with reduced graphene oxide–tetraethylene pentamine. *J. Mater. Chem. A*. ***4*****(21),** 8395-8401 (2016).
29. Zhang, T. *et. al.* Improved cathode materials for microbial electrosynthesis. *Environ Sci Technol,* ***6*****(1),** 217-224 (2013).
30. Zeikus, J. G. Chemical and fuel production by anaerobic bacteria. *Ann Rev Microbiol*, ***34*****(1),** 423-464 (1980).

31. Ai, H., Fang, M., Jones, S. A., Lvov, Y. M. Electrostatic layer-by-layer nanoassembly on biological microtemplates: platelets. *Biomacromolecule.* **3,** 560-564 (2002).
32. Liang, K. *et al.* Metal–organic framework coatings as cytoprotective exoskeletons for living cells. *Adv Mater.* **28,** 7910-7914 (2016).
33. Liang, K., *et al.* An enzyme-coated metal–organic framework shell for synthetically adaptive cell survival. *Angew Chem Int Ed.* **129,** 8630-8635 (2017).
34. Liu, Z., Xu, X., Tang, R. Improvement of biological organisms using functional material shells. *Adv Func Mater.* **26,** 1862-1880 (2016).
35. Park, J. H. *et al.* Nanocoating of single cells: from maintenance of cell viability to manipulation of cellular activities. *Adv Mater.* **26,** 2001-2010 (2014).
36. Yang, S. H. *et al.* Biomimetic encapsulation of individual cells with silica. *Angew Chem Int Ed.* **48,** 9160-9163 (2009).
37. Elani, Y. *et al.* Constructing vesicle-based artificial cells with embedded living cells as organelle-like modules. *Sci Rep.* **8,** 4564 (2018).
38. Wei, W. *et al*. A surface-display biohybrid approach to light-driven hydrogen production in air. *Sci. Adv.*, vol. 4, no. 2, eaap9253 (2018).
39. Das, A., & Ljungdahl, L. G. Electron-transport system in acetogens. In *Biochemistry and physiology of anaerobic bacteria* (pp. 191-204). Springer, New York, NY (2003).
40. Deutzmann, J. S., Sahin, M., & Spormann, A. M. Extracellular enzymes facilitate electron uptake in biocorrosion and bioelectrosynthesis. *MBio*, ***6*(2),** e00496-15 (2015).
41. Sytnyk, M. *et al.* Cellular interfaces with hydrogen-bonded organic semiconductor hierarchical nanocrystals. *Nat. Commun*. ***8*(1),** 91 (2017).
42. Reguera, G., McCarthy, K. D., Mehta, T., Nicoll, J. S., Tuominen, M. T., & Lovley, D. R. Extracellular electron transfer via microbial nanowires. *Nature*, ***435*(7045),** 1098 (2005).
43. Kornienko, N. *et al*. Spectroscopic elucidation of energy transfer in hybrid inorganic–biological organisms for solar-to-chemical production. *Proc. Natl. Acad. Sci. U. S. A.*, ***113*(42),** 11750-11755 (2016).

Chapter 2. Intracellular Au Nanocluster Photosensitized Bacteria for Solar Fuel Production

Section 2.1 Abstract

The demand for renewable and sustainable fuel has prompted the rapid development of advanced nanotechnologies to effectively harness the copious flux of solar power. The construction of photosynthetic biohybrid systems (PBSs) aims to link preassembled biosynthetic pathways with inorganic light absorbers. This strategy inherits both the high light-harvesting efficiency and the superior catalytic performance from solid-state semiconductors and whole-cell microorganisms, respectively. Here, we introduce an intracellular, biocompatible light absorber, namely gold nanoclusters (Au NCs), to circumvent the sluggish kinetics of electron transfer for existing PBSs. Translocation of these Au NCs into nonphotosynthetic bacteria enabled photosynthesis of acetic acid from CO_2. Besides, Au NCs also serve as reactive oxygen species (ROS) inhibitors to maintain high bacterium viability (Fig. 1). Taking the dual advantages of light absorption and biocompatibility, this new generation of PBS can efficiently harvest sunlight and transfer photo-generated electrons to cellular metabolism, realizing CO_2 fixation continuously over several days.

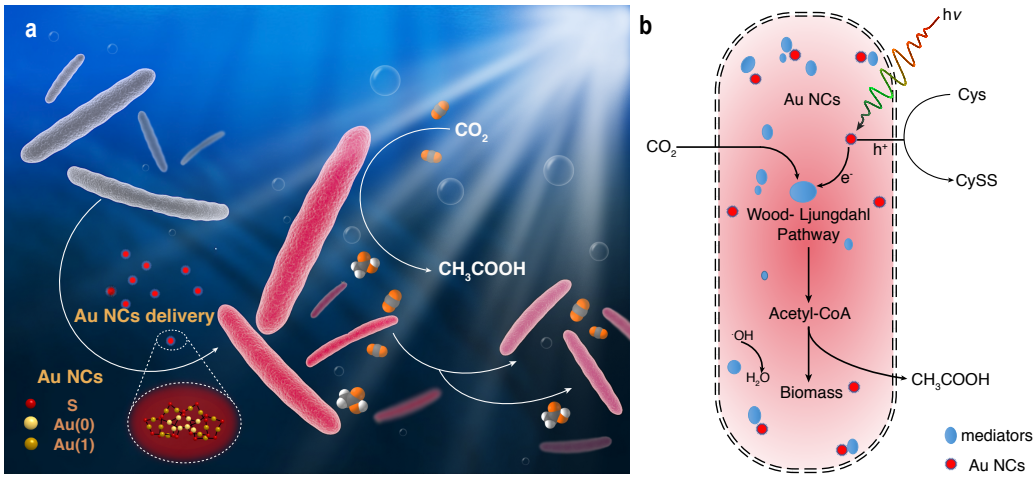

Fig. 2.1. The schematic diagram of the *M. thermoacetica*/Au NCs hybrid system. a, The $Au_{22}(SG)_{18}$ NCs were delivered into bare *M. thermoacetica* (grey) during culture process, forming *M. thermoacetica*/Au NCs with red emission. **b,** The electrons generated from intracellular Au NCs under illumination could be utilized by the enzymatic mediators inside the cytoplasm, and are finally passed on to the Wood-Ljungdahl pathway. The simulated chemical structure of $Au_{22}(SG)_{18}$ NCs was shown with differently colored balls[18]. Bright yellow balls: Au atoms in the core; dark yellow balls: Au atoms in the staple motifs; red balls: S atoms in the shell. All other atoms (carbon, hydrogen) have been omitted for clarity.

Section 2.2 Introduction

Although the solar-to-energy efficiencies of inorganic semiconductor devices can easily surpass 20%, the transduction of solar energy into specific organics remains a bottleneck for abiotic catalysts[1,2]. The construction of photosynthetic biohybrid systems (PBSs) enables the solar-to-chemical with high specificity and low cost[3]. Among several well-documented prototypes of inorganic-biological hybrid systems for photosynthetic CO_2 fixation[4-6], the whole-cell strategy is favored because of the involvement of a complete biological CO_2 reduction cycle and the ability to self-replicate and self-repair[7]. In conjunction with the development of bacterial synthetic biology, nonphotosynthetic organisms possess more desirable metabolic pathways than their photosynthetic counterparts, offering tunable CO_2 metabolism for diverse products[8]. Our first proof-of-concept whole-cell hybrid system was realized by interfacing the nonphotosynthetic and electrotrophic bacterium, *Sporomusa ovata*, with a photoelectrochemical silicon nanowire array[4]. *Sporomusa ovata* is able to directly utilize electrons from the silicon photoelectrode through the bio-inorganic interface assisted by numerous active enzymes and functional proteins on their membranes[9]. Recently, we demonstrated that the acetogenic bacterium, *Moorella thermoacetica* (ATCC 39073), can self-precipitate cadmium sulfide (CdS) nanoparticles on its membrane[7]. The photo-excited electrons from CdS nanoparticles are captured by membrane proteins to produce reducing equivalents that are ultimately transported into the cytoplasm to drive the Wood-Ljungdahl pathway for CO_2 fixation. In both examples, intimate bio-inorganic interfaces were formed between the inorganic semiconductors and the bacteria. Nevertheless, as most biocatalytic CO_2 fixation cycles are carried out in the cytoplasm, mass transport of redox shuttle molecules across the membrane into the cytoplasm would consume extra energy and be bottlenecked by transmembrane diffusion[10]. Therefore, simultaneous generation of photo-excited electrons and reducing equivalents inside the bacteria should potentially improve the efficiency of energy transduction. An essential prerequisite for the light absorbers is the ability to be taken by living microorganisms without losing its chemical integrity.

In this letter, we introduce ultra-small gold nanoclusters (Au NCs) as the biocompatible intracellular photosensitizer for the nonphotosynthetic bacteria. Au NCs possess chromophore-like discrete energy states and unique geometric structures[11]. Feasible tunability over core size and surface ligands of the Au NCs allows us to manipulate their biochemical/biophysical properties, such as cell uptake, cytotoxicity, biocompatibility, and molecular electronic structures[12-14]. In particular, several important strides have been made in the utilization of Au NCs in solar light harvesting as a visible-light absorber in the form of a type II junction[15]. Proof-of-concept studies have demonstrated that Au NCs can be delivered into mammalian cells either *in vivo* or *in vitro* to achieve the cell imaging with high biocompatibility[16,17].

Section 2.3 Experimental details

Section 2.3.1 Au nanoclusters synthesis

The red-emitting Au NCs were synthesized by a pH-mediated $NaBH_4$ reduction method[18,19]. In a typical synthesis, aqueous solutions of $HAuCl_4$ (12.5 mL, 20 mM) and GSH (7.5mL, 50 mM) were added to a 500-mL flask containing 180 mL of ultrapure water. After 2 min of vigorous stirring, the pH of the reaction solution was brought to 12.0 with 1 M NaOH. Thereafter, 0.24 mg $NaBH_4$ in 0.1 mL water was added into the reaction solution, stirring at 500 rpm at room

temperature. After 0.5 h, the solution pH was adjusted to 2.5 with 0.33 M HCl. The reaction solution was then sealed airtight and slowly stirred at 200 rpm for 8 h. An aqueous solution of strong red-emitting Au NCs was formed. To isolate Au NCs from the solution, isopropyl alcohol was added with 1:1 volume ratio. The dark red precipitate was collected through high speed centrifugation at 14000 rpm and washed with 1:1 methanol: H_2O mixture. Polyacrylamide gel electrophoresis (PAGE, 30 wt% monomers) was then applied to separate and collect $Au_{22}(SG)_{18}$ from $Au_{15}(SG)_{13}$ and $Au_{18}(SG)_{14}$ (Fig. 2.2).

Native Polyacrylamide Gel Electrophoresis (PAGE) separation of the as-synthesized Au NCs. Native PAGE was carried out on a Hoefer SE 600 system. The electrophoresis buffer was made of 192 mM glycine and 25 mM tris(hydroxymethyl)aminomethane. Stacking and resolving gels were prepared from 4 and 30 wt% acrylamide monomers (19:1 = monomer: crosslinker), respectively. 40 µL sample solutions (1 mg/mL crude Au NCs in 8 vol% glycerol aqueous solution) were loaded into the wells of the stacking gel. The electrophoresis was allowed to run for ~5 h at a constant voltage of 250 V at room temperature. The bands containing different-sized Au NCs were individually cut, crushed, and sonicated in ultrapure water for 20 min to allow the NCs in the gels to diffuse out. The resulting solutions were then filtered by use of a filter with 0.45 µm pore size, followed by adjusting the pH to 3.0. Methanol was then added into the solution gradually and the precipitate was collected as powders. The yield of individual NC species based on the Au atoms in the starting Au precursors was determined from inductively coupled plasma (ICP-MS) measurements.

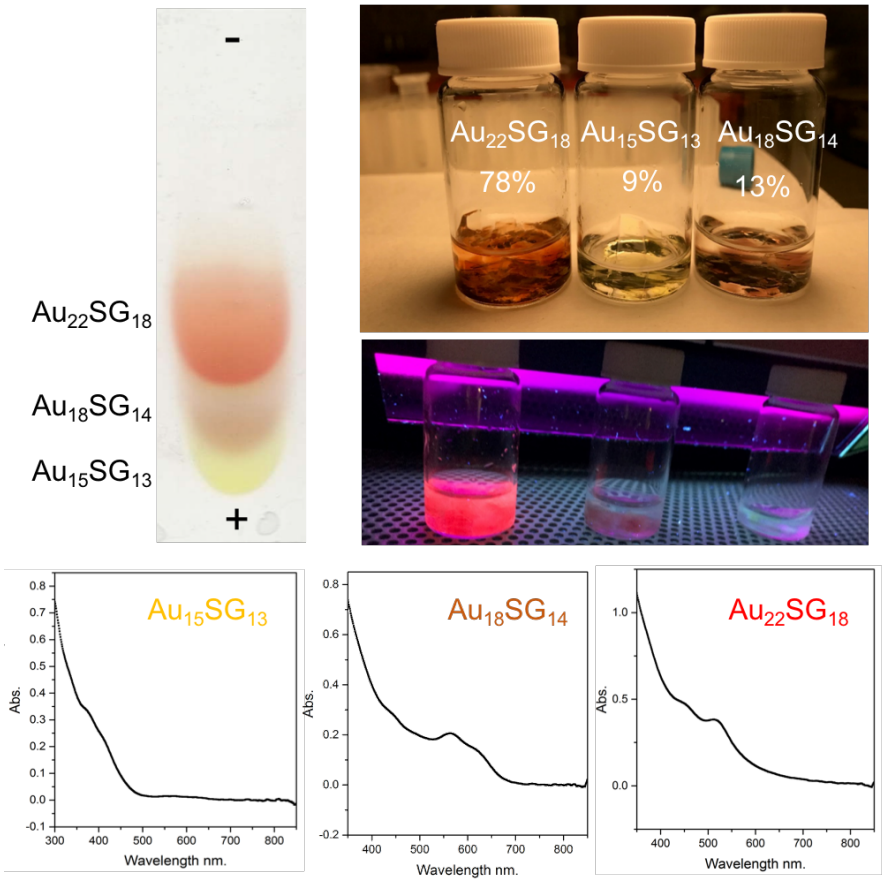

Fig. 2.2. Purification of $Au_{22}(SG)_{18}$ NCs *via* polyacrylamide gel electrophoresis. Polyacrylamide gel electrophoresis (PAGE, 30 wt% monomers) was used to separate and collect $Au_{22}(SG)_{18}$ from $Au_{15}(SG)_{13}$ and $Au_{18}(SG)_{14}$. The pure $Au_{22}(SG)_{18}$ NCs with unique red emission were used in the *M. thermoacetica*/Au NCs PBSs.

Section 2.3.2 Growth of *M. thermoacetica*/Au NCs

Preparation of heterotrophic medium and autotrophic medium. Both media were prepared under anaerobic conditions with deionized (DI) water. The Hungate technique or an anaerobic chamber (Coy Laboratory Products, Inc.) was employed in all operations to prevent exposure of the anaerobic bacteria to oxygen. The recipe for a general broth is as follows: to a bottle of 1 L degassed DI water was added 400 mg NaCl, 400 mg NH_4Cl, 330 mg $MgSO_4 \cdot 7H_2O$, 50 mg $CaCl_2$, 250 mg KCl, and 2.5 g $NaHCO_3$. The mixture was heated and stirred to boiling point under a continuous flux of nitrogen atmosphere, and 10 mL Wolfe's vitamin mix (Table 2.1) and 10 mL trace mineral mix (Table 2.2) were added after cooling down to room temperature. To make the heterotrophic medium, 25 mL 1 M glucose solution, 20 mL 5 wt.% Cys·HCl solution, 800 mg β-glycerophosphate·2Na·xH_2O, 500 mg yeast extract, and 500 mg tryptone were added into 1 L of the general broth and stirred until fully dissolved. To make the autotrophic medium, only 640 mg K_2HPO_4 was added into 1 L of the general broth. Yeast extract and tryptone were obtained from BD Biosciences, and all other reagents were obtained through Sigma-Aldrich. Anaerobic media were then dispensed under a mixed atmosphere (80:20 mixture of N_2: CO_2) into 16 x 125 mm Balch-type anaerobic culture tubes (Chemglass Life Sciences) with butyl rubber stoppers and screw caps, and 18 x 150 mm Balch-type anaerobic culture tubes (Chemglass Life Sciences) with butyl rubber stoppers and aluminum crimp seals. Media were then autoclaved for 15 min at 121°C before use.

Table 2.1. Wolfe's Vitamin Mix

Wolfe's Vitamin Mix	Pyridoxine·HCl	Thiamine·HCl	Riboflavin	Nicotinic acid	Thioctic acid
mg L^{-1}	10.0	5.0	5.0	5.0	5.0
	Calcium D-(+)-pantothenate	Biotin	Folic acid	Vitamin B12	
mg L^{-1}	5.0	2.0	2.0	0.1	

Table 2.2. Trace Mineral Mix

Trace Mineral Mix	Nitriloacetic acid	$MnSO_4 \cdot H_2O$	$CoCl_2 \cdot 6H_2O$	$ZnSO_4 \cdot 7H_2O$	$CuCl_2 \cdot 2H_2O$
mg L^{-1}	2000.0	1000.0	200.0	0.2	20.0
	$Fe(SO_4)_2(NH_4)_2 \cdot 6H_2O$	$NiCl_2 \cdot 6H_2O$	$Na_2MoO_4 \cdot 2H_2O$	Na_2SeO_4	Na_2WO_4
mg L^{-1}	800.0	20.0	20.0	20.0	

The initial inoculum of *M. thermoacetica* (ATCC 39073) was cultured in the heterotrophic medium, and the late log cultures were cryopreserved in a -80 °C freezer with 10% dimethyl sulfoxide as a cryoprotectant. To prepare *M. thermoacetica*/Au NCs hybrids, the thawed cryopreserved stock of 10 mL *M. thermoacetica* was inoculated in 10 mL of the anaerobic heterotrophic medium at 5 vol.%, and incubated with occasional agitation at 52 °C. The headspace of each tube was pressurized to 150 kPa with a flux of the mixed atmosphere (80:20 mixture of N_2: CO_2). After 2 days of growth (OD_{600} = 0.16), the culture was reinoculated at 5 vol.% into fresh heterotrophic medium, and incubated at 52°C. After 36 hours of growth (OD_{600} = 0.28), 0.5 mL 4 mg/mL $Au_{22}(SG)_{18}$ solution was added to each tube. The chemical stability of Au NCs at different concentrations was tested *via* UV-vis absorption, and the intracellular Au NCs stability was explored via the structure illumination microscope(SIM) emission intensity as well. The tubes were returned to incubation and placed in the mini shaker (VMR) at a speed of 100 rpm for 1h, and then stand still for the rest days without shaking. After an additional 1 day, each tube was centrifuged at 2500 rpm for 10 min, washed and resuspended in an equivalent volume of autotrophic medium supplemented with 0.1 wt.% cysteine. 10mL of the suspension was distributed into each clean anaerobic tube equipped with a magnetic stir bar (sealed and autoclaved as previously described). Each tube was pressurized with 150 kPa of 80:20 H_2: CO_2 and incubated for 12 hours at 52 °C to promote autotrophic respiration.

Section 2.3.3 Photosynthesis measurements

Prior to photosynthesis, the mixed flux of 80:20 N_2: CO_2 was continuously applied to each tube for 5 mins to extrude the residual mixture of H_2 and CO_2. Then, an additional 0.1 wt.% cysteine was added to each tube (total 0.2 wt.%, nominal). Each tube was stirred at 150 rpm and heated to a measured temperature of 55 °C by a stirring hot plate. The illumination source employed for simulated sunlight measurements was a collimated 75 W Xenon lamp (Newport, Corp.) with an AM 1.5G filter. All light intensities were calibrated by a silicon photodiode (Hamamatsu S1787-04). Concentrations of photosynthetic products were measured by ^{1}H-qNMR with sodium 3-(trimethylsilyl)-2,2',3,3'-tetradeuteropropionate (TMSP-d4, Cambridge Isotope Laboratories, Inc.) as the internal standard in D_2O. Spectra were processed using the MestReNova software. The experiments for all the conditions were replicated and the sample sizes were listed in the caption. The ^{13}C isotope labeling experiments were conducted in the autotrophic media with $NaH^{13}CO_3$, and the headspace was pressurized by $^{13}CO_2$. Photosynthetic products were measured by ^{1}H-NMR and ^{13}C-NMR.

Section 2.3.4 Viability and ROS assay test

Viability test: Cell mL^{-1} values were determined by manual counting with a Petroff-Hauser counting chamber both under dark and light conditions. In parallel, the Colony Forming Unit (CFU) Assays were performed by sampling and inoculating 0.1 mL of the *M. thermoacetica*, *M. thermoacetica*-CdS and *M. thermoacetica*/Au NCs photosynthesis suspension into 5 mL of molten (T > 50 °C) agar broth supplemented with 40 mM glucose and 0.1 wt.% cysteine to double check the viability. After thorough mixing, place the tubes horizontally in ice to set a thin layer of agar on the sidewalls of the anaerobic tubes. Assay tubes were pressurized to 150 kPa with 80: 20 N_2: CO_2 and incubated vertically at 52 °C. After 3 days of growth, visible white, circular colonies were

counted to determine the CFU mL^{-1} as a measure of cell number and viability in the light. In the meantime, the viability of *M. thermoacetica*/Au NCs with different Au NCs concentrations in dark was measured.

ROS assay test: Fluorometric Intracellular ROS Assay MAK143 Kit was cultured with *M. thermoacetica*/Au NCs for sensitive, one-step fluorometric to detect intracellular ROS (especially superoxide and hydroxyl radicals) in live cells within 1 hour incubation. The medium was as the control. The analysis was performed 12 and 48 after the illuminated in autotrophic medium. The 96 well with clear bottom black plate was used for fluorometric emission (λ_{ex} = 490/λ_{em} = 520 nm). The relative luminescence units were measured by a plate reader (DTX 880, Beckman Coulter).

Section 2.3.5 Microscope sample preparations

Optical Characterization: The UV-Vis spectra of *M. thermoacetica*/Au NCs suspensions were obtained *via* a Shimadzu UV3101PC UV-Vis-NIR Spectrophotometer with an integrating sphere. Photoluminescence spectra were taken in a confocal fluorescence spectroscope based on a Horiba LabRAM HR system. The excitation solid state laser illumination at the wavelength 532 nm was focused onto the sample *via* an optical objective (20x magnification, numerical aperture 0.4). Fluorescence from the sample was collected by the same objective and sent to the spectroscopy for analysis. The spectroscope was equipped with a diffraction grating of 600 lines mm^{-1} (blaze wavelength at 500 nm) and a charge coupled device (CCD) camera.

SIM Microscopy: Super-resolution 3D-structured illumination microscopy (SIM) imaging was performed on a Zeiss ELYRA PS.1 system (Carl Zeiss). Images were acquired with a Plan-Apochromat 100x /1.40 oil immersion objective and an Andor iXon 885 EMCCD camera. A 100 mW 540 nm optically pumped semiconductor laser (Coherent Inc.) and a BP 570/650 nm emission filter (Optics Balzers AG, Balzers, Liechtenstein) were used. Twenty-eight images per plane (three rotations) and 86 nm z section of total 2.4 μm height were acquired for generating super resolution images. Raw images were reconstructed and processed to demonstrate structure with greater resolution by the ZEN 2011 software (Carl Zeiss), and the Imaris software was used to analyze the re-constructed images.

Electron Microscopy: Samples of fixed *M. thermoacetica*-CdS and *M. thermoacetica*/Au NCs were prepared for STEM by dropping the fixed suspension onto Formvar coated Ultrathin Carbon Cu TEM grids, settling for 1 hour, and washing briefly in DI water. Grids were air dried overnight. STEM imaging and EDS mapping was performed at 80 kV with an FEI Titan microscope at the National Center for Electron Microscopy (NCEM). The EDS signal was acquired *via* a FEI SuperX Quad windowless detector based on silicon drift technology that was controlled by Bruker Esprit software.

Section 2.4 Results and discussion

Section 2.4.1 The characterization of intracellular biohybrid system

Water-soluble Au NCs of majority $Au_{22}(SG)_{18}$ (SG = glutathione) were synthesized as describe above. *M. thermoacetica* bacteria were inoculated and cultured in heterotrophic medium for two days before the $Au_{22}(SG)_{18}$ solution was injected. In the following two days, bacteria underwent exponential growth in the presence of Au NCs, and then they were centrifuged, separated from the supernatant, and redispersed in the autotrophic medium. In Fig. 2.3, the redispersed solution shows almost the same color as it is before the centrifugation, whereas the supernatant is clear, suggesting that Au NCs were preferentially taken by *M. thermoacetica* with a 95.37% uptake efficiency. Furthermore, ultraviolet-visible (UV-vis) absorption spectrum of the redispersed *M. thermoacetica*/Au NCs solution displays the same characteristic peaks as the bare Au NCs solution, in contrast to the featureless absorption curve of the bare *M. thermoacetica* solution, indicating that the Au NCs stay intact during the integration process.

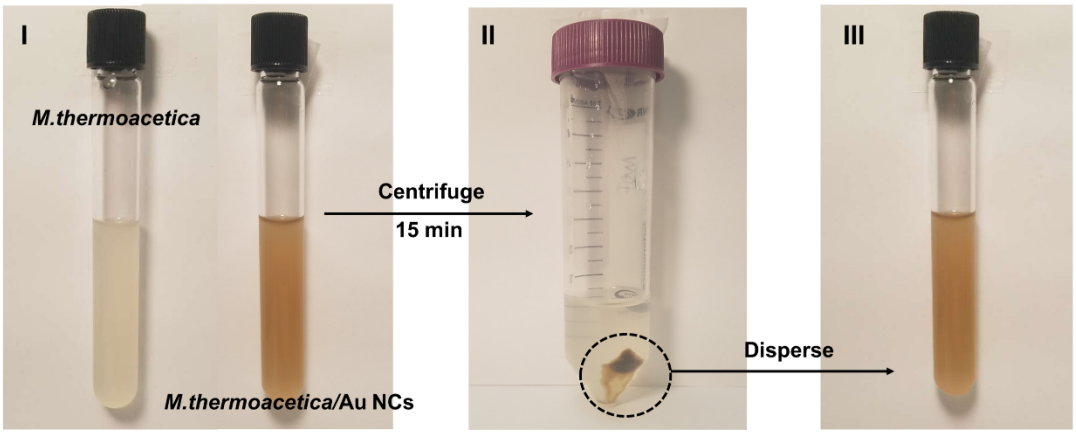

Fig. 2.3. The characterization of *M. thermoacetica*/Au NCs hybrid system and deletional controls. I, picture of the bare *M. thermoacetica* and *M. thermoacetica*/Au NCs with different colors. **II,** picture displaying the colorless supernatant of *M. thermoacetica*/Au NCs hybrid system after centrifugation. **III,** picture of redispersed solution from II sediment.

Structure illumination microscopy (SIM) was further used to clarify the location of Au NCs in the hybrid biosystem by collecting the emissive fluorescence from Au NCs under excitation at 540 nm (Fig. 2.4a)[20]. Fig. 2.4 displays the image of a bunch of Au NCs-treated *M. thermoacetica* on different focal planes with a step increment of 86 nm along the z direction. It clearly shows the volcano-like emission intensity profile from the bottom through the top cross-sections of the bacteria. A movie of the reconstructed 3D model of an individual Au NCs-treated *M. thermoacetica* is available in the Supplementary. In order to draw a solid conclusion, the same culturing conditions were applied to the bare *M. thermoacetica* and the *M. thermoacetica*/CdS PBS as well. As a control, the bare *M. thermoacetica* displays no PL emission and results in an absolute dark image under 540 nm illumination (Fig. 2.5). In comparison (Fig. 2.4c and Fig. 2.4d), the SIM images of the *M. thermoacetica*-CdS PBS excited at 408 nm show greenish PL emission with an annular shape from the membrane-bound CdS nanoparticles. The distinct SIM PL emission patterns confirm the successful transportation of Au NCs into the cytoplasm of *M. thermoacetica*. Additionally, high angle annular dark field scanning transmission electron microscopy (HAADF-STEM) and energy-dispersive X-ray spectroscopy (EDS) mapping were performed to verify the location of Au NCs (Fig. 2.4e, f, g). As shown in Fig. 2.4f, gold element was mostly detected and

well distributed across the whole bacteria without obvious aggregation on the membrane. Although the mechanistic study of Au NCs delivery into bacteria remains to be fully explored, the well-documented specific uptake of various metal nanoparticles and quantum-dots (QDs) into mammalian cells can provide us a clue. In order to be specifically taken by living cells, nano-sized particles are chemically linked to biorecognition molecules such as peptides, antibodies, nucleic acids or small-molecule ligands for particular applications[21,22]. In this regard, we hypothesize that the specific Au NCs uptake by *M. thermoacetica* is similarly mediated by the tripeptide surface ligand, glutathione, for its strong bioaffinity *via* passive targeting[23,24].

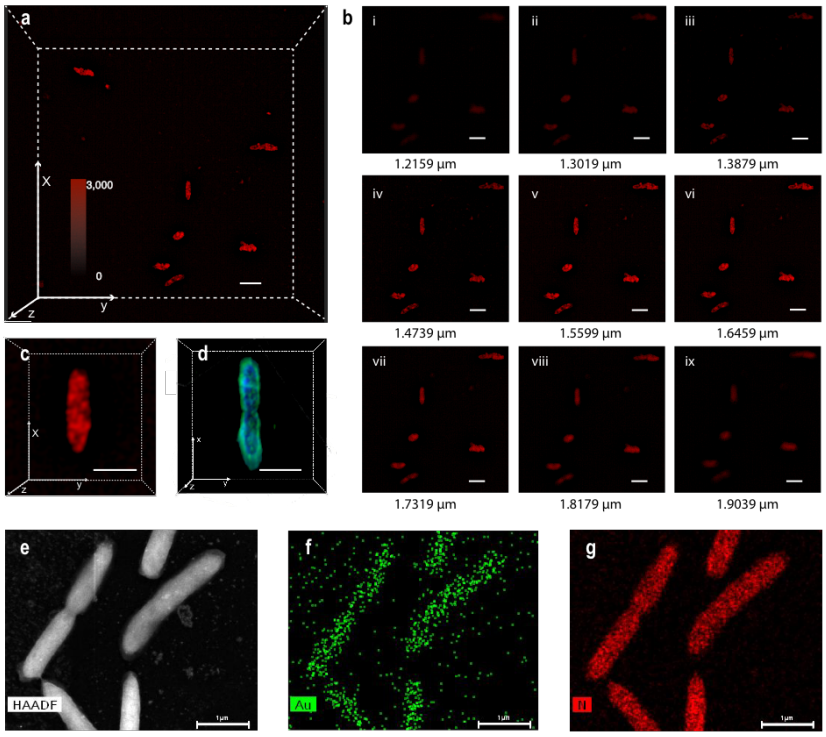

Fig. 2.4. The microscopy images of the *M. thermoacetica*/Au NCs hybrid system. a, SIM image of a bunch of *M. thermoacetica*/Au NCs with red fluorescence (excitation at 540 nm) with total counts ranging from 0 to 3,000. **b,** SIM images of different focal planes along z direction. **c,** SIM image of individual *M. thermoacetica*/Au NCs PBS. **d**, SIM image of a single *M. thermoacetica*-CdS PBS (excitation at 408 nm) with annular-shaped emission. **e**, HAADF-STEM image of *M. thermoacetica*/Au NCs, and EDS mapping showing **f,** Au and **g**, N elements across the entire cell. Scale bar for a. b. c. d is 2 µm.

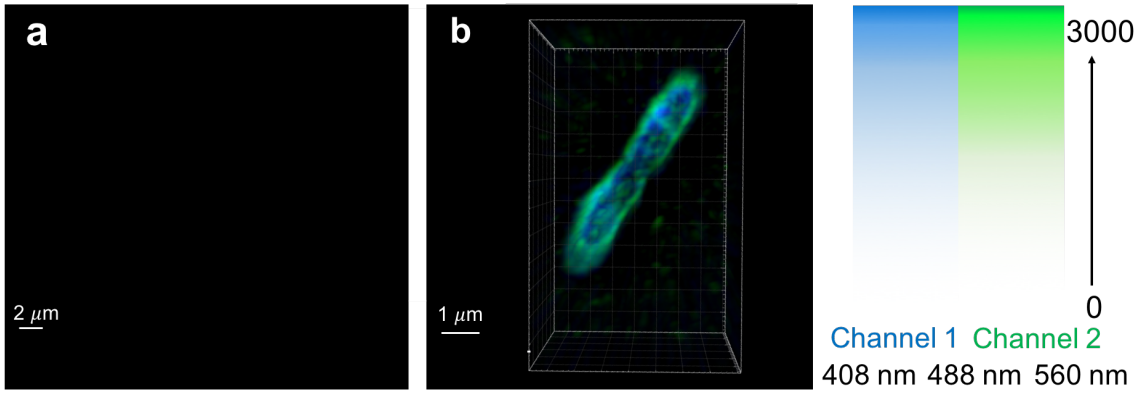

Fig. 2.5. SIM images of deletional controls. a, the SIM images of bare *M. thermoacetica* without emission under 540 nm excitation. **b,** the SIM image of *M. thermoacetica*-CdS PBS under 408 nm excitation with annular shape emission. The color-code bar reveals the relative fluorescence intensity, counts ranging from 0 to 3000.

Section 2.4.2 Photosynthesis of *M. thermoacetica*/Au nanoclusters hybrid system

After successful incorporation of Au NCs into living bacteria, the photosynthetic ability of the hybrid system was examined. Before being exposed to low-intensity simulated sunlight (calibrated by photodiode, air mass 1.5 global spectrum, 2 W m^{-2}), the heterotrophic medium was replaced by the autotrophic medium, to make sure that CO_2 is the only external carbon source for *M. thermoacetica*. As the only respiration product, the concentration of acetic acid was monitored by quantitative proton nuclear magnetic resonance (^{1}H-qNMR), and the ^{13}C isotope labeling was also carried out to track the carbon source during the photosynthesis in order to double-check and track the carbon source. The $^{13}CO_2$ and $NaH^{13}CO_3$ were purchased from Sigma Aldrich Company with 99% purity. $NaH^{13}CO_3$ was used in the autotrophic medium and the headspace is pressurized by $^{13}CO_2$. From the ^{1}H-NMR and ^{13}C-NMR spectra in Fig 2.6, the acetate can be detected. From the ^{1}H-NMR spectra of acetate produced from unlabeled and ^{13}C-labeled batch, the obviously different peak features can be detected. For ^{13}C-labled samples, the high abundance of ^{13}C in the acetate magnifies $^1J_{CH}$ and $^2J_{CH}$ coupling, resulting in the satellite peaks in the spectrum. The unlabeled one shows the single peak with 1.85 ppm chemical shift. With the addition of $NaH^{13}CO_3$, the ^{13}C-signal is strongly enhanced in bicarbonate, dissolved CO_2, and the produced acetate molecules, while the unlabeled acetate spectrum is featureless with ^{12}C. These isotope labeling spectra indicate that the CO_2 gas or HCO_3^- is the inorganic carbon source for the acetate generation in *M.thermoacetica*/Au NCs system.

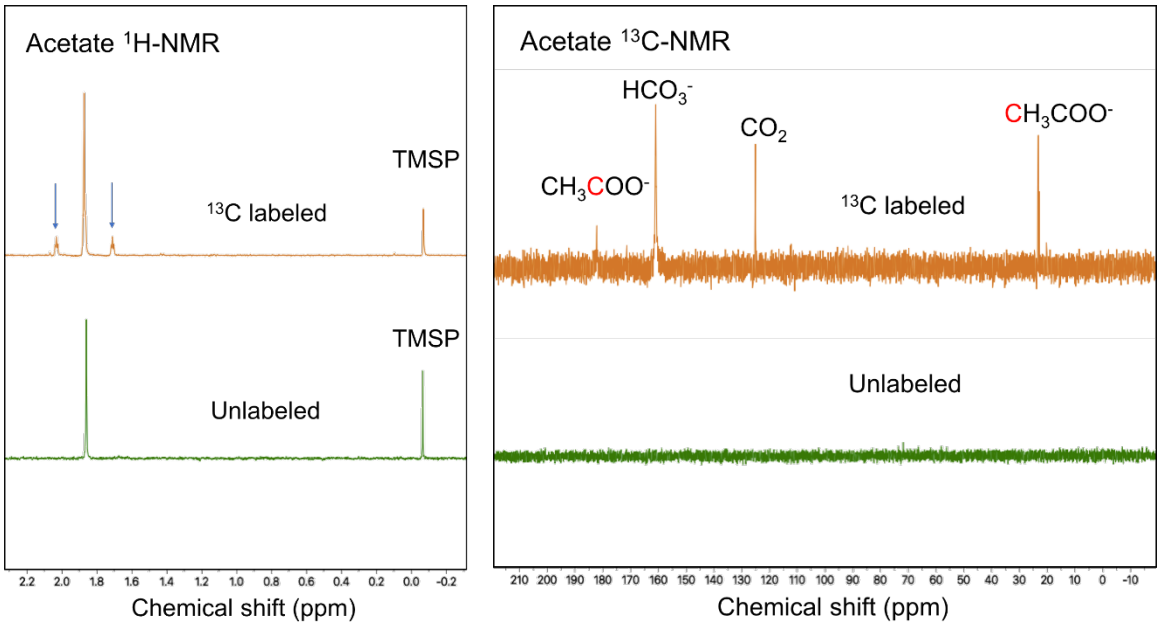

Fig. 2.6. ^{1}H-NMR and ^{13}C-NMR spectra of acetate labeled with ^{13}C. For ^{13}C-labled samples, the high abundance of ^{13}C in the acetate magnifies $^{1}J_{CH}$ and $^{2}J_{CH}$ coupling, resulting in the satellite peaks in the spectrum in ^{1}H-NMR. The unlabeled one shows the single peak with 1.85 ppm chemical shift. With the addition of $NaH^{13}CO_3$, the ^{13}C-signal is strongly enhanced in bicarbonate, dissolved CO_2, and the produced acetate molecules, while the unlabeled acetate spectrum is featureless with ^{12}C.

Some very restricted controls in terms of the number of cells, culture volume, and optimized light absorbers concentration, for *M.thermoacetica*/Au NCs and *M.thermoacetica*-CdS systems were carried out to make it comparable between them. For the number of cells and culture volume, the bacteria in these two systems are from the same batch to guarantee the same concentration of viable bacteria under the same generations (or phases) for the following experiments. The concentration (mM) of acetate is used to describe the overall performance instead of absolute moles of acetate. For the concentration of Au NCs and CdS nanoparticles, it's practical and fair to compare these systems with the optimized concentration for each.

The overall acetate yield in hybrid system could be affected by several factors, such as the amount of photo-excited electrons, the viable bacterium population, the turn-over-frequency of bacteria, and the amount of hole scavengers. In order to take all the factors into account, using dry weight to normalize the acetate yield could be appropriate to describe the differences between Au NCs and CdS hybrid systems. The initial bacteria amount is the fixed parameter for all systems, and the overall dry weight after the photosynthesis could reveal the cell population, which reflects the toxicity of photosensitizer as well. This normalization could satisfy most criteria for assessing the system efficiency. The dry weights of bare bacteria, *M.thermoacetica*/Au NCs, and *M.thermoacetica*-CdS systems were measured, and the mass of photosensitizers was carefully subtracted *via* the following calculations. The total concentration of CdS is determined by $[Cd^{2+}]$ due to the sufficient S^{2-} in the medium.

Mass of CdS will be 0.1mM ×144.46 g/mol = 14.45 mg/L

Mass of Au NCs will be 0.5ml × 0.4mg/ml / 0.01L = 20.00 mg/L

	M.thermoacetica	*M.thermoacetica*/Au NCs	*M.thermoacetica*-CdS
Dry weight (mg/L)	280± 20	328± 15	291± 18
Mass of material	NA	20.00	14.45
Net dry weight (mg/L)	280± 20	308± 15	276± 18
Acetate/dry weight (mmol/g)	NA	5.84	4.34

The acetic acid yield was normalized to the dry weight after the photosynthesis for each system, which presents the overall cell information by taking cell population, cell phases, and toxicity effects of photosensitizers into account. In the two deletional controls, namely the bare *M. thermoacetica* in the light and the *M. thermoacetica*/Au NCs in the dark, the acetic acid yield is negligible (Fig. 2.7a). Particularly, the *M. thermoacetica*/Au NCs system exhibits faster acetic acid production than the *M. thermacetica*-CdS system. After four days, the accumulated acetic acid yield of *M. thermoacetica*/Au NCs is notably higher than that of the *M. thermoacetica*-CdS system. In order to illustrate the photosensitizing behavior of Au NCs inside *M. thermoacetica*, we employed the PL spectroscopy to study the electron transfer between Au NCs and the bacteria (Fig. 2.7b). The bare Au NCs solution shows strong red and near infrared PL emission centered at 680 nm when being excited by a 532 nm solid state laser beam, while the bare *M. thermoacetica* solution shows no PL emission at all. Before carrying out the photosynthesis, the PL emission spectrum of the *M. thermoacetica*/Au NCs in the CO_2 free medium gives a broad peak with slight red shift and slimmer intensity than the bare Au NCs solution. However, during the photosynthetic process, the red PL emission of the *M. thermoacetica/*Au NCs solution are totally quenched. Thus, it is reasoned that instead of undergoing a recombination process, the photo-excited electrons from Au NCs are transferred to some cytoplasm-distributed redox mediators, such like ferredoxin (Fd), flavoproteins (Fp) and rubredoxins(Rd) (Table 2.3) as illustrated in previous enzymological and thermodynamic studies on the same bacterium[25,26].

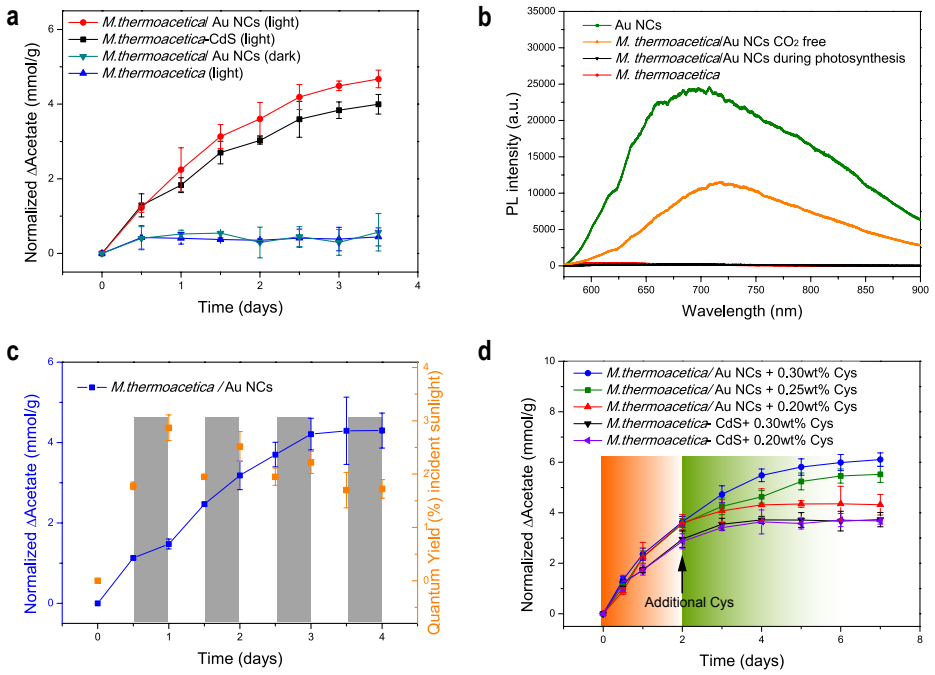

Fig. 2.7. Photosynthesis behavior of different systems. a, Normalized photosynthetic production of acetic acid by *M. thermoacetica*, *M. thermoacetica*/Au NCs and *M. thermoacetic*-CdS PBSs under continuous low-intensity illumination and dark condition (replicated times n = 20 culture batches for *M. thermoacetica*-CdS (light), n = 35 culture batches for other conditions). **b,** PL spectra of pure Au NCs, bare *M. thermoacetica, M. thermoacetica*/Au NCs in CO_2 free conditions without photosynthesis ability, and *M. thermoacetica*/Au NCs in photosynthesis process. **c**, Normalized acetic acid production and incident quantum yield of *M. thermoacetica*/Au NCs with light-dark cycles (replicated times n = 21 culture batches). **d,** Cysteine dependent acetic acid yield in *M. thermoacetica*/Au NCs and *M. thermoacetica*-CdS with additive cysteine for seven days of photosynthesis (replicated times n = 12 culture batches). All points and error bars show the mean and error-propagated SD, respectively, of the experiments.

Table 2.3. Components of the ET chain and their subcellular locations in *M. thermoacetica*. The bifunctional enzyme carbon monoxide dehydrogenase/acetyl-CoA synthase (CODH/ACS) is the key enzyme of the acetyl-CoA pathway[5].

Membrane only	Cytosol only	Both membranes and cytosol
Menaquinone	Ferredoxin I	Ferredoxin II
Cytochrome b_{554}	Rubrerythrin	Flavoprotein/flavodoxin
F_1F_0 ATP synthase	Rubredoxin oxidoreductase	High molecular weight rubredoxin (Hrb)
	Type A flavoprotein (FprA)	CODH/ACS
	High molecular weight	Methanol dehydrogenase
	Methanol dehydrogenase	Hydrogenase
	rubredoxin	NADH dehydrogenase
	Formate dehydrogenase	Cytochrome b_{560}
		Methylene-THF reductase
		Methyl transferase

Moreover, an average lifetime of 729 ns was determined for the luminescence decay at 630 nm for the bare Au NCs solution, which results from the ligand-to-metal-metal charge transfer (LMMCT) relaxation occurring at a triplet metal-centered state in the long, interlocked gold shell[27]. The ultra-long PL lifetime is beneficial for the electron transfer from Au NCs to the energy-transfer-system (ETS) in cytoplasm[28]. Ultimately, the photo-excited electrons from Au NCs are passed on to the Wood-Ljungdahl pathway to synthesize acetic acid from CO_2, while the holes are quenched by cysteine, resulting in its oxidized form cystine[7]. The overall photosynthetic reaction is

$$2\ CO_2 + 8\ Cys + 8\ h\nu \xrightarrow{M.\ thermoacetica/\text{Au NCs}} CH_3COOH + 2\ H_2O + 4\ CySS \qquad (1)$$

Which can be split into several steps:

$$8\text{Au NCs} + 8h\nu + 2CO_2 + 8H^+ \xrightarrow{M.thermoacetica} 8\text{Au NCs}^* + CH_3COOH + 2H_2O$$

$$Cys + Cys \rightarrow CySS + 2H^+ + 2e^-$$

$$8\text{Au NCs}^* + 8e^- \rightarrow 8\text{Au NCs}$$

According to several previous studies, Au NCs with different chemical compositions have different HOMO and LUMO energy diagrams[15]. In such Au NCs, photoexcitation occurs in two nondegenerate states near the HOMO-LUMO gap that are derived from the Au metal core and the ligand S atom orbitals. In analog to inorganic semiconductors, once the electrons are photo-excited from the HOMO level to the LUMO or higher levels, a "hole-electron pair" is generated in a single Au NC. In our case, the photo-excited electrons in Au_{22} NCs are located in the LUMO and near energy levels, which would be transferred to the electron acceptors with appropriate energy states. Actually, there are several enzymes as the electron acceptors involved in the WLP process (Fig. 2.8). Once photo-excited electrons from the Au_{22} NCs are transferred to the enzyme electron acceptors, a "hole" actually remains in the Au_{22} NCs. The oxidized Au NCs can be reduced by red-ox couple 'cysteine-cystine' to scavenge the "hole".

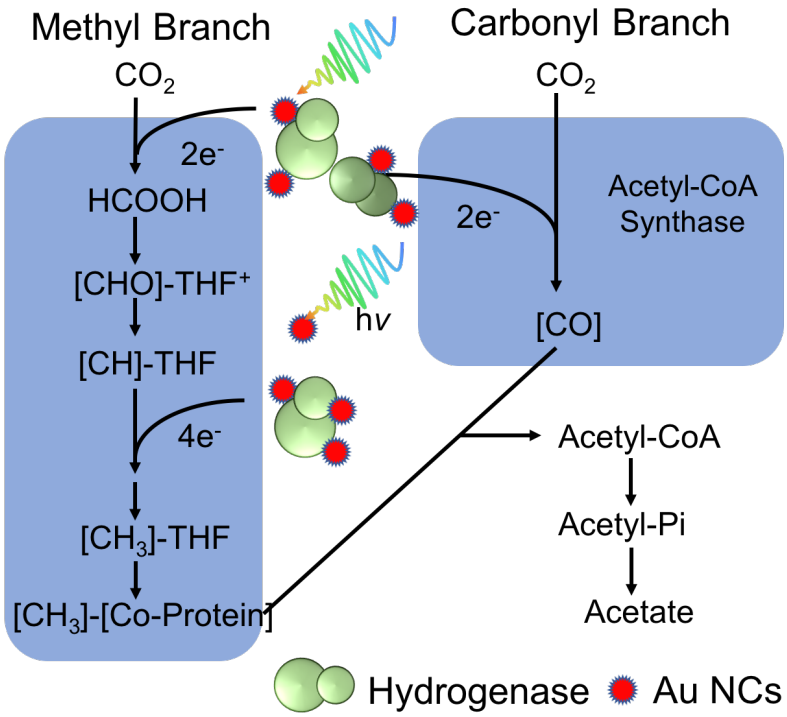

Fig. 2.8. The acetyl-CoA pathway as resolved from *M. thermoacetica*. Abbreviations: THF, tetrahydrofolate; Pi, inorganic phosphate; [e^-], reducing equivalent; Co-Protein, corrinoid enzyme[34].

To further study the photosynthetic behavior, we illuminated *M. thermoacetica*/Au NCs hybrids following an alternative light-dark cycle of 12 hours each to imitate the intermittent nature of the solar source. In Fig. 2.7c, we can see a continuous production of acetic acid during the day-night cycles, mainly due to the accumulation of metabolic intermediates as illustrated in our previous study[7], which could be affirmed by the observation of distinct acetic acid increase rates for dark cycles. The least acetic acid increase in the first dark cycle compared to that of the following dark cycles indicates the potential deficit of the accumulated biosynthetic intermediates at the beginning, and the possible explanation lies in the insufficient energy generated or quickly consumption for biomass.

The quantum efficiency was quantified daily by the ratio of the effective electrons used for acetic acid production to the total input photon flux. The reduction of two CO_2 molecules to one acetic acid molecule requires 8 electrons.

$$QE\% = \frac{\#\ electrons}{\#\ photons} \times 100\% = \frac{8 \times mol\ acetate\ generated}{mol\ total\ photons} \times 100\%$$

Where

mol acetate generated = the total acetate concentration (Ca) × total suspension volume (V)

mol total photons = photo flux (Φph cm^{-2} s^{-1}) × area of illumination (A) × reaction time (t) / Avogadro's Number (N_A)

Therefore, the QE% can be rewritten as:

$$QE\% = \frac{8 \times Ca \times V \times N_A}{\Phi ph \times t \times A} \times 100\%$$

The following calculation example is based on the data from day 0.5.

Ca = 0.375 mM V= 10 ml $N_A = 6.022\times10^{23}$

Integration photons 320 - 610 nm: $\Phi ph = 1.54 \times 10^{14}\ s^{-1}\ cm^{-2}$ t = 12h × 3600 = 43200 s A = 15 cm^2

$$8\times Ca\times V\times N_A = 8 \times 0.375 \times 10^{-3} \times 10 \times 10^{-3} \times 6.022 \times 10^{23} = 1.807 \times 10^{18}$$

$$\Phi ph \times t \times A = 1.54 \times 10^{14} \times 43200 \times 15 = 9.983 \times 10^{19}$$

$$QE\% = \frac{8\times Ca\times V\times NA}{\Phi ph \times t\times A} = \frac{1.807 \times 10^{18}}{9.983 \times 10^{19}} \times 100\% = 1.81\%$$

The overall quantum efficiency can be as high as 2.86 $\pm$ 0.38% at the first day, which is 33% higher than *M. thermoacetica*-CdS with 2.14 $\pm$ 0.16%, reflecting a better CO_2 fixation ability in *M.thermoacetica*/Au NCs system. Additionally, although the natural photosynthesis can produce organics *via* CO_2 fixation during daytimes, most of them are consumed by the respiration process at nights. Nevertheless, the photosynthetic product in this *M. thermoacetica*/Au NCs PBS, acetic acid, cannot be catabolized by *M. thermoacetica*, and thus, the common catabolic energy loss in the dark cycles is absent. Therefore, this special behavior could potentially help the PBS to outstrip the utility of natural photosynthesis in near future. In Fig 2.7c of the light-dark cycle photosynthesis performance, there is a comparable dark and light acetate production from day1 to day3, while the rates show a stronger dependence on light from day 0-1. This phenomenon could be explained through a deep insight into the WLP metabolic process during the photosynthesis. The photo-excited electrons from Au NCs triggered the WLP process to fix CO_2 under illumination, and meanwhile, such process can accumulate biosynthetic intermediates during the light cycle. These may include a number of reductive species [e.g., NADH (reduced nicotinamide adenine di-nucleotide), NADPH (reducedNADphosphate), or ferredoxin] or intermediates in the WLP such as acetyl-CoA. A proton gradient may also store energy for adenosine triphosphate synthesis in the dark. From day 0 to day 1, the light and dark acetate yields are distinctly different when compared to that of day1-3. A potential explanation lies in the deficit of the accumulated biosynthetic intermediates. The generated energy *via* input photons within the first 12 hours of illumination may not be able to provide sufficient intermediates for the first dark cycle, which causes the disparate acetate yield rates in the first day. The cell division could also help to explain the different light and dark acetate yields in the day1. Considering that the bacteria we used for the photosynthesis are in their late exponential and close to stationary stage, their division capability is not as good as the log phase. We observed an increase of viable bacteria in all three systems. Such increase is partially attributed to the completion of cell division of those duplicated yet not completely split bacteria. The generated intermediates or proton gradient during the light cycle could be partially utilized to generate biomass for the growth of the newly-split bacteria. With high bacteria population at day0-1.5, the stored intermediates for the dark cycle are not sufficient to maintain the same acetate production rate as the light cycle in day1.

Either the continuous or light-dark cycle experiment reveals that the rate of acetic acid production began to plateau after 3 days. We postulated that the sacrificial hole scavenger, namely Cys, was quickly consumed by the *M. thermoacetica*/Au NCs PBS during the first three days of photosynthesis. Therefore, a second injection of Cys with varying amount was carried out at day 2. In Fig. 2.7d, the accumulated acetic acid production normalized by dry weight after a week of photosynthesis reached 4.51 mmol/g, 5.52 mmol/g and 6.01 mmol/g when the overall feed of Cys was 0.2 wt%, 0.25 wt% and 0.3 wt%, respectively. On the contrary, the addition of extra Cys in

the *M. thermoacetica*-CdS PBS did not improve the acetic acid production. This phenomenon can be explained by the structural instability of membrane-bound CdS nanoparticles, evidenced by the observation of severe ripening and ultimately peeling off from the membranes, and the successive photo-oxidization of CdS under long-time illumination. The acetic acid upsurge around 80% in the *M. thermoacetica*/Au NCs system affirms its ability to conduct a continuous solar-to-chemical conversion process. To explain this disparity, we should take into consideration the following two factors: (1) total efficient photo-excited electrons; (2) effective charge transfer pathways.

Both Au NCs and CdS nanoparticles, as light absorbers, are able to provide enough photo-excited electrons for WLP to produce acetate in the first 2 days. Nevertheless, only Au NCs own the good structural stability, and the membrane-bound CdS NPs suffer from a successive photo-oxidization under long-time illumination. A lot of membrane-bound CdS NPs were converted into oxidative states with less absorption, where the total photo-excited electrons in CdS system were largely reduced in the following days of photosynthesis reactions. Moreover, with partial oxidized states, the band-positions of CdS changed, which may not be suitable for electron transfer between CdS and membrane-bound electron acceptors. We also observed that CdS NPs severely ripened and ultimately peeled off from the membranes. Due to this structural instability, the separation between CdS NPs and bacteria cut off the effective charge transfer pathways. With no sufficient energy source (e^- or H_2) provided, the *M.thermoacetica*-CdS system cannot undergo the WLP for CO_2 fixation even though cysteine is not the limiting factor. With such two issues in the *M.thermoacetica*-CdS system, it is difficult to boost the acetate yield only by increasing the cysteine concentration. These could be the reasons why the cysteine dependent experiments show different trends in the two systems.

The AuNCs intracellular stability has been examined as well. Au NCs with different compositions display diverse absorption patterns[29]. The UV-vis absorption patterns of several types of Au NCs are mostly broad bumps other than sharp peaks. This absorption pattern characteristic makes it difficult to distinguish the UV-Vis absorption signal of Au_{22} NCs in the *M.thermoacetica*/Au NCs system from the strong cell membrane absorptions. Fortunately, among all those Au NCs, Au_{22} has the strongest red PL emission[18]. Therefore, we can take advantage of the structure illumination microscope (SIM) to demonstrate the intracellular stability of Au NCs. The intracellular stability measurement is based on two simple facts: (1) only several specific Au NCs are emissive, and 670 nm red emission is merely originated from Au_{22}[18]; (2) the red PL emission can be detected by SIM only when Au_{22} are intact. Therefore, SIM provides us a convenient approach to evaluate the stability over time by visually check the photoluminescence changes. Fig. 2.9 shows the SIM images with the same excitation energy (541 nm) and the same exposure time during the data acquisitions. The identical red emission with almost the same intensity generated intracellularly from day 1 to day 5 verifies the good stability of intracellular Au NCs. Otherwise, there should be no or dimmer emission.

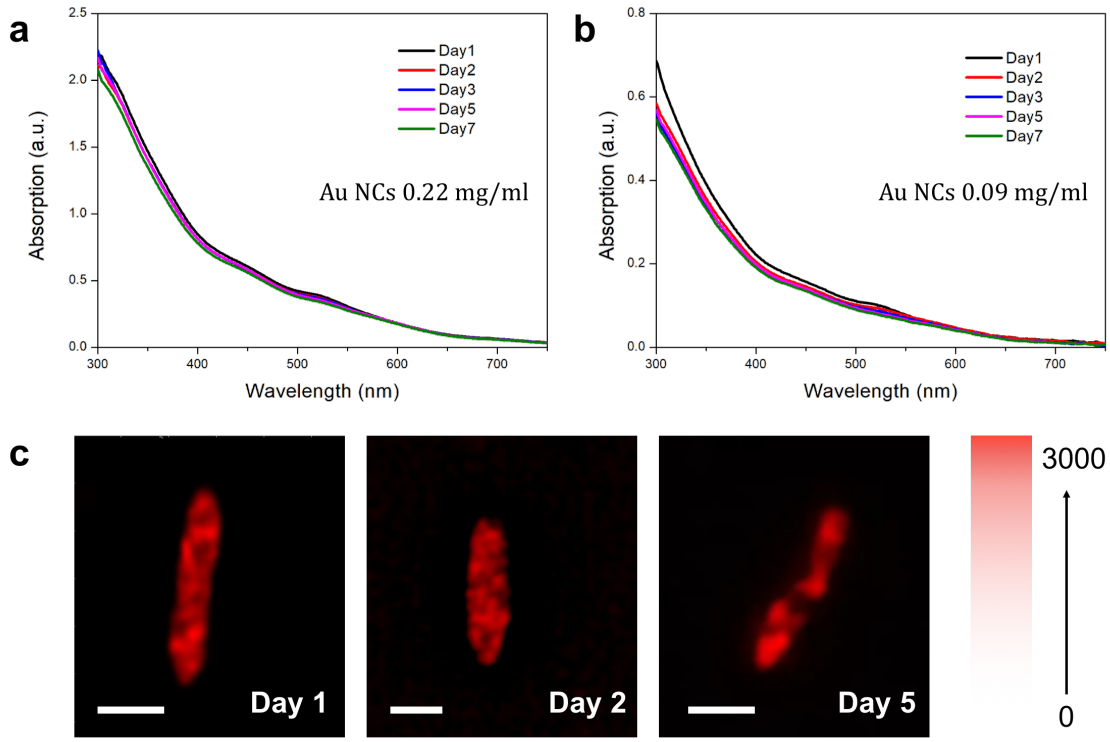

Fig. 2.9. Stability of Au NCs and intracellular Au NCs. The stability of Au NCs in the medium at different Au NCs concentration 0.22 mg/ml (**a**), 0.09 mg/ml (**b**), and the stability of intracellular Au NCs from day1 to day5 *via* the SIM images with the same excited energy and the same exposure time (**c**). Scale bar for c is 1 μm.

Section 2.4.3 Cell viability characterization

The viability of bacteria in different systems was also determined by bacteria enumeration using a Petroff-Hauser counting chamber in both dark and light conditions (Fig. 2.10a, b). First, in the dark incubator, bacteria were cultured in parallel in heterotrophic mediums for 2 days, and then, Au NCs solution, Cd^{2+} precursor solution, and blank water with the same volume were added accordingly. After keeping increasing for 12 hours, the bare *M. thermoacetica* and *M. thermoacetica*/Au NCs systems kept a relative high proliferation rate and cell viability until the fourth day, whereas the cell population of the *M. thermoacetica*-CdS system started to decline (Fig. 2.10a). This observation confirms the superior biocompatibility of the Au NCs. On the other hand, under the conditions of photosynthesis, we found that the bacteria population continued to increase in the first 12 hour, probably resulting from the completed division of already doubled yet not split bacteria. Thereafter, the population of viable bare *M. thermoacetica* dropped quickly due to the lack of heterotrophic substrates and potential photo-oxidative degradation. The viability of *M. thermoacetica*-CdS PBS declined after day 1 and cell concentration decreased to ~25% after 4 days (from the initial $8.9 \pm 0.2 \times 10^7$ cell ml^{-1}). Nevertheless, the cell ratio of *M. thermoacetica*/Au NCs kept higher than 100% within the first 2 days after which the cell amount slowly dropped to ~70% (from the initial $11.5 \pm 0.2 \times 10^7$ cell ml^{-1}).

Besides the low toxicity and good biocompatibility, Au NCs were also reported to possess the ability to quench reactive oxygen species (ROS)[24], such like NO• and •OH generated from the photo-oxidative degradation of metal clusters contained biomolecules under illumination[30]. The viability of *M. thermoacetica* could drop significantly with the existence of accumulated intracellular ROS. Therefore, we further applied ROS kit MAK 143 to assay the ROS level in the cytoplasm of *M. thermoacetica* by recording the intensity of ROS-triggered fluorescence emission. As shown in Fig. 2.10c, the ROS concentration in bare *M. thermoacetica* is 1.8 times higher than *M. thermoacetica*/Au NCs after they were illuminated for 48 hours. These significant differences reveal the beneficial effect of Au NCs on eliminating ROS in the *M. thermoacetica*/Au NCs system[31,32]. The hypothesis of ROS scavenging by Au NCs could attribute to its chemical catalytic property, which triggers the reactions between cysteine and radicals. The Au NCs with multiple energy levels are speculated to facilitate the electron transfer to neutralize the active species to stable states[33].

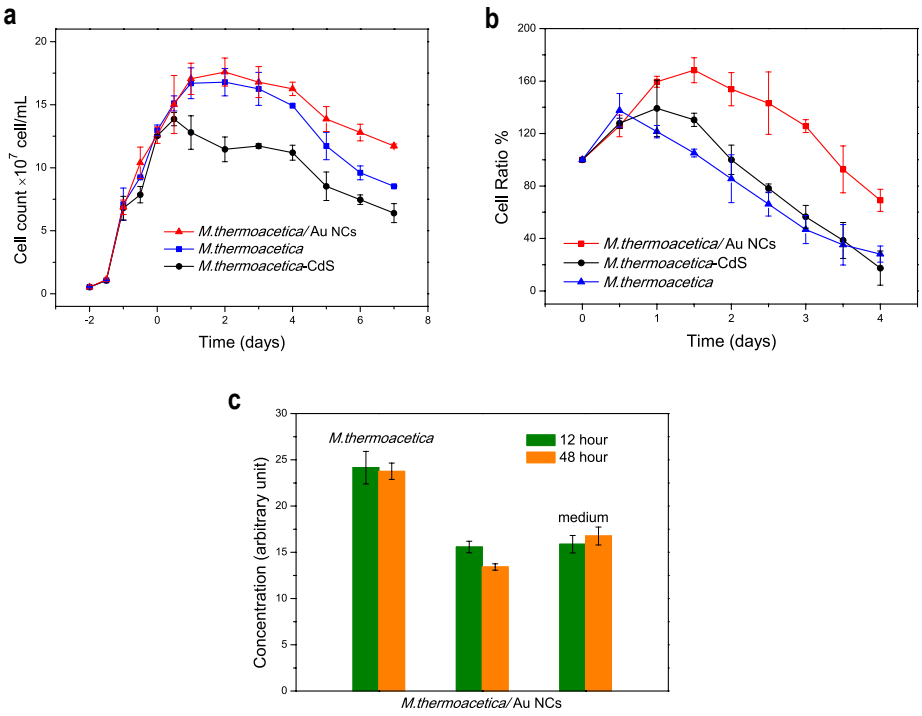

Fig. 2.10. The viability measurements. Bacterium enumeration of *M. thermoacetica*/Au NCs, *M. thermoacetica*-CdS, and bare *M. thermoacetia via* colony counting in the heterotrophic medium **a,** under dark condition, and **b,** in the autotrophic medium exposed to the low-intensity illumination (n = 20 culture batches for each condition). **c,** ROS concentration of bare *M. thermoacetia*, *M. thermoacetica*/Au NCs and medium under the low-intensity illumination for 12 h and 48 h respectively (n = 9). All points and error bars show the mean and error-propagated SD, respectively, of the experiments.

Section 2.5 Conclusions

In summary, we have developed and demonstrated that the Au NCs as an intercellular photosensitizer could facilitate the nonphotosynthetic bacterium, *M. thermoacetica,* to achieve

high efficiency photosynthesis. Small-sized Au NCs with high biocompatibility inside the bacterium enables the photosynthesis of acetic acid from CO_2. Moreover, the photo-generated electrons from intracellular Au NCs could be passed to cytoplasmic mediators in the Wood-Ljungdhal pathway, bypassing the slow mass transport and energy consumption across the cell membrane. Besides the intracellular-energy transfer, the continuous CO_2 fixation over six days benefited from the high viability of *M. thermoacetica*/Au NCs with Au NCs as the ROS scavenger.

Section 2.6 References

1. Blankenship, R. E. *et al.* Comparing photosynthetic and photovoltaic efficiencies and recognizing the potential for improvement. *Science* **332,** 805–809 (2011).
2. Appel, A. M. *et al.* Frontiers, opportunities, and challenges in biochemical and chemical catalysis of CO_2 fixation. *Chem. Rev.* **113,** 6621–58 (2013).
3. Sakimoto, K. K., Kornienko, N. & Yang, P. Cyborgian material design for solar fuel production: the emerging photosynthetic biohybrid systems. *Acc. Chem. Res.* **50,** 476–481 (2017).
4. Liu, C. *et al.* Nanowire-bacteria hybrids for unassisted solar carbon dioxide fixation to value-added chemicals. *Nano Lett.* **15,** 3634−3639 (2015).
5. Malvankar, N. S. & Lovley, D. R. Microbial nanowires for bioenergy applications. *Curr. Opin. Biotechnol.* **27,** 88–95 (2014).
6. Liu, C., Colon, B. C., Ziesack, M., Silver, P. A. & Nocera, D. G. Water splitting-biosynthetic system with CO_2 reduction efficiencies exceeding photosynthesis. *Science* **352,** 1210–1213 (2016).
7. Sakimoto, K. K., Wong, A. B. & Yang, P. Self-photosensitization of nonphotosynthetic bacteria for solar-to-chemical production. *Science* **351,** 74-77 (2016).
8. Gronenberg, L. S., Marcheschi, R. J. & Liao, J. C. Next generation biofuel engineering in prokaryotes. *Curr. Opin. Chem. Biol.* **17,** 462–471 (2013).
9. Lovley, D. R. Powering microbes with electricity: direct electron transfer from electrodes to microbes. *Environ. Microbiol. Rep.* **3,** 27–35 (2011).
10. Silhavy, T., Kahne, D. & Walker, S. The bacterial cell envelope. *Cold Spring Harb. Perspect. Biol.* **2,** 1–16 (2010).
11. Chen, L. Y., Wang, C. W., Yuan, Z. & Chang, H. T. Fluorescent gold nanoclusters: recent advances in sensing and imaging. *Anal. Chem.* **87,** 216–229 (2015).
12. Mathew, A. & Pradeep, T. Noble metal clusters: applications in energy, environment, and biology. *Part. Part. Syst. Charact.* **31,** 1–37 (2014).
13. Zhang, X. D. *et al.* Ultrasmall glutathione-protected gold nanoclusters as next generation radiotherapy sensitizers with high tumor uptake and high renal clearance. *Sci. Rep.* **5,** 8669 1–7 (2015).
14. Abbas, M. A., Kamat, P. V. & Bang, J. H. Thiolated Gold Nanoclusters for Light Energy Conversion. *ACS Energy Lett.* **3,** 840–854 (2018).
15. Abbas, M. A., Kim, T. Y., Lee, S. U., Kang, Y. S. & Bang, J. H. Exploring interfacial events in gold-nanocluster-sensitized solar cells: insights into the effects of the cluster size and electrolyte on solar cell performance. *J. Am. Chem. Soc.* **138,** 390–401 (2016).
16. Wang, J. *et al.* In vivo self-bio-imaging of tumors through in situ biosynthesized fluorescent gold nanoclusters. *Sci. Rep.* **3,** 1–6 (2013).

17. Durgadas, C. V, Sharma, C. P. & Sreenivasan, K. Fluorescent gold clusters as nanosensors for copper ions in live cells. *Analyst* **136,** 933–940 (2011).
18. Xie, J. *et al*. Identification of a highly luminescent $Au_{22}(SG)_{18}$ nanocluster. *J. Am. Chem. Soc.* **136,** 1246–1249 (2014).
19. Zhang, C. *et al.* Mimicking Pathogenic Invasion with the Complexes of Au 22 (SG) 18 - Engineered Assemblies and Folic Acid. *ACS Nano* **12,** 4408–4418 (2018).
20. Huang, B., Babcock, H. & Zhuang, X. Breaking the diffraction barrier: super-resolution imaging of cells. *Cell* **143,** 1047–1058 (2010).
21. Medintz, I. L., Uyeda, H. T., Goldman, E. R. & Mattoussi, H. Quantum dot bioconjugates for imaging, labelling and sensing. *Nat. Mater.* **4,** 435–446 (2005).
22. Chithrani, B. D. & Chan, W. C. W. Elucidating the mechanism of cellular uptake and removal of protein-coated gold nanoparticles of different sizes and shapes. *Nano Lett.* **7,** 1542–1550 (2007).
23. Kong, L. *et al*. Biocompatible glutathione-capped gold nanoclusters for dual fluorescent sensing and imaging of copper (II) and temperature in human cells and bacterial cells. *Microchim. Acta.* **183,** 2185–2195 (2016).
24. Lin, J. Zhang, H. Chen Z & Zheng, Y. Penetration of lipid membranes by gold nanoparticles: insights into cellular uptake, cytotoxicity, and their relationship. *ACS Nano* **4,** 5421–5429 (2010).
25. Kornienko, N. *et al.* Spectroscopic elucidation of energy transfer in hybrid inorganic-biological organisms for solar-to-chemical production. *Proc. Natl. Acad. Sci. U. S. A.* **113,** 11750–11755 (2016).
26. Deutzmann, J. S., Sahin, M. & Spormann, A. M. Extracellular enzymes facilitate electron uptake in biocorrosion and bioelectrosynthesis. *mBio* **6,** 1–8 (2015).
27. Pyo, K. *et al.* Ultrabright luminescence from gold nanoclusters: rigidifying the Au(I)-thiolate shell. *J. Am. Chem. Soc.* **137,** 8244–8250 (2015).
28. Das, A. & Ljungdahl, LG. Electron-transport system in acetogens. *Biochemistry and Physiology of Anaerobic Bacteria (Springer, New York)*, pp 191–204 (2003).
29. Negishi, Y., Nobusada, K. & Tsukuda, T. Glutathione-protected gold clusters revisited: Bridging the gap between gold(I)-thiolate complexes and thiolateprotected gold nanocrystals. *J. Am. Chem. Soc*. **127**, 5261–5270 (2005).
30. Jiang, Y. *et al.* Light-induced N_2O production from a non-heme iron-nitrosyl dimer. *J. Am. Chem. Soc.* **136,** 12524–12527 (2014).
31. Santiago-Gonzalez, B. *et al.* Permanent excimer superstructures by supramolecular networking of metal quantum clusters. *Science* **353,** 571–575 (2016).
32. Xiong, B., Xu, R., Zhou, R., He, Y. & Yeung, E. S. Preventing UV induced cell damage by scavenging reactive oxygen species with enzyme-mimic Au-Pt nanocomposites. *Talanta* **120,** 262–267 (2014).
33. Gao, Y., Shao, N., Pei, Y., Chen, Z. & Zeng, X. C. Catalytic activities of subnanometer gold clusters (Au_{16}-Au_{18}, Au_{20}, and Au_{27}-Au_{35}) for CO oxidation. *ACS Nano* **5,** 7818–7829 (2011).
34. Schuchmann, K. & Müller, V. Autotrophy at the thermodynamic limit of life: a model for energy conservation in acetogenic bacteria. *Nat. Rev. Microbiol*. **12**, 809–821 (2014).

Acknowledgments:

This work was supported by Director, Office of Science, Office of Basic Energy Sciences, Chemical Sciences, Geosciences, and Biosciences Division, of the U.S. Department of Energy under Contract No. DE-AC02-05CH11231, FWP No. CH030201 (Catalysis Research Program). We thank the imaging facilities at the National Center for Electron Microscopy (NCEM) at the Molecular Foundry and the NMR facility of the College of Chemistry, University of California, Berkeley. Work at the NCEM was supported by the Office of Science, Office of Basic Energy Sciences, of the U.S. Department of Energy under Contract No. DE-AC02-05CH11231. Research reported in this publication was supported in part by the National Institutes of Health S10 program under award number 1S10OD018136-01. The content is solely the responsibility of the authors and does not necessarily represent the official views of the National Institites of Health. H. Z. thanks the Suzhou Industry Park (SIP) fellowship.

Chapter 3. Cytoprotective Metal-Organic Frameworks for Anaerobic Bacteria

Key words: cell wrapping, metal-organic frameworks, artificial photosynthesis, anaerobic bacteria, reactive oxygen species

Section 3.1 Abstract

We report a strategy to uniformly wrap *Morella thermoacetica* bacteria with a metal-organic framework (MOF) monolayer of nanometer thickness for cytoprotection in artificial photosynthesis. The catalytic activity of the MOF enclosure toward decomposition of reactive oxygen species (ROS) reduces the death of strictly anaerobic bacteria by fivefold in the presence of 21% O_2, and enables the cytoprotected bacteria to continuously produce acetate from CO_2 fixation under oxidative stress. The high definition of the MOF-bacteria interface involving direct bonding between phosphate units on the cell surface and zirconium clusters on MOF monolayer, provides for enhancement of life throughout reproduction. The dynamic nature of the MOF wrapping allows for cell elongation and separation, including spontaneous covering of the newly grown cell surface. The open-metal sites on the zirconium clusters lead to 600 times more efficient ROS decomposition compared to zirconia nanoparticles.

Significance Statement

Culturing bacteria to produce desired chemicals has long been practiced in human history, and has recently being taken as a promising approach to sustainable energy when this process is driven by sunlight and fed by CO_2 as the only carbon source. Among these chemical-producing microbes are anaerobic bacteria, inherently susceptible to O_2 and reactive oxygen species that are inevitably generated on anodes. Here, we provide cytoprotection against such oxidative stress by wrapping bacteria with an artificial material, metal-organic frameworks (MOFs), which significantly enhances the lifetime of anaerobes in the presence of O_2, and maintains the continuous production of acetic acid from CO_2. The ultrathin nature of the MOF layer allows for cell reproduction without loss of this cytoprotective material.

Section 3.2 Introduction

Anaerobic bacteria have long been bred and used for fermenting organic matter in the absence of O_2 to produce value-added chemicals (ethanol, acetic acid, lactic acid, acetone, and butanol)[1]. Recent work on artificial photosynthesis takes advantage of the autotropic metabolism of these bacteria by employing CO_2 as the only carbon feed along with solar energy to produce fuels and chemicals[2-7]. Although these studies show promise, the evolution of O_2 and reactive oxygen species (ROS) at the anode along with fuel generation are detrimental to the metabolism of anaerobic bacteria. Addressing this inherent vulnerability to oxidative stress will expand the range and conditions for implementing a truly productive artificial photosynthesis. In this report, we show that by wrapping a semiconductor-sensitized anaerobic bacteria (*Moorella thermoacetica*) with a monolayer of a metal-organic framework (MOF), CO_2 was converted to acetate twice as long as that observed without such wrapping. We find a fivefold decrease in death of the wrapped bacteria when subjected to an O_2 environment (21%), and that they are also capable of reproduction without loss of the MOF. It is well established that the O_2 species can be converted

to H_2O_2 at the cell membrane[8]. In our system, this O_2-H_2O_2 conversion is followed by H_2O_2 decomposition on the zirconium oxide units of the MOF. This sequence of reactions, being mediated by the MOF, prevents the generation and accumulation of ROS, known to be detrimental to the bacteria, and therefore dramatically elongates the lifetime in oxidative environment. The high definition of the MOF monolayer structure allowed us to confirm that the Zr^{4+} of the MOF is bonded to the phosphate units on the cell wall, and that the dynamic chemistry of this bonding is the key to the observed increase in lifetime of the bacteria, effectiveness of the wrapping, and the facility of their reproduction.

It is known that bacteria can be coated with polymers, inorganic nanoparticles, and MOFs to enhance their viability under radiation, thermal, and mechanical stress[9-15], but not to address the critical issue of the oxidative stress in artificial photosynthesis. These coatings suffer from complicated synthetic procedure that yields either poor coverage or stiff shells of hundreds of nanometers in thickness, which trap cells in dormant state. As such, the protection provided by these materials is only temporary because the material coating needs to be repeated every time a new batch of cells is introduced. The fact the bacteria we report here were wrapped with only 1-2 nm MOF layer and the bonds at the bacteria-MOF interface are dynamic, leads to facile reproduction and maintains protection against oxidative stress. It is worth noting, the excess MOF in the culture media can wrap over newly grown cell surfaces to pass on this protection over generations of anaerobes.

Section 3.3 Experimental details

Section 3.3.1 Synthesis of MOF monolayer $Zr_6O_4(OH)_4(BTB)_2(OH)_6(H_2O)_6$.

The synthetic protocol was modified based on the reported literature[16]. The obtained MOF dispersion was repeatedly washed by centrifugation with DMF and then water. The washed MOF monolayer, as a white gel sitting at the bottom of the centrifuge tubes, was redispersed in 0.1 M HCl and heated at 90 °C overnight to remove formate ligands. The resulting suspension was filtrated over polyethersulfone membrane filters (pore size of 0.2 μm, STERLITECH) and washed with water. The filter cake, before getting dried, was redispersed in water and stored for further usage. The concentration of the obtained MOF monolayer dispersion in water was determined by measuring UV-Vis spectroscopy. The absorption coefficient at 280 nm was found to be 0.10 mg^{-1} L cm^{-1} by quantifying zirconium amount using ICP-AES. This value was then referred for further usage in the quantification of this material.

Synthesis of model compound ZrDMPO. A mixture of $ZrCl_4$ (10 mg) and dimethylphosphate (30 mg) in DMF (2 mL) was incubated at 85 °C for two days and rhombohedral single crystals were obtained. The crystals were washed with DMF and acetone before dried under vacuum.

Fluorescent labeling of MOF monolayer. Molecules containing carboxylate groups can bind to the MOF monolayer through the coordination bond between carboxylate moieties and zirconium clusters. For this purpose, 2-FITC-biphenyl-4,4'-dicarboxylic acid (FITC-H_2BPDC) was synthesized according to reported literature (27). To functionalize MOF monolayer with FITC-H_2BPDC, 20 mg of FITC-H_2BPDC was added into a solution of MOF (5 mg) in DMF (5 mL). The mixture was incubated at 85 °C for 24 hours before washing repeatedly by centrifugation

in DMF and water. The final MOF monolayer functionalized with FITC-BPDC was redispersed in water for further usage.

Section 3.3.2 Anaerobic bacteria culturing

The medium was prepared under anaerobic conditions with deionized (DI) water. The Hungate technique or an anaerobic chamber (Coy Laboratory Products, Inc.) was employed in all operations to prevent the exposure of anaerobic bacteria to oxygen. The recipe for a general broth is the same as before (6). To make the heterotrophic medium, 25 mL of 1 M glucose solution, 20 mL of 5 wt.% Cys·HCl solution, 800 mg of β-glycerophosphate·2Na·xH_2O, 500 mg of yeast extract (BD Biosciences), and 500 mg of tryptone (BD Biosciences) were added into 1 L of the general broth and stirred until fully dissolved. Anaerobic media were then dispensed under a mixed atmosphere (80:20 mixture of N_2: CO_2) into 16 x 125 mm Balch-type anaerobic culture tubes (Chemglass Life Sciences) with butyl rubber stoppers and screw caps, and 18 x 150 mm Balch-type anaerobic culture tubes (Chemglass Life Sciences) with butyl rubber stoppers and aluminum crimp seals. Media were then autoclaved for 15 min at 121 °C before use.

The initial inoculum of *M. thermoacetica* (ATCC 39073) was cultured in the heterotrophic medium, and the late log cultures were cryopreserved in a -80 °C freezer with 10% dimethyl sulfoxide as a cryoprotectant. To prepare *M. thermoacetica* cultures, 0.5 mL of the thawed cryopreserved stock of *M. thermoacetica* was inoculated in 10 mL of the anaerobic heterotrophic medium, and incubated with occasional agitation at 52 °C. The headspace of each tube was pressurized to 150 kPa with a flux of the mixed atmosphere (80:20 mixture of N_2:CO_2). After 2 days of growth (OD_{600} = 0.16), the culture was reinoculated at 5 vol.% into fresh heterotrophic medium, and incubated at 52°C. After the other two days of growth (OD_{600} = 0.38), the bacteria were centrifuged down at 2500 rpm for 10 min, washed and resuspended in an equivalent volume of heterotrophic medium.

Section 3.3.3 Wrapping MOF monolayer around *M. thermoacetica*

The bacteria culture in the heterotrophic medium was supplemented with MOF monolayer dispersion with the final concentration of 0.05 mg/mL. The tubes were returned to incubator at 52 °C and placed in the mini shaker (VMR) at a speed of 100 rpm for 1 h. The obtained wrapping system was directly used for viability test and photosynthesis. For structural characterization, the excess MOF in the media was removed by centrifugation at 1000 rpm for 30 min. The supernatant was collected and the centrifugation was repeated for three times. The salts in the obtained supernatant were removed by further centrifugation at 2500 rpm for 20 min. The precipitate was collected and the centrifugation was repeated for three times. Finally, the precipitate was redispersed in water for structural characterization.

Section 3.3.4 Physical and chemical characterization

Electron Microscopy: TEM Samples were prepared by dropping suspensions onto the 400 mesh copper grids with lacey carbon support. The grids were air dried for one day. Bright field TEM imaging was performed on a JEOL 2100-F 200 kV Field-Emission Analytical TEM equipped with Oxford INCA EDS X-ray detection system (Oxford Instruments, Abingdon, UK) at the Molecular Foundry at Lawrence Berkeley National Laboratory (Berkeley, CA, USA). High-angle

annular dark-field scanning TEM images and X-ray elemental mapping were acquired with a 1-nm probe at 200 kV. The specimens were tilted 10° toward the X-ray detector to optimize the X-ray detection geometry. Collection time was individually optimized for the best results. SEM samples were prepared by dropping suspensions onto the silicon wafer and air dried for one day. SEM images were recorded on a Zeiss Gemini Ultra-55 analytical SEM with accelerating voltage of 5 kV.

Optical Characterization: Super-resolution 3D-structured illumination microscopy (SIM) imaging was performed on a Zeiss ELYRA PS.1 system (Carl Zeiss). Images were acquired with a Plan-Apochromat 100x /1.40 oil immersion objective and an Andor iXon 885 EMCCD camera. A 100 mW 486 nm optically pumped semiconductor laser (Coherent Inc.) and a BP 510/620 nm emission filter (Optics Balzers AG, Balzers, Liechtenstein) were used. Thirty images with 86 nm z section were acquired for generating super resolution images. Raw images were reconstructed and processed to demonstrate structure with greater resolution by the ZEN 2011 software (Carl Zeiss), and the Imaris software was used to analyze the re-constructed images.

Chemical Characterization: Inductively coupled plasma atomic emission spectroscopy (ICP-AES, Optima 7000 DV, Perkin Elmer) was used to determine the amount of Zr in the material. The samples were digested in a solution mixture of nitric acid (0.5 mL) and hydrofluoric acid (0.1 mL). The resulting solution was filtered then diluted with 2% aqueous nitric solution to 10 mL before the measurement. All samples for PXRD were dried under vacuum before measurement. PXRD patterns were recorded using a Rigaku Miniflex 600 (Bragg-Brentano geometry, Cu Kα radiation λ = 1.54056 Å) instrument. The FT-IR spectra were collected on a Bruker ALPHA FT-IR Spectrometer equipped with ALPHA's Platinum ATR single reflection diamond ATR module, which can collect IR spectra on neat samples. XPS was obtained using an ultra-high vacuum (UHV) PHI 5400 XPS system with a non-monochromatic Al X-ray source (Kα = 1486.7 eV) operated at 350 W power. Survey XPS spectra were obtained with analyzer pass energy of 178.5 eV and step size of 1 eV. High resolution spectra of P 2p region were obtained with analyzer pass energy of 35 eV and 0.05 eV energy steps. The binding energy scale was corrected setting C 1s (sp2) peak in 284 eV (*Appendix*, Fig. A3.1). The peak fitting was performed using Casa XPS software.

For SXRD study, a colorless rhombohedral crystal (0.200 mm) was mounted on a Bruker D8 Venture diffractometer equipped with a finefocus Mo target X-ray tube operated at 40 W power (40 kV, 1 mA) and a PHOTON 100 CMOS detector. The specimen was cooled to 100 K using an Oxford Cryosystem chilled by liquid nitrogen. Bruker APEX2 software package was used for data collection; SAINT software package was used for data reduction; SADABS was used for absorption correction; no correction was made for extinction or decay. The structure was solved by direct methods in a rhombohedral space group R-3 with the SHELXTL software package and further refined with least squares method. All non-hydrogen atoms were refined anisotropically, all hydrogen were generated geometrically. The details of crystallography data are shown in *Appendix*, Table A3.1 and A3.2.

Section 3.3.5 Oxidative stress and cell viability test

The volumetric cell numbers were determined by the manual counting with a Petroff-Hauser counting chamber. In parallel, the colony forming unit (CFU) assays were performed by sampling

and inoculating 0.1 mL of *M. thermoacetica* and *M. thermoacetica*-MOF suspension into 5 mL of molten (T > 50 °C) agar broth supplemented with 40 mM glucose and 0.1 wt.% cysteine. Assay tubes were pressurized to 150 kPa with 80: 20 mixture of N_2: CO_2 and incubated vertically at 52 °C. After 3 days of growth, visible white, circular colonies were counted to determine the CFU (mL^{-1}) as a measure of cell number and viability.

The viability of *M. thermoacetica* and *M. thermoacetica*-MOF under different O_2 and H_2O_2 concentration was tested after the heterotrophic growth entered a stationary phase. The sterile O_2 was injected by syringe into the bacteria culture media until volumetric concentrations of 21% were reached in the headspace. H_2O_2 was introduced into the culture media by injection with syringe until concentrations reached 1 μM, 5 μM, and 50 μM.

The *E. coli*-MOF was prepared in the same way as *M. thermoacetica*-MOF. Zeiss Z1 AxioObserver inverted fluorescence microscope was used for measuring living cell cultures over extended periods of time. It is equipped with low-light digital image capture for both color and grayscale. The system is completely automated and can be programmed for long-term experiments on living cells. The 100 µL of *E. coli*-MOF was added into CellASIC® ONIX plate B04X, which is controlled by CellASIC Onix Microfluidics system to pump slight bacteria into the main culture chamber at certain time points. General bright field and excited fluorescence filed movies were collected via Hamamatsu 9100-13 EMCCD camera every 4 min under Zeiss definite focus.

Section 3.3.6 Photosynthesis characterization

The *M. thermoacetica*-CdS was prepared as the previous method[6]. Typically, 1 mM $Cd(NO_3)_2$ was added to the *M. thermoacetica* when OD_{600} reached 0.42. After 3 days of growth, the opaque yellow suspension revealed the formation of *M. thermoacetica*-CdS. The MOF cytoprotected PBS was prepared in the same way as shown above. Prior to photosynthesis, 0.2 wt.% cysteine was added to each tube. The sterilized O_2 was injected into each tube till 2% (v/v) to mimic the oxidative stress condition in the whole reaction. Each tube was stirred at 150 rpm and heated to a measured temperature of 55 °C by a stirring hot plate. The illumination source employed for simulated sunlight measurements was a collimated 75 W Xenon lamp (Newport, Corp.) with an AM 1.5 G filter. All light intensities were calibrated by a silicon photodiode (Hamamatsu S1787-04). Concentrations of photosynthetic products were measured by ^{1}H-qNMR with sodium 3-(trimethylsilyl)-2,2',3,3'-tetradeuteropropionate (TMSP-d_4, Cambridge Isotope Laboratories, Inc.) as the internal standard in D_2O. Spectra were processed using the MestReNova software.

Section 3.4 Results and discussion

Section 3.4.1 Wrapping structural characterization of MOF-bacteria system

In this study, we chose the MOF [$Zr_6O_4(OH)_4(BTB)_2(OH)_6(H_2O)_6$; BTB = 1,3,5-benzenetribenzoate] (Fig. 3.1a) for cell wrapping because the constituting zirconium clusters are of low toxicity and high stability. The fact that these clusters can be connected by BTB linkers into self-supporting monolayer[16] further makes this material an ideal candidate. To build the bacteria-MOF construct, we developed a new strategy through adding pre-synthesized MOF monolayer into the culture media of bacteria (Fig. 3.1b). This post-synthetic method, in contrast to the *in situ* growth of MOF shells on bacteria[10], allows the spontaneous wrapping to occur around the newly

grown cell surface, facilitated by the coordination bond between zirconium cluster and teichoic acid on cell wall (Fig. 3.1c). The accomplished MOF wrapping is envisioned to serve as cytoprotective layer due to its catalytic activity toward ROS decomposition reaction (Fig. 3.1d).

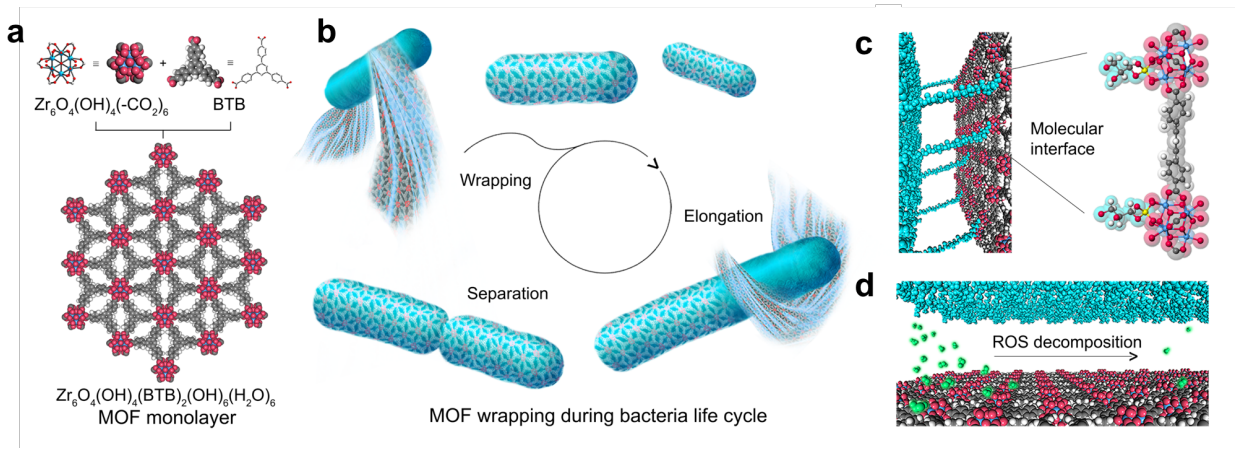

Fig. 3.1. Design and synthesis of the *M. thermoacetica*-MOF wrapping system. **a.** The MOF monolayer comprises 6-connected $Zr_6O_4(OH)_4(-CO_2)_6$ cluster and trigonal BTB linker. **b**. The monolayer of MOF spontaneously wraps around *M. thermoacetica*, allowing for elongation and separation of cells, during which newly formed cell surface is wrapped *in situ* by an excess of MOF in the culture medium. **c.** The molecular structure at the interface illustrates the multivalent coordination bonds form between the inorganic clusters of MOF and the phosphate moieties of teichoic acid on cell wall. **d**. Decomposition of ROS by the MOF monolayer coating on cell surface. In the space-filling model, atoms of cell wall and ROS are represented in cyan and green spheres, respectively. Hydrogen atoms on zirconium clusters are omitted for clarity. Color code: blue, Zr; red, O; grey, C; white, H; yellow, P.

The MOF monolayer was obtained using an established method[16]. Transmission electron microscopy (TEM) confirms the formation of the self-supporting MOF monolayer with lateral dimensions of microns (Fig. 3.2a). Early stationary stage *M. thermoacetica,* cultured in heterotrophic medium, was centrifuged down and redispersed together with MOF monolayers in the autotrophic culture medium. Upon gentle shaking, spontaneous wrapping was afforded over the course of one hour. The morphology of the resulting wrapping systems, *M. thermoacetica*-MOF, was examined by TEM (Fig. 3.2, *Appendix* Fig. A3.2), scanning transmission electron microscopy (STEM) (Fig. 3. 2), scanning electron microscopy (SEM) (Fig. 3.3), confirming that the bacteria were wrapped with ultrathin layers covering and further protruding from the whole body of the cell. The chemical composition of the wrapping construct was analyzed using energy-dispersive X-ray spectroscopy (EDXS) mapping (Fig. 3.2). The overlapping region of atomic distribution between zirconium, carbon, sulfur and phosphorus indicates the presence of MOF over the cell body. Structured illumination microscopy was employed to assess the structure of the heterogeneous wrapping system.

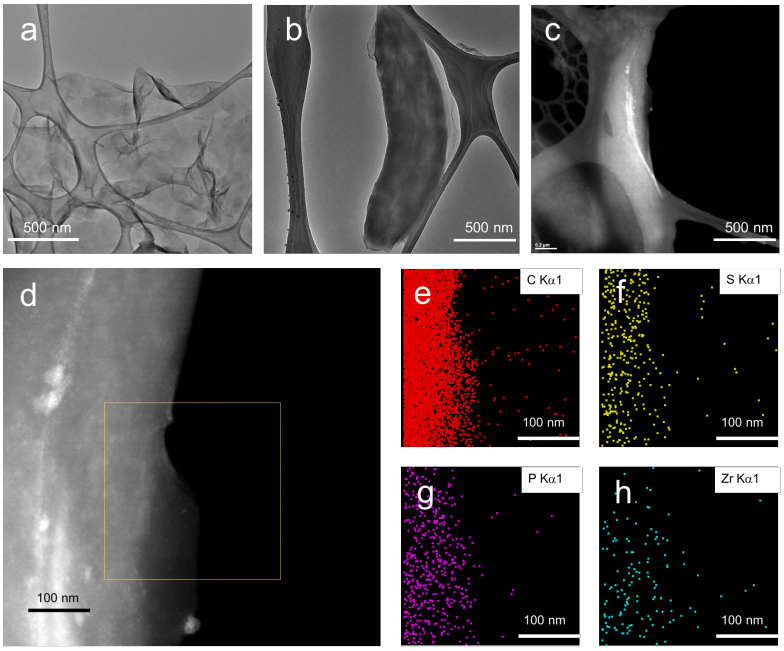

Fig. 3.2. Structural characterization of *M. thermoacetica*-MOF. **a.** TEM image of MOF monolayer. TEM image (**b**), and High-angle annular dark field (HAADF) STEM image (**c,d**), of *M. thermoacetica*-MOF. EDS mapping of the selected region labeled by yellow square in (**d**) confirms the presence of carbon (**e**), sulfur (**f**), phosphorus (**g**), and zirconium (**h**) on the edge of *M. thermoacetica*-MOF.

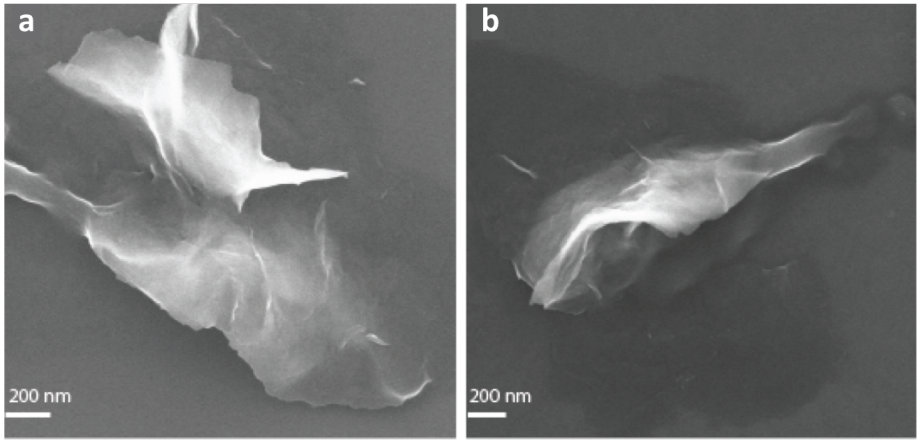

Fig. 3.3. SEM images of *M. thermoacetica*-MOF.

In order to double examine the wrapping systems, we labeled MOF monolayer and bacteria with fluorescein (Fig. 3.4a) and intracellular gold nanocrystals, emitting green and red fluorescence, respectively. The rebuilt 3D images (Fig. 3.4b) display a core-shell structure, further corroborating that the bacteria were wrapped by MOF.

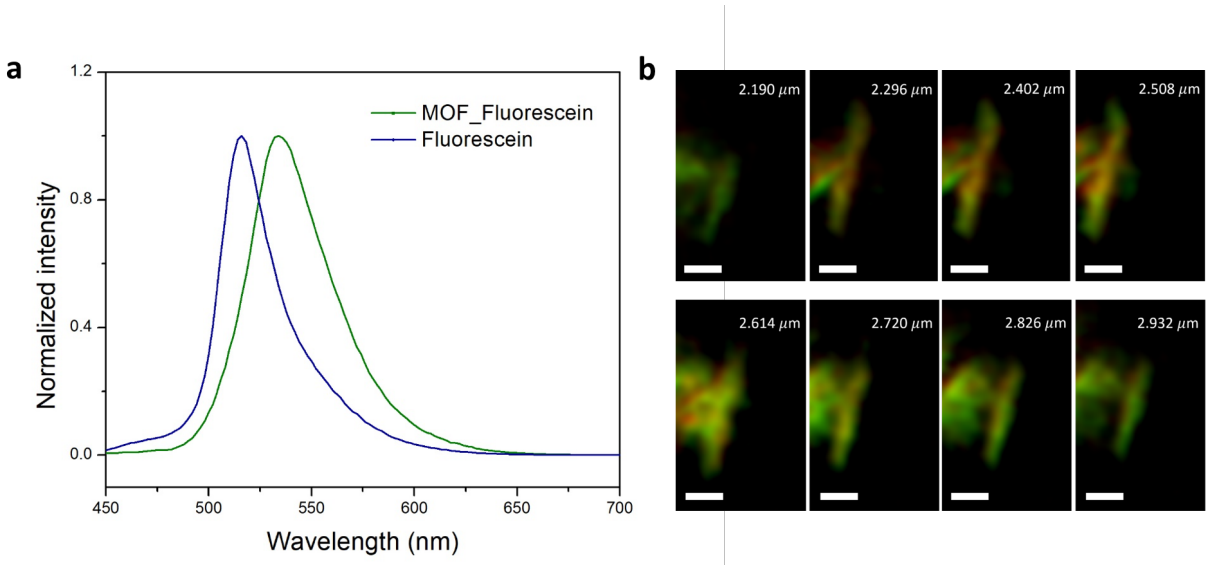

Fig. 3.4. Optical characterization of MOF wrapping systems. **a.** The Fluorescence spectra of the pristine fluorescein and fluorescein-functionalized MOF monolayer. **b.** Structure illumination microscopy images of *M. thermoacetica*-MOF wrapping system at different depth. MOF and the bacteria were labeled with green and red emission, respectively. Scale bars are 2 μm.

The crystallinity of MOF and *M. thermoacetica*-MOF were examined by powder X-ray diffraction (PXRD). The obtained PXRD patterns of the MOF soaked in culture media and the final wrapping construct *M. thermoacetica*-MOF were found to be in good agreement with that of the as-synthesized framework (Fig. 2*I*), confirming that the MOF remained intact during the cell wrapping process. The presence of the MOF was further confirmed by Fourier-transform infrared (FT-IR) spectra, where *M. thermoacetica*-MOF features aromatic C=C (1407 cm^{-1}) and C-H stretches (856 and 777 cm^{-1}) of the BTB linker (*Appendix*, Fig. A3.3). The weight percent of MOF monolayer in the resulting wrapping construct was determined by inductively coupled plasma atomic emission spectroscopy (ICP-AES) and found to be 6.0 ± 0.9%.

The spontaneous wrapping of MOF monolayer over bacteria is facilitated by the coordination sites on zirconium clusters where hydroxyl and water ligands can be readily replaced by phosphate groups[17] of teichoic acid on the cell surface[18,19]. To have the cell surface as the only phosphate-containing ligand, ☆-glycerophosphate, a nutrient component, was excluded from the culture medium during the wrapping process for structural assessment. FT-IR spectra of the resulting wrapping system (*M. thermoacetica*-MOF-NP) exhibits the appearance of a new peak at 839 cm^{-1}, which does not belong to either bacteria or MOF along (Fig. 3.5a). To identify its chemical nature, a molecular analog of the proposed *M. thermoacetica*-MOF fragment, zirconium dimethylphosphate (ZrDMPO), was synthesized and used as a model compound. The structure of ZrDMPO was solved by single-crystal X-ray diffraction (SXRD) (*Appendix*, Fig. A3.4, Table A3.1 and Table A3.2) and comprised of two oxygen atoms of DMPO coordinating to adjacent zirconium ions in a bidentate fashion. This very bonding was found to exhibit a (Zr)-O-P stretch at 839 cm^{-1} in the FT-IR spectrum[20], consistent with the new peak emerged from that of *M. thermoacetica*-MOF-NP (Fig. 3.5b). The coordination of glycerophosphate to zirconium cluster occurs when MOF was soaked alone in the culture media and displays a (Zr)-O-P stretch (832 cm^{-1}), which contributes to the broad peak at the same position in the FT-IR spectra of *M. thermoacetica*-MOF. This result indicates the presence of both glycerophosphate and cell surface bonding to the

zirconium clusters when the wrapping is processed in the complete culture media, between which the competition can enable a dynamic wrapping that allows for the elongation and separation of the cell wall. The presence of coordination bonds between phosphate moieties on the cell surface and zirconium clusters was corroborated by X-ray photoelectron spectroscopy (XPS) (Fig. 3.5c). The P 2p spectrum of *M. thermoacetica*-MOF-NP exhibits a binding energy shift from 132.8 eV to 133.1 eV relative to the bare bacteria, analogous to that of the model compound ZrDMPO with P 2p binding energy of 133.2 eV.

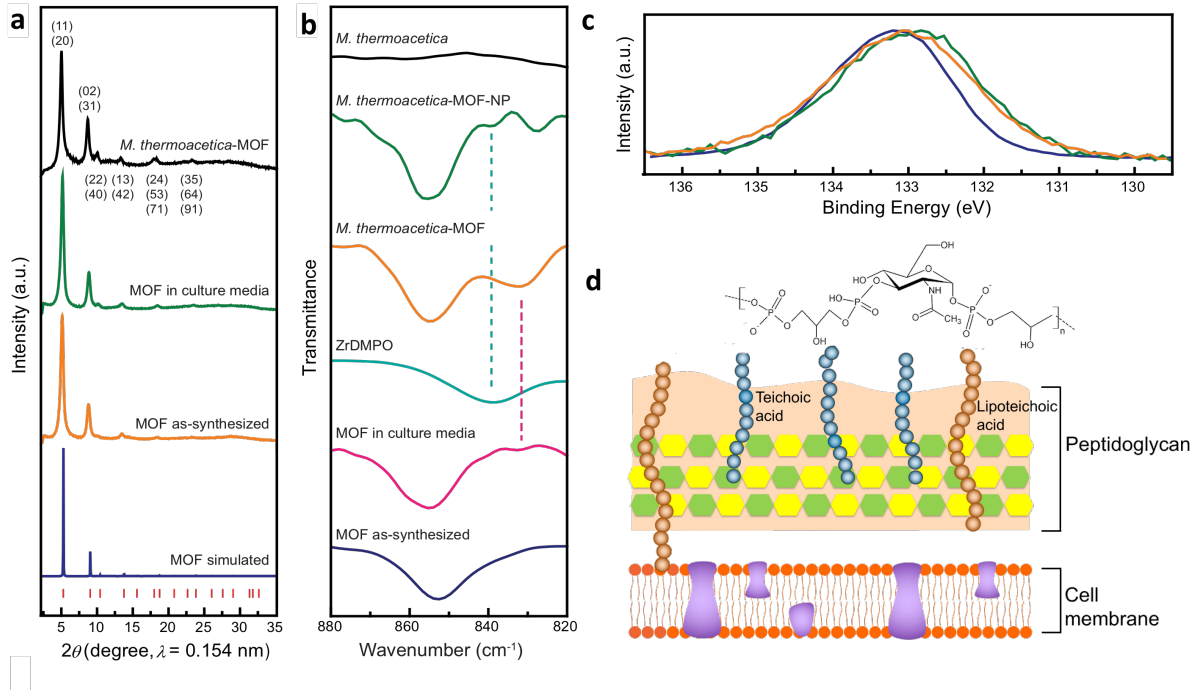

Fig. 3.5. Structural characterization of *M. thermoacetica*-MOF. **a.** PXRD pattern and Bragg position (red lines) of *M. thermoacetica*-MOF, MOF soaked in culture media, MOF as-synthesized, and the modeled structure. **b.** FT-IR spectra of *M. thermoacetica*, *M. thermoacetica*-MOF, *M. thermoacetica*-MOF cultured in phosphate-free medium (-NP), the model compound ZrDMPO, MOF soaked in culture media, and MOF as-synthesized. Peaks at 839 and 832 cm^{-1} are labeled with dashed lines in cyan and magenta, respectively. **c.** P 2p spectra obtained by XPS of ZrDMPO (blue), *M. thermoacetica*-MOF-NP (orange), and *M. thermoacetica* (green). **d.** The structure of cell membrane for Gram Positive bacteria.

Section 3.4.2 Cell viability characterization of MOF-bacteria system

To essay the biocompatibility of the MOF monolayer, heterotrophic growth of *M. thermoacetica* cultured under anaerobic conditions was profiled by counting colony formed units (CFU). *M. thermoacetica*-MOF was observed to exhibit a growth curve consistent with that of the bare bacteria (Fig. 3.6a), which reveals that the MOF wrapping maintains cell life and their reproductive capacity. This finding was supported by the observation that MOF monolayer permits the transportation of small molecules necessary for cell growth (*Appendix*, Fig. A3.5). The

reproduction process of *Escherichia. coli* wrapped by MOF monolayer in the microfluidic cell was recorded in a time-lapse video by labeling MOF with green fluorescence (Fig. 3c, *Appendix*, Movie 3.1 and Movie 3.2). The motion of the MOF enclosure was tracked and found to move in accordance to the elongation and separation of the cell surface, and carried by bacteria of next generations. When excess MOF monolayer are present in the culture media, the newly grown cell surface could be spontaneously covered. Therefore, the *in situ* wrapping process allows cell reproduction and guarantees the retention of cytoprotection in future generations.

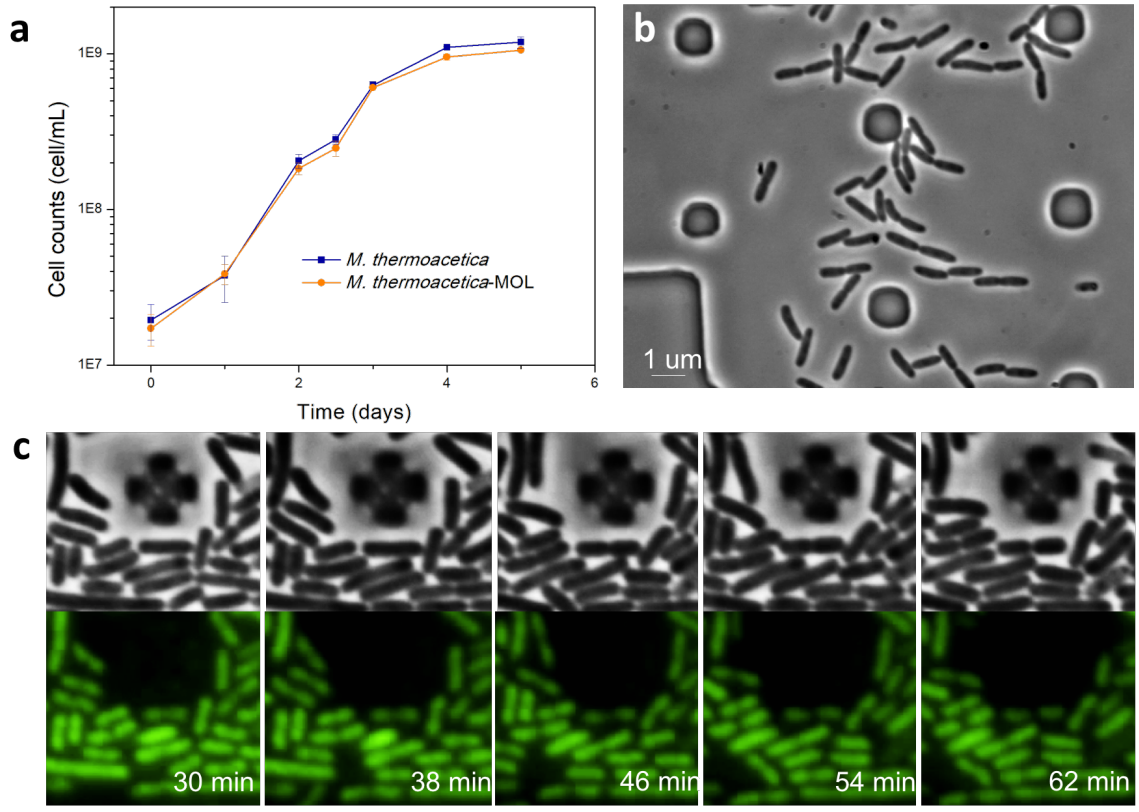

Fig. 3.6. MOF monolayer enclosure allows for the reproduction of bacteria. a. Heterotrophic growth curves of *M. thermoacetica* and *M. thermoacetica*-MOF under the anaerobic condition. **b.** Snapshots of the division process of *E. coli*-MOF captured in dark field (left) and fluorescence field (right). Scale bars: 1 μm.

Classified as strict anaerobes, several acetogenic bacteria used in artificial photosynthesis, including *M. thermoacetica* [6], have been reported to only tolerate low levels of O_2[8, 21, 22]. To investigate the cytoprotective effect of MOF enclosure on anaerobes under oxidative stress, *M. thermoacetica* cultures were subject to O_2 after reaching a stationary phase. It was observed that *M. thermoacetica* equipped with MOF enclosure cultured in 21% O_2 environment exhibit a high viability of 76 ± 8% after 2 days, which is comparable to the survival ratio of 83 ± 7% cultured under anaerobic conditions (Fig. 3.7a). In contrast, the population of the bare bacteria without this artificial enhancement decayed to 50 ± 7% when exposed to the same level of O_2, corresponding to a fivefold increase in death. Additionally, the defense of MOF enclosure against H_2O_2, a predominant ROS, was analyzed by feeding H_2O_2 into the culture media at the concentrations of 1

μM, 5 μM, and 50 μM. The cytoprotective MOF was found to result in a significantly improved viability of *M. thermoacetica* in these H_2O_2 media (Fig. 3.7b-c).

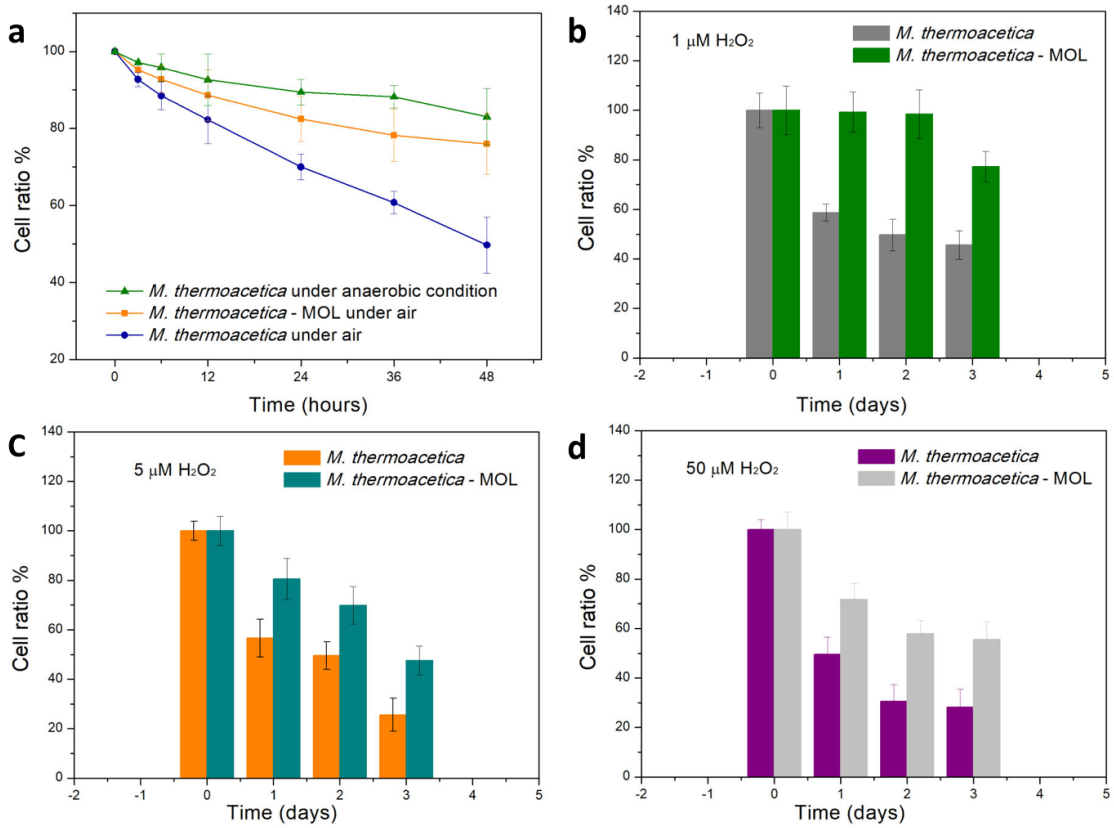

Fig. 3.7. MOF monolayer enhances the bacteria viability under oxidative stress. a. Cell population decay curves of *M. thermoacetica* and *M. thermoacetica*-MOF in air, and bare *M. thermoacetica* under anaerobic conditions. The viability of *M. thermoacetica* and *M. thermoacetica*-MOF in media containing H_2O_2 at concentrations of 1 μM (**b**) (*D*), 5 μM (**c**), and 50 μM (**d**). Error bars represent SD.

Section 3.4.3 Mechanism of cytoprotective property

The protection against oxidative stress by MOF monolayer might originate from its catalytic activity toward ROS decomposition due to the structural resemblance between zirconium clusters and active sites of zirconia[23]. Mechanistic studies of this process were performed by measuring the H_2O_2 concentration in MOF media, determined according to Ghormley triiodide method[24,25], at different time intervals. An initial rapid decrease in H_2O_2 concentration was observed, which is ascribed to the physical adsorption of H_2O_2 on the MOF surface (Fig. 3.8a). Once the physical adsorption reaches its equilibrium, the catalytic decomposition of H_2O_2 becomes dominant, which shows a first-order rate dependence on H_2O_2, analogous to what is observed for

zirconia[26]. The catalytic activity of the MOF monolayer is further quantified by the second-order rate constant, as k_2= 3.26 ± 0.04 ×10^{-9} m s^{-1} (Fig. 3.8b), a number that is 28 times higher than zirconia nanoparticles when normalized by the number of zirconium atoms on the surface, and 600 times higher when normalized by mass (see Materials and Methods).

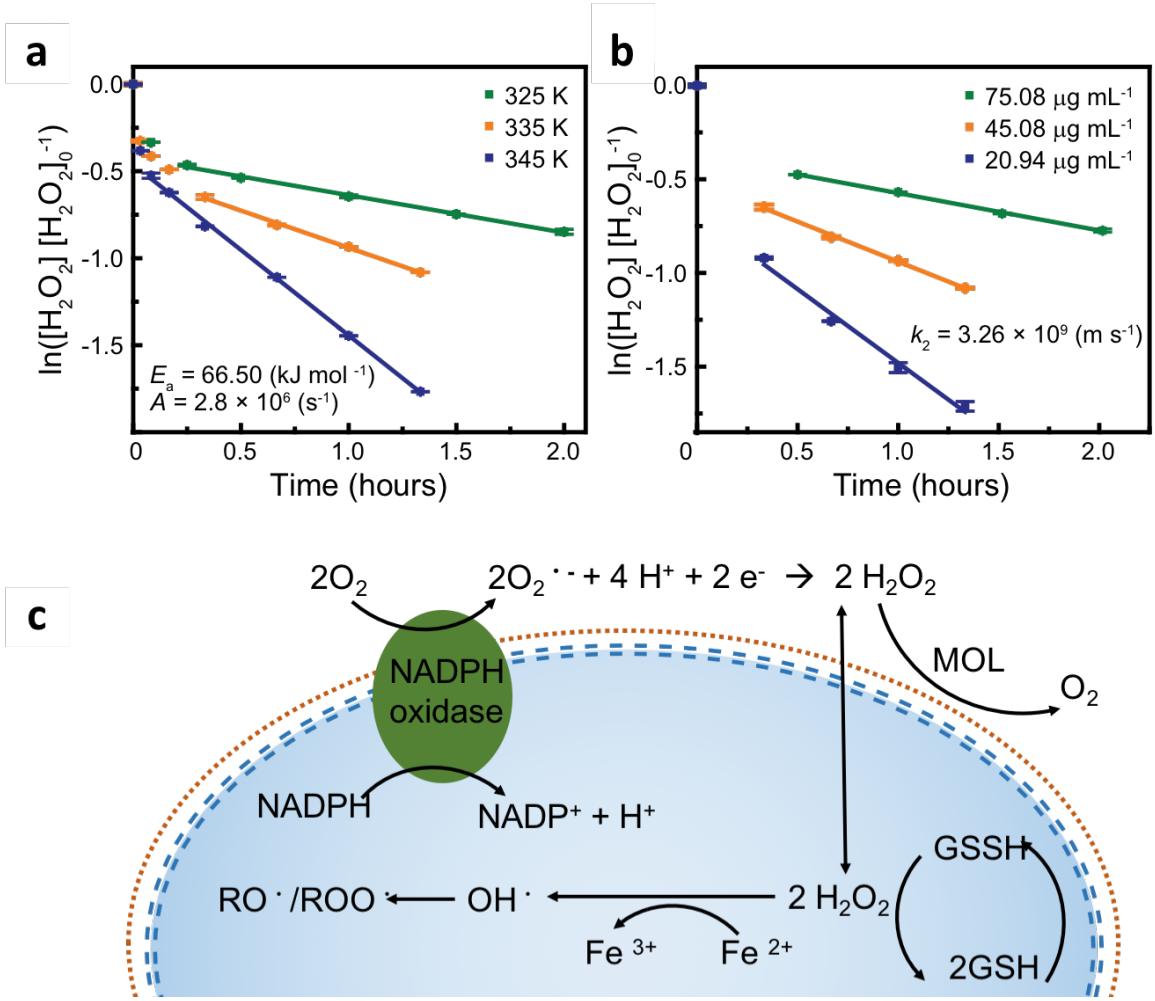

Fig. 3.8. The mechanism of protection against oxidative stress by MOF enclosure. Normalized concentration of H_2O_2 as a function of time in the decomposition reaction at different temperatures ([MOF] = 45.08 μg mL^{-1}) **a.** and at different concentrations of MOF (335 K) (**b**). The Arrhenius activation energy E_a, frequency factor A, and the second-order rate constant k_2 were determined. Error bars represent SD. **c.** The scheme of possible ROS deactivation process in MOF wrapping system.

The kinetics of the H_2O_2 decomposition reaction was measured by charging a 100 mL flask with various amount of MOF monolayer and Milli-Q water to make the final volume of 78.4 mL. The flask was closed with rubber septum, and heated in water bath set at specific temperatures under stirring at 750 rpm. After the MOF dispersion reaches the set temperature, 1.6 mL of H_2O_2 (1 mM) was instantly injected into the solution and timing was started. At different time intervals, 2 mL of the reaction mixture was sampled by syringe and filtered through PTFE membrane (pore size of 200 nm, Whatman). The H_2O_2 concentration in the obtained solution was determined

through Ghormley triiodide method[24, 25], in which I^- is oxidized quantitatively by H_2O_2 to I_3^-. Specifically, the sample solution was added with 100 μL of 1 M KI, 100 μL of a mixture solution containing 1 M sodium acetate and 1 M acetic acid, and adjusted to the final volume of 2 mL. The solution was left to react for 5 min before measuring the absorbance at 350 nm. A solution containing KI, sodium acetate, and acetic acid of the same concentration was prepared in parallel as blank control for background measurement. The molar extinction coefficient of I_3^- at 350 nm was taken as 25500 M^{-1} cm^{-1} for the calculation of H_2O_2 concentration.

It was reported in the literature[23] that the catalytic decomposition of H_2O_2 on zirconia follows first-order kinetics with respect to H_2O_2. When an excess of zirconia is present, the reaction kinetics can be approached to a pseudo-first order. As such, the concentration of H_2O_2 as a function of reaction time follows

$$\ln\left(\frac{[H_2O_2]}{[H_2O_2]_0}\right) = -k_1 t$$

where k_1 is the pseudo-first-order rate constant, t is the reaction time, $[H_2O_2]$ is the concentration of H_2O_2 at a reaction time t, and $[H_2O_2]_0$ is the concentration at $t = 0$. It was found that, after the adsorption of H_2O_2 on the surface of MOF reaches equilibrium, its concentration as a function of time shows good agreement with this first-order kinetic behavior (Fig. 3.8a). Calculating the slopes of such linear dependence affords k_1 at different temperatures (Fig. 3.9a), which follows Arrhenius equation

$$\ln(k_1) = -\frac{E_a}{R}\frac{1}{T} + \ln(A)$$

where E_a is the Arrhenius activation energy, R is the gas constant, A is the frequency factor, and T is the absolute temperature. Extracted from this dependence of rate constant on temperature are E_a as 66.50 ± 0.07 kJ mol^{-1} and A to be 2.8 ± 0.1×10^6 s^{-1}. By varying the amount of MOF used as catalyst, the second-order rate constant k_2 was obtained by studying the pseudo-first-order rate constant as a function of the surface-area-to-solution-volume ratio of MOF according to

$$k_1 = k_2\left(\frac{S_A}{V}\right)$$

where S_A is the surface area of MOF and V is the volume of the reaction mixture. Using the specific surface area of MOF, S_{MOF}, this equation can be expressed as

$$k_1 = k_2\left(\frac{S_{MOF}[MOF]}{V}\right)$$

where [MOF] denotes the concentration of MOF. Taking S_{MOF} = 883 m^2 g^{-1} [16], the k_2 obtained from the slope of Fig. 3.9b for the reaction at 335 K is k_2 = 3.26 ± 0.04 ×10^{-9} m s^{-1}. This value represents the intrinsic catalytic activity of MOF to the decomposition reaction of H_2O_2. To compare the catalytic activity between MOF and zirconia, we take k_2 of zirconia at the same temperature as 9.66 ×10^{-10} m s^{-1} from the literature[23]. We further calculate the zirconium atom density of MOF monolayer as 0.91 nm^{-2} and that of (001) facet of monolithic zirconia as 7.5 nm^{-2} according to their crystal structures. By using these values, the k_2 of MOF monolayer normalized by zirconium atom numbers are obtained as 3.6 ×10^{-27} m^3 s^{-1}, 28 times higher than that of zirconia (1.3 ×10^{-28} m^3 s^{-1}). When normalized by mass, compared with zirconia nanoparticle of 5 m^2 g^{-1} in surface area[23], the k_2 of MOF monolayer is 600 times higher.

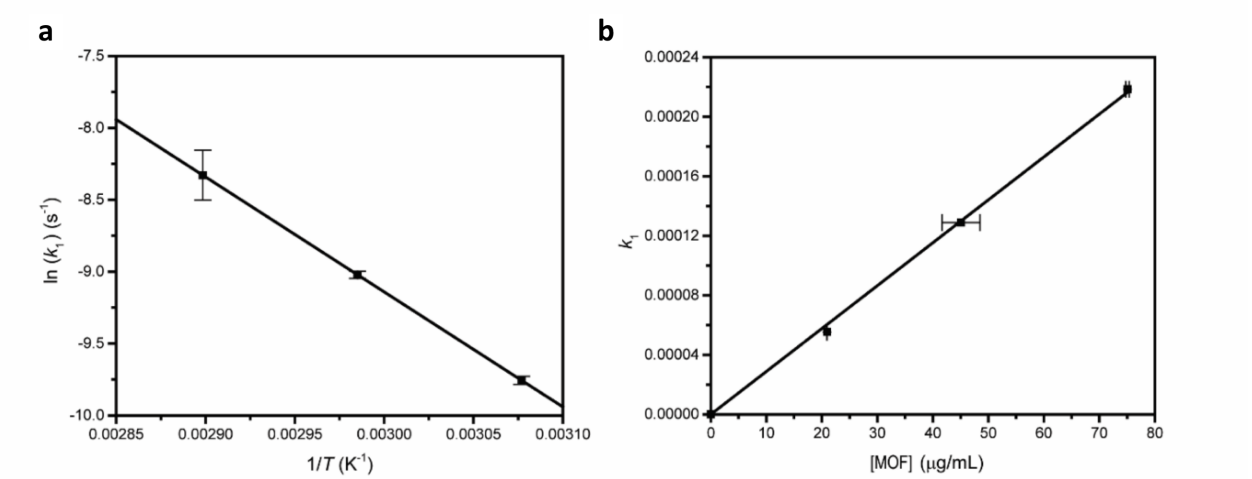

Fig. 3.9. Kinetics of H_2O_2 decomposition catalyzed by MOF monolayer.

The catalytic performance of MOF monolayer is vital to the enhanced tolerance of the anaerobes against oxidative stress. When anaerobes such as *M. thermoacetica* are exposed to O_2, H_2O_2 can be generated by NADH oxidase[8] on the cell membrane and diffuse into the cell. Once the amount of H_2O_2 exceeds the buffering capacity of glutathione, it poses a threat to cell survival by its transformation into toxic hydroxyl radical through Fenton's reaction. In our system, we demonstrate that the O_2-H_2O_2 conversion is followed by H_2O_2 decomposition on the zirconium oxide units of the MOF. This sequence of reactions, being mediated by the MOF, prevents the accumulation of ROS and therefore dramatically elongates the lifetime in oxidative environment. The enhanced tolerance of *M. thermoacetica* against oxidative stress holds the promise in facilitating the whole reaction of the photosynthesis of acetate from CO_2 in conjugation with oxygen evolution reaction. To show the proof of concept, into our previous photosynthetic biohybrid system (PBS)[6] was injected 2% O_2 to mimic the atmosphere of the whole photosynthetic reaction. It was found that the bare PBS without the cytoprotective MOF wrapping can only be functional to fix CO_2 into acetate within the first day (Fig. 3.10). The short lifetime of PBS is due to the cytotoxicity of O_2 and ROS generated along with photosynthesis. In contrast, the MOF wrapping maintains the photosynthesis by PBS for 2.5 days under the same condition, and increases the productivity of acetate to 200%.

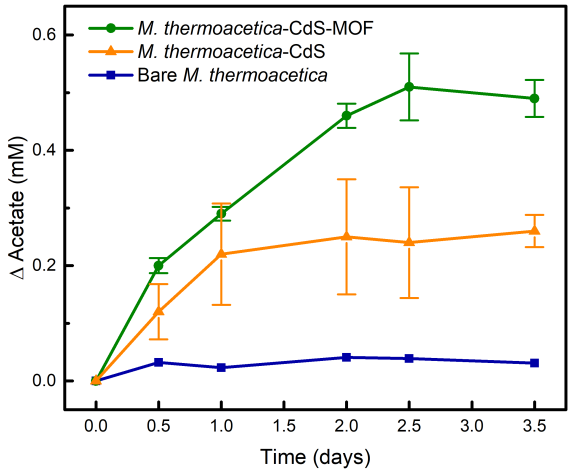

Fig. 3.10. The Yield of acetate in the half photosynthetic reaction catalyzed by *M. thermoacetica*-CdS-MOF, *M. thermoacetica*-CdS, and bare *M. thermoacetica* under the atmosphere of oxygen (2%).

Section 3.5 References

1. Zeikus, J. G. Chemical and fuel production by anaerobic bacteria. *Ann Rev Microbiol.* **34**, 423-464 (1980).
2. Torella, J. P. *et al*. Efficient solar-to-fuels production from a hybrid microbial–water-splitting catalyst system. *Proc Natl Acad Sci USA*. **112,** 2337-2342 (2015).
3. Liu, C. *et al*. Nanowire−bacteria hybrids for unassisted solar carbon dioxide fixation to value-added chemicals. *Nano Let.* **15**, 3634-3639 (2015).
4. Nichols, E. M. *et al*. Hybrid bioinorganic approach to solar-to-chemical conversion. *Proc Natl Acad Sci USA*. **112**, 11461-11466 (2015).
5. Liu, C., Colon, B. C., Ziesack M, Silver PA, Nocera DG. Water splitting–biosynthetic system with CO_2 reduction efficiencies exceeding photosynthesis. *Science.* **352**. 1210-1213 (2016).
6. Sakimoto, K. K., Wong, A. B., Yang, P. Self-photosensitization of nonphotosynthetic bacteria for solar-to-chemical production. *Science.* **351,** 74-77 (2016).
7. Sakimoto, K. K., Zhang, S. J., Yang, P. Cysteine−cystine photoregeneration for oxygenic photosynthesis of acetic acid from CO_2 by a tandem inorganic−biological hybrid system. *Nano Let*. **16**, 5883-5887 (2016).
8. Karnholz, A., Küsel, K., Gößner, A., Schramm, A., Drake HL. Tolerance and metabolic response of acetogenic bacteria toward oxygen. *Appl Environ Microbiol.* **68,** 1005-1009 (2002).
9. Ai, H., Fang, M., Jones, S. A., Lvov, Y. M. Electrostatic layer-by-layer nanoassembly on biological microtemplates: platelets. *Biomacromolecule.* **3,** 560-564 (2002).
10. Liang, K. *et al.* Metal–organic framework coatings as cytoprotective exoskeletons for living cells. *Adv Mater.* **28,** 7910-7914 (2016).

11. Liang, K. *et al.* An enzyme-coated metal–organic framework shell for synthetically adaptive cell survival. *Angew Chem Int Ed.* **129,** 8630-8635 (2017).
12. Liu, Z., Xu, X., Tang, R. Improvement of biological organisms using functional material shells. *Adv Func Mater.* **26,** 1862-1880 (2016).
13. Park, J. H. *et al.* Nanocoating of single cells: from maintenance of cell viability to manipulation of cellular activities. *Adv Mater.* **26,** 2001-2010 (2014).
14. Yang, S. H. *et al.* Biomimetic encapsulation of individual cells with silica. *Angew Chem Int Ed.* **48,** 9160-9163 (2009).
15. Elani, Y. *et al.* Constructing vesicle-based artificial cells with embedded living cells as organelle-like modules. *Sci Rep.* **8,** 4564 (2018).
16. Cao, L. *et al.* Self-supporting metal–organic layers as single-site solid catalysts. *Angew Chem Int Ed.* **55,** 1-6 (2016).
17. Wang, Z. *et al.* Organelle-specific triggered release of immunostimulatory oligonucleotides from intrinsically coordinated DNA-metal-organic frameworks with soluble exoskeleton. *J Am Chem Soc.* **139,** 15784-15791(2017).
18. Heptinstall, S., Archibald, A. R., Baddiley, J. Teichoic acids and membrane function in bacteria. *Nature.* **225,** 519-521 (1970).
19. Brown, S., Santa Maria, J. P., Walker, S. Wall teichoic acids of gram-positive bacteria. *Annu Rev Microbiol.* **67,** 313-336 (2013).
20. Kim, H., Keller, S. W., Mallouk, T. E. Characterization of zirconium phosphate/polycation thin films grown by sequential adsorption reactions. *Chem Mater.* **9,** 1414-1421 (1997).
21. Boga, H. I., Brune, A., Hydrogen-dependent oxygen reduction by homoacetogenic bacteria isolated from termite guts. *Appl Environ Microbiol.* **69,** 779-786 (2003).
22. Das, A., Silaghi-Dumitrescu, R., Ljungdahl, L. G., Kurtz, D. M., Cytochrome *bd* oxidase, oxidative stress, and dioxygen tolerance of the strictly anaerobic bacterium *Moorella thermoacetica. J Bacteriol.* **187,** 2020-2029 (2005).
23. Lousada, C. M., Johansson, A. J., Brinck, T., Jonsson, M. Mechanism of H_2O_2 decomposition on transition metal oxide durfaces. *J Phys Chem C.* **116,** 9533-9543 (2012).
24. Ghormley, J. A., Stewart, A. C. Effects of radiation on ice. *J Am Chem Soc.* **78,** 2934-2939 (1956).
25. Diesen, V., Jonsson, M. Formation of H_2O_2 in TiO_2 photocatalysis of oxygenated and deoxygenated aqueous systems: a probe for photocatalytically produced hydroxyl radicals. *J Phys Chem C.* **118,** 10083-10087 (2014).
26. Lousada, C. M., Jonsson, M. Kinetics mechanism and activation energy of H_2O_2 decomposition on the surface of ZrO_2. *J Phys Chem C.* **114**, 11202-11208 (2010).
27. Schrimpf, W. *et al.* Chemical diversity in a metal–organic framework revealed by fluorescence lifetime imaging. *Nat Commun.* **9,** 1647 (2018).

Acknowledgments This research was supported by BASF SE (Ludwigshafen, Germany) for synthesis and characterization of MOFs, by King Abdulaziz City for Science and Technology (Center of Excellence for Nanomaterials and Clean Energy Applicatioins) for mechanistic studies, and by National Aeronautics and Space Administration (NASA), Center for the Utilization of Biological Engineering in Space (CUBES) under award No. NNX17AJ31G for bacteria study. H. Z. thanks the Suzhou Industry Park (SIP) fellowship. SEM, XPS, and STEM measurements were performed at the Molecular Foundry, Lawrence Berkeley National Laboratory. We thank J. Baek and B. Rungtaweevoranit (Yaghi group) for the acquisition of XPS data and SEM images, C. Zhao (Yaghi group) for help in mechanistic studies of H_2O_2 decomposition by MOF, C. S. Diercks (Yaghi group) for discussions, and C. Chen (Peidong group) for cell culture and enumeration.

Appendix

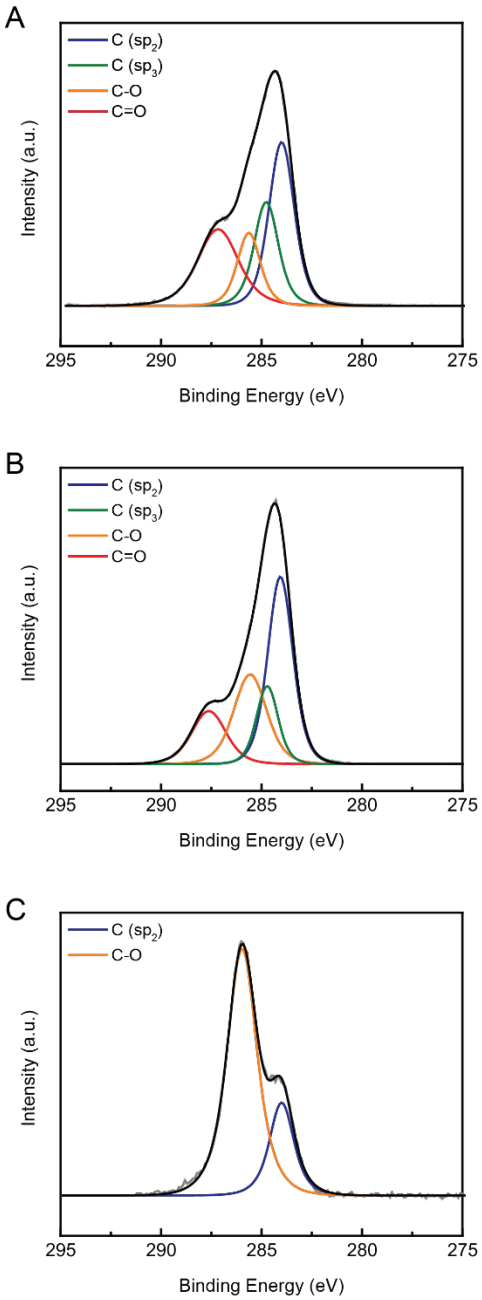

Fig. A3.1. C 1s Spectra obtained by XPS for *M. thermoacetica* (*A*), *M. thermoacetica*-MOF (*B*), and ZrDMPO (*C*). Deconvolution of the spectra indicates higher amount of C (sp_2) in *M. thermoacetica*-MOF compared with bare bacteria due to the contribution by the phenyl rings in BTB linkers of the MOF. The C (sp_2) peak in ZrDMPO comes from the signal of the carbon tape. The C (sp_2) peaks of all the samples are used for the calibration of binding energy and set as 284.0

eV. The original spectra are plotted in grey lines and the integrations of the fitted peaks are plotted in black lines.

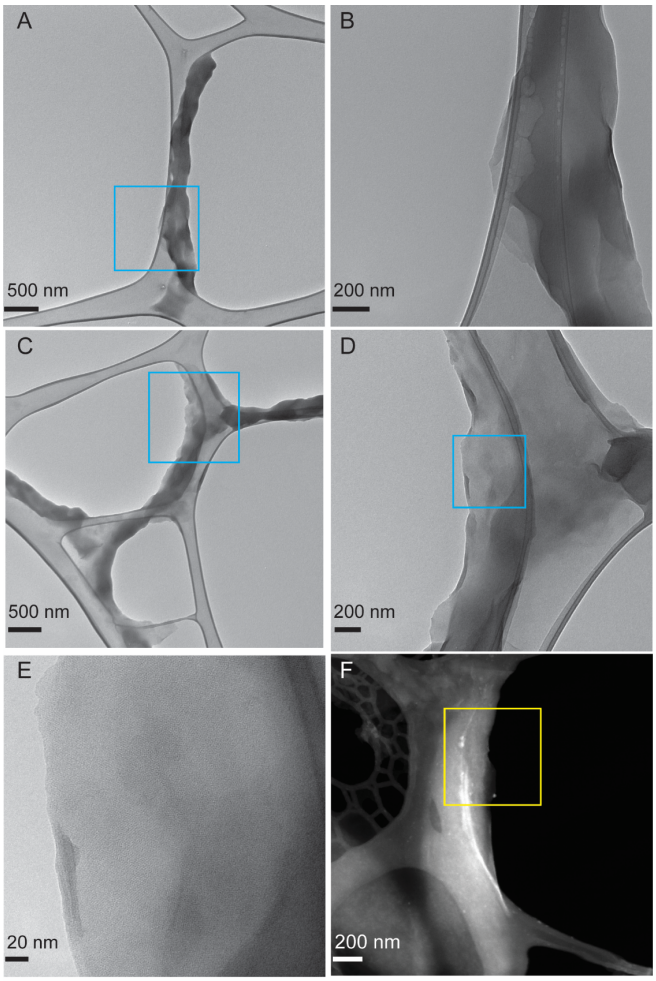

Fig. A3.2. (*A*-*C*) SEM images of *M. thermoacetica*-MOF

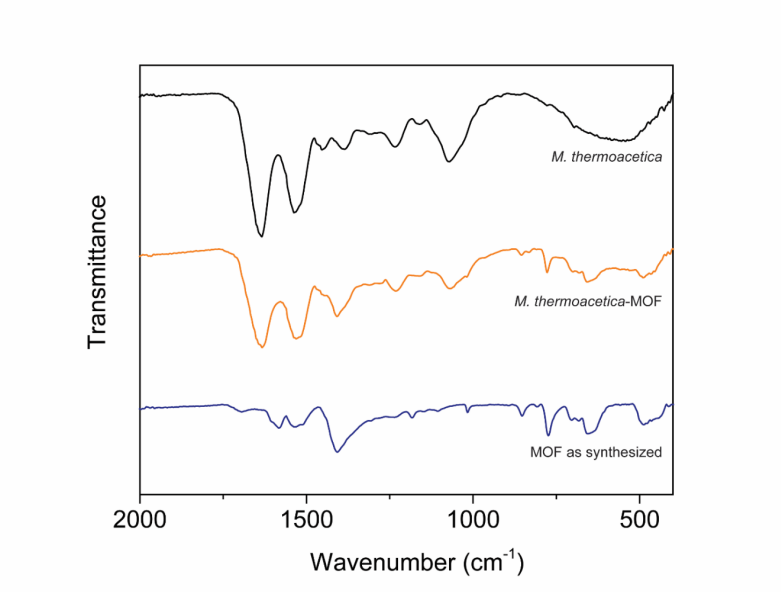

Fig. A3.3. FT-IR spectra of *M. thermoacetica*, *M. thermoacetica*-MOF, and MOF as synthesized.

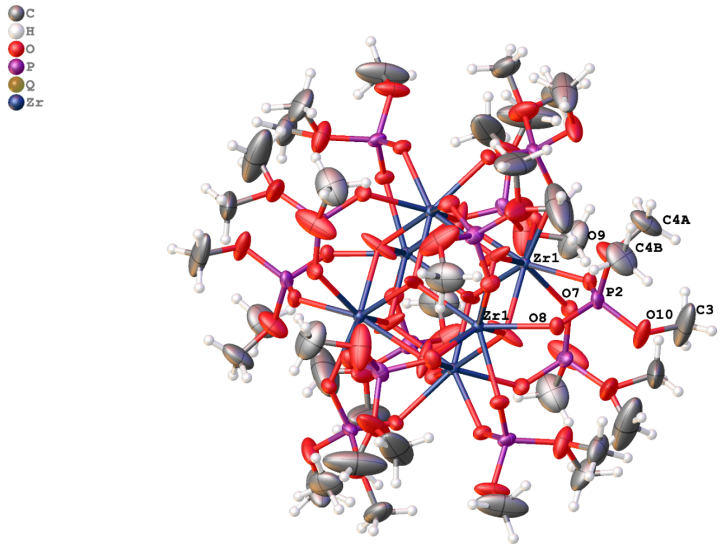

Fig. A3.4. The crystal structure of ZrDMPO. Thermal ellipsoids are shown with 50% probability.

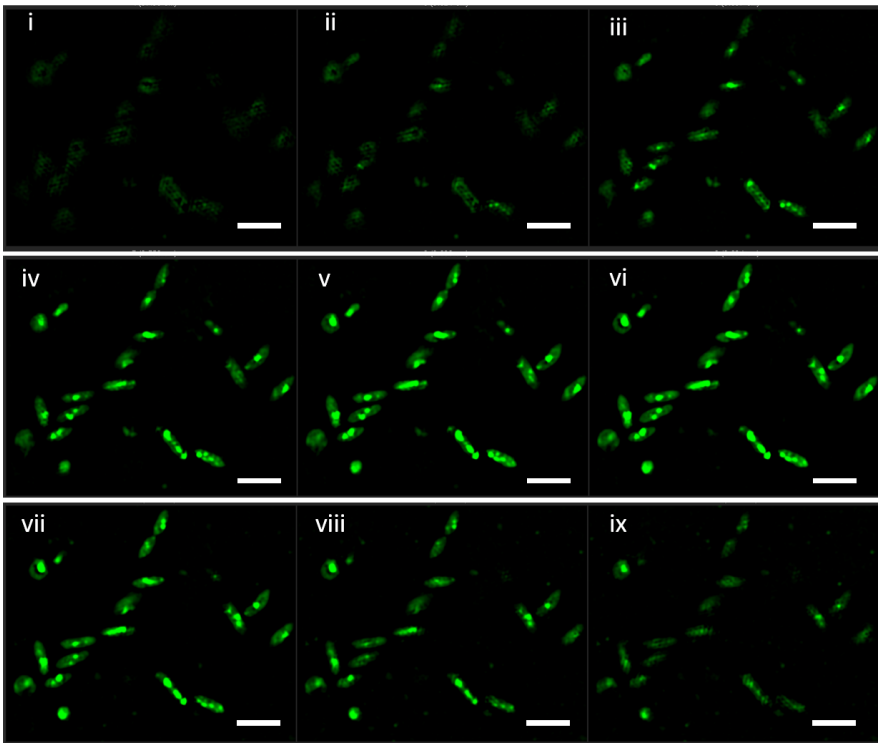

Fig. A3.5. Structured illumination microscopy images of *M. thermoacetica*-MOF wrapping system feeding with fluorescent dye with green emission at different depth (from i to ix), confirming the presence of the dye molecule in the cell. This observation indicates the MOF enclosure allows for the transportation of small molecules, including nutrients, to enter the enclosed cell. Scale bars are 4 **μ**m.

Table A3.1. Crystal data and structure refinement ZrDMPO

Chemical formula	$C_4H_{12}O_{9.33}P_2Zr$
Formula weight	362.63
Temperature/K	100
Crystal system	trigonal
Space group	R-3
a/Å	20.3072(10)
b/Å	20.3072(10)
c/Å	14.9882(8)
α/°	90
β/°	90
γ/°	120
Volume/Å^3	5352.8(6)
Z	18
ρ_{calc}g/cm^3	2.025

μ/mm^{-1}	1.226
F(000)	3252.0
Crystal size/mm^3	0.2 × 0.2 × 0.2
Radiation	Mo Kα (λ = 0.71073)
2Θ range for data collection/°	5.372 to 52.036
Index ranges	$-25 \leq h \leq 25$, $-25 \leq k \leq 23$, $-18 \leq l \leq 18$
Reflections collected	15918
Independent reflections	2354 [R_{int} = 0.0218, R_{sigma} = 0.0145]
Data/restraints/parameters	2354/0/174
Goodness-of-fit on F^2	1.071
Final R indexes [I>=2σ (I)]	R_1 = 0.0286, wR_2 = 0.0679
Final R indexes [all data]	R_1 = 0.0308, wR_2 = 0.0696
Largest diff. peak/hole / e $Å^{-3}$	0.73/-0.84

Table A3.2. Selected Structural Data for ZrDMPO

	Length/Å
Zr(1)-O(7)	2.194(2)
Zr(1)-O(8)	2.211(2)
P(2)-O(7)	1.494(2)
P(2)-O(8)	1.491(2)
P(2)-O(9)	1.580(3)
P(2)-O(10)	1.553(3)
O(10)-C(3)	1.400(5)
O(9)-C(4A)	1.337(12)
O(9)-C(4B)	1.375(8)

	Angle/°
P(2)-O(7)-Zr(1)	133.20(12)
P(2)-O(8)-Zr(1)	133.38(12)
O(8)-P(2)-O(7)	117.08(12)
O(10)-P(2)-O(9)	105.87(19)
C(3)-O(10)-P(2)	123.0(3)
C(4A)-O(9)-P(2)	127.8(7)
C(4B)-O(9)-P(2)	122.6(4)

Chapter 4. Ultrafast Studies of Photoinduced Excited States of Au Nanocluster in Model System

Section 4.1 Introduction

In the past several decades, nanomaterials have elucidated new frontiers in energy science, biochemistry, drug delivery, and engineering[1-7]. Different from the traditional nanoparticles with size larger than 3 nm, atomically precise metal nanoclusters have emerged as a new type of materials which attracts tremendous attention. Metal nanoclusters with size ranging between sub nm to 3 nm, present the unique optical and electronic properties compared to nanoparticles, and therefore, the nanocluster exploration provides an important link between metal nanoparticles and single atoms. In particular, thiol-protected gold nanoclusters ($Au_n(SR)_m$) have received a lot of attention in recent years due to their application in catalysis[1], optics[2,3], solar energy harvesting for photovoltaics[4-6], and photocatalysis[7-9]. Due to surface plasmon resonance, gold nanoparticles display visible light absorbance, which has become well understood and exploited in various applications like surface enhance Raman spectroscopy. When the size scales down to 3 nm, gold nanoparticles no longer support plasmon absorption but present the molecular-like optical properties, which is regard as the special molecule-like transitions of gold nanoclusters (AuNCs)[10,11].

Due to the precise synthetic method, AuNCs with different size could be controlled and stabilized by either hydrophilic or hydrophobic ligands[12]. Most AuNCs follow a "magic number" that corresponds to exact atom and ligands number with specific electronic and chemical stability, such as $Au_{25}(SR)_{18}$, $Au_{22}(SR)_{18}$, $Au_{18}(SR)_{14}$, and $Au_{15}(SR)_{12}$. The structure, optical, and electronic properties of AuNCs varies greatly among different sizes as well as the nature of the coordination ligands. Optical properties of AuNCs were investigated by various spectroscopic technique[13-18], and ultrafast spectroscopy has been employed to understand the excitation states of various AuNCs by lots of groups [19-23]. The influence of charge-state on the cluster was studied by transient absorption spectroscopy, and interesting correlation between the core-gold and shell-gold relaxation was observed. Kamat's group has been studied the glutathione-stabilized $Au_{25}(SR)_{18}$, and an emission maximum at 600 nm and a lifetime of 780 ns has been characterized[23]. Instead of very weak luminescence in visible to near-infrared(NIR) region of most water-soluble AuNCs, $Au_{22}(SG)_{18}$ showed very intense red-emission with a typical quantum yield (QY) of ~ 15% [24]. The red-emitting $Au_{22}GSH_{18}$ could provide a good opportunity for understanding unresolved luminescence fundamentals of thiolated Au NCs. However, less studies have been carried out on the $Au_{22}(SG)_{18}$for the excited states study, and their charger transfer ability. Herein we use ultrafast (femtosecond) transient absorption spectroscopy (fsTA) and nanosecond transient absorption spectroscopy (nsTA) to investigate the excited state behavior of glutathione-protected clusters; $Au_{22}(SG)_{18}$, and $Au_{18}(SG)_{14}$. By introducing methyl viologen (MV^{2+}) as a probe molecule, we have succeeded in determining the electron donor ability of AuNCs and the electron transfer process between excited metal clusters and MV^{2+}.

Section 4.2 Experimental details

Section 4.2.1 Au nanoclusters synthesis

The red-emitting Au NCs were synthesized by a pH-mediated $NaBH_4$ reduction method[24]. In a typical synthesis, aqueous solutions of $HAuCl_4$ (12.5 mL, 20 mM) and GSH (7.5mL, 50 mM) were added to a 500-mL flask containing 180 mL of ultrapure water. After 2 min of vigorous stirring, the pH of the reaction solution was brought to 12.0 with 1 M NaOH. Thereafter, 0.24 mg $NaBH_4$ in 0.1 mL water was added into the reaction solution, stirring at 500 rpm at room temperature. After 0.5 h, the solution pH was adjusted to 2.5 with 0.33 M HCl. The reaction solution was then sealed airtight and slowly stirred at 200 rpm for 8 h. An aqueous solution of strong red-emitting Au NCs was formed. To isolate Au NCs from the solution, isopropyl alcohol was added with 1:1 volume ratio. The dark red precipitate was collected through high speed centrifugation at 14000 rpm and washed with 1:1 methanol: H_2O mixture. Polyacrylamide gel electrophoresis (PAGE, 30 wt% monomers) was then applied to separate and collect $Au_{22}(SG)_{18}$ from $Au_{15}(SG)_{13}$ and $Au_{18}(SG)_{14}$.

Native Polyacrylamide Gel Electrophoresis (PAGE) separation of the as-synthesized Au NCs. Native PAGE was carried out on a Hoefer SE 600 system. The electrophoresis buffer was made of 192 mM glycine and 25 mM tris(hydroxymethyl)aminomethane. Stacking and resolving gels were prepared from 4 and 30 wt% acrylamide monomers (19:1 = monomer: crosslinker), respectively. 40 μL sample solutions (1 mg/mL crude Au NCs in 8 vol% glycerol aqueous solution) were loaded into the wells of the stacking gel. The electrophoresis was allowed to run for ~5 h at a constant voltage of 250 V at room temperature. The bands containing different-sized Au NCs were individually cut, crushed, and sonicated in ultrapure water for 20 min to allow the NCs in the gels to diffuse out. The resulting solutions were then filtered by use of a filter with 0.45 μm pore size, followed by adjusting the pH to 3.0. Methanol was then added into the solution gradually and the precipitate was collected as powders. The yield of individual NC species based on the Au atoms in the starting Au precursors was determined from inductively coupled plasma (ICP-MS) measurements.

Section 4.2.2 Au nanoclusters characterization

Optical Characterization: The ultraviolet-visible (UV-vis) spectra of AuNCs were obtained *via* a Shimadzu UV3101PC UV-Vis-NIR Spectrophotometer with an integrating sphere. Photoluminescence spectra were taken in a confocal fluorescence spectroscope based on a Horiba LabRAM HR system. Solution phase photoluminescence (PL) measurements were taken using a Horiba Jobin-Yvon Fluorolog steady-state spectrofluorometer. The time-resolved PL(trPL), solutions of AuNCs dissolved in water were secured in an N_2-gas filled cell. The samples were excited in an epifluorescence scheme. The second harmonic of the output of a Coherent RegA amplifier seeded by a Coherent Mira oscillator was used as the 405 nm excitation source. The instrument response is around ~30 ps, and the measurement time window is to 10 μs.

Electrospray ionization mass spectrometry (ESI-MS) was carried out to determine the molecular formula of as-synthesized nanocluster. Electrospray ionization time-of-flight (ESI-TOF) mass spectra were obtained from a Waters Q-TOF Premier instrument (Milford, MA). The samples were directly injected into the chamber with electrospray emitters. The emitter tip is positioned ~ 5 mm from the instrument entrance in a Z-spray configuration, and a 0.127 mm diameter platinum

wire is inserted into the emitter to contact with the solution. Typical instrument parameters: capillary voltage, 0.8 -1.3 kV; m/z range, 100 – 4000. Nanocluster ions are detected in both positive and negative ion modes. The mass of the nanocluster ions is determined based on the isotopic distribution. The charger state (z) of an ionized AuNCs could be determined by $1/\Delta(m/z)$, if the isotopic peak spacing is $\Delta(m/z)$. As for the molecular weight of the ionized AuNCs equals $(m/z) \times z$. If the simulated isotope pattern does not perfectly match with the experimental data, the molecular formula needs to be re-assigned until they match perfectly.

Section 4.2.3 Femtosecond and nanosecond transient absorption setup

Femtosecond and Nanosecond Transient Absorption: Femtosecond TA spectra (fsTA) were obtained using an Ultrafast Systems Helios TA system with a Coherent Libra amplified Ti:sapphire laser system and Coherent optical parametric amplifier (OPA) pump/probe source. Solutions of neutral or anionic clusters in 1 mm path length cuvettes are resonantly excited by the tunable output of the OPA (pump). Briefly, the samples were excited with ~50fs laser pulses generated by the OPA at a repetition rate of 1 kHz. TA spectra were obtained by time delaying a broadband supercontinuum probe pulse that is overlapped in time and space with the femtosecond pump pulse. The supercontinuum is produced by focusing a small portion of the amplified laser fundamental into a sapphire plate. Multiwavelength TA spectra were recorded using dual spectrometers (signal and reference) equipped with fast Si array detectors. In all experiments, the fluence value was calibrated, varying from 75 nJ/cm^2 to 600 nJ/cm^2 for the power-dependent studies, and fixed at 400 nJ/cm^2 to rule out effects from exciton–exciton annihilation. During the experiments, all the samples were continuously stirred by a magnetic bar coated by Teflon and ultraviolet–visible absorption remained the same before and after the femtosecond experiments.

Nanosecond transient absorption(nsTA) measurements were conducted using the same ultrafast pump pulses along with an electronically delayed supercontinuum light source with a sub-nanosecond pulse duration (EOS, Ultrafast Systems).

TA Data Processing: The differential absorbance (ΔA) as a function of wavelength (λ) and time delay (t) is analyzed using a commercial global fitting procedure (Surface Explorer Pro). Spectral chirp in the fsTA is corrected using the time zero values (t_0) extracted from fitting the coherent response of the bare solvent. Singular value decomposition was applied to estimate the number of time constants needed to fit the data. Single-wavelength kinetic data are fit to a multiexponential decay law ($y = A + a_1e^{-t/t1} + a_2e^{-t/t2} + ...$). To analyze the coherent phonon response of the system, a Fourier transform of the kinetic data at each wavelength was calculated.

Section 4.3 Results and discussion

Section 4.3.1 Ultrafast excited states of $Au_{22}(SG)_{18}$

To investigate the optical property, the UV-vis absorption spectrum of as synthesized $Au_{22}(SR)_{18}$ in Fig. 4.1a shows the significant characteristic absorption peak at 515 nm, which is attributed to the $Au_{22}(SR)_{18}$ from previous studies. The broad absorption peak is distinct from the gold nanoparticles with surface plasmon resonance. The resulting photoluminescence spectrum in

Fig. 4.1b shows the strong red emission centered at 630 nm with the 405nm laser as the excitation wavelength. Electrospray ionization mass spectrometry (ESI-MS) was then used to determine the molecular formula of as synthesized $Au_{22}(SR)_{18}$. As shown in Fig. 4.2, the main base peak was at m/z 1968.47 in the resulting zoomed-in spectrum. Isotope pattern analysis of the 1968.47 peak is shown in the insert with isotope spacing = 0.2, indicating that the ionized NCs carried five units of negative charge. Therefore, the molecular weight of the NCs was 9842.35 Da (1968.47 × 5), which is consistent with the molecular formula of $[Au_{22}(SG)_{18}^{0} - 5H]^{5-}$ (molecular weight of 9841.6 Da).

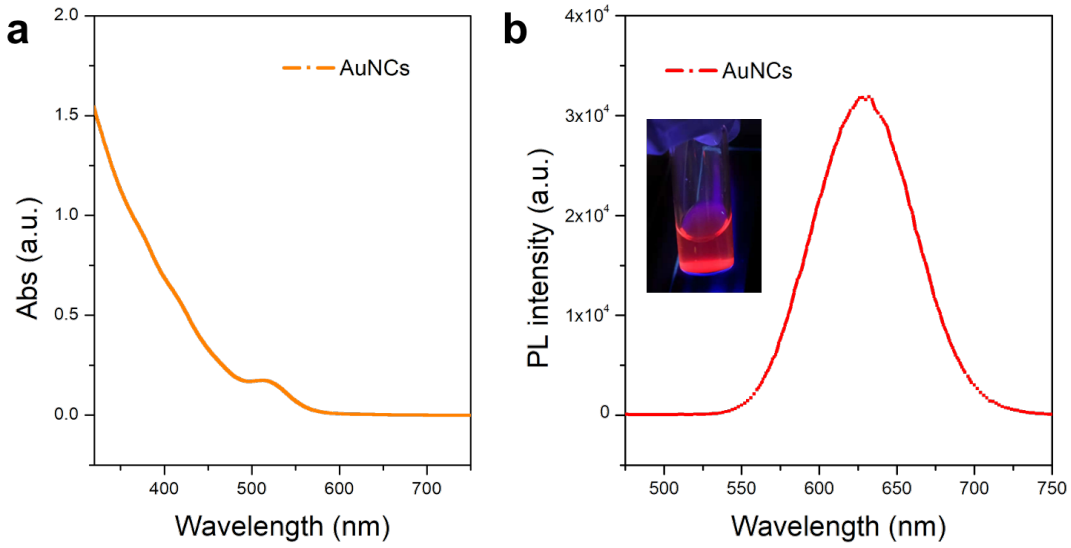

Fig. 4.1. Optical properties of $Au_{22}(SR)_{18}$. a. UV-Vis absorption and the photoemission spectrum(**b**) of $Au_{22}(SR)_{18}$. (Insets) Digital photos of the raw product dissolved in water under UV light.

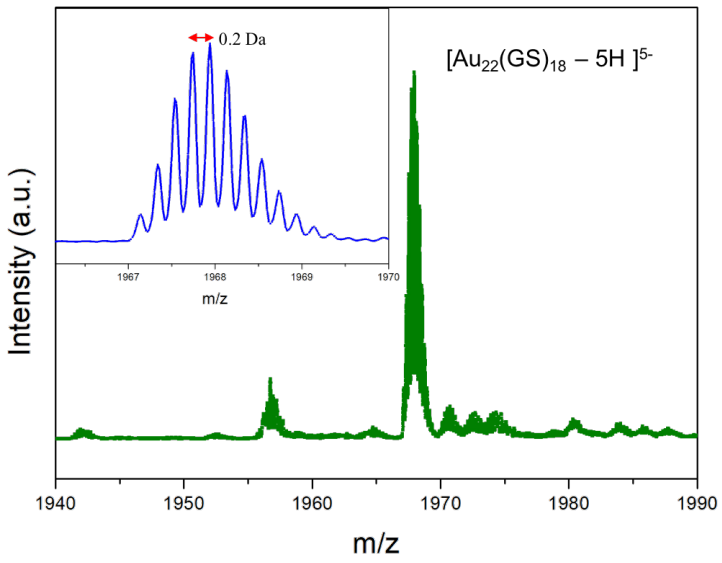

Fig. 4.2. Electrospray ionization mass spectrometry (ESI-MS) spectrum of $Au_{22}(GS)_{18}$. The insert lines are the isotope pattern of $[Au_{22}(GS)_{18}{}^{0} - 5H]^{5-}$.

The lifetime of $Au_{22}(SR)_{18}$ has been carried out to further understand the clusters' physical property, and the 405 nm laser was used as the excitation wavelength to profile the time-resolved PL spectrum at 630 nm. Fit by exponential equation, the non-radiative decay and radiative decay process is extremely long to 67 ns and 729 ns, respectively (Fig. 4.3).

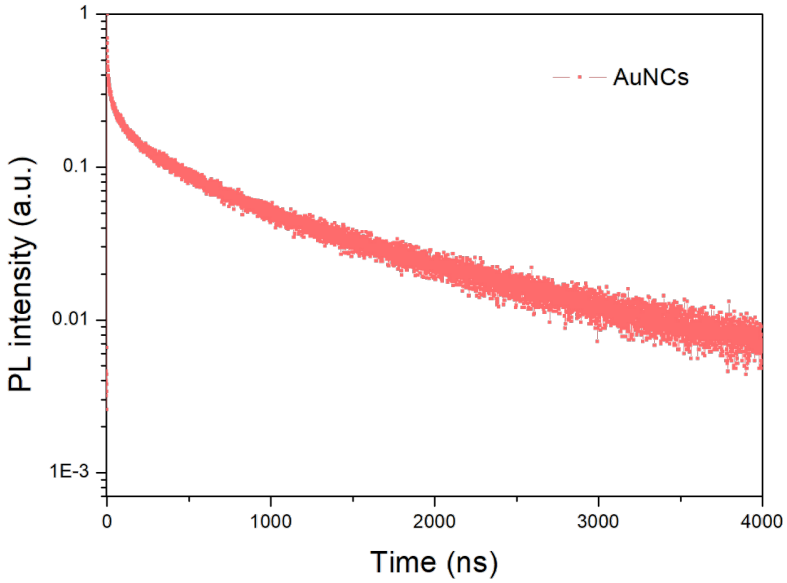

Fig. 4.3. The time-resolved PL spectrum of $Au_{22}(SR)_{18}$ at 630 nm. The spectrum is fit by biexponential equations, including 67 ns and 729 ns two components.

The time-dependent change in absorbance (ΔA) of solution was monitored after a 350 nm laser (laser power = 400 nJ) excitation to determine the excited states of $Au_{22}(SR)_{18}$. The $Au_{22}(SR)_{18}$ solution was degassed with N_2 and placed in a 2 mm path length quartz cuvette for both fsTA and nsTA measurements, and was continuously stirred by a magnetic bar to avoid the power heating during the experiments. In the transient absorption map, the positive signal and negative signal present the excited-state absorption (ESA) and ground-state bleach (GSB), respectively. The fsTA was first carried out to study the ultrafast excited-states dynamics of $Au_{22}(SR)_{18}$. As shown in Fig. 4.4a, the difference absorption spectra spanning over the broad visible range from 400-800 nm overlapped with GSB signals that correspond to its steady-state absorption spectrum shown in Fig. 4.1b. Interesting, the previous studies on $Au_{25}SR_{18}$ demonstrate a short lived excited states ($t < 5$ ps) and a longer lifetime component ($t > 2$ns)[25]. These two components are attributed to the metal-metal transition in the core structure, and ligand-to-metal transfer. Whereas, the transient absorption of $Au_{22}(SR)_{18}$ remains unperturbed at early times, suggesting no short-lived transient happening in these measurements (Fig. 4.4b). The similar difference absorption spectra recorded immediately, 50 ps, 100 ps, and 500 ps after 350 nm excitation prove that the excited state of $Au_{22}(SR)_{18}$ is dominated exclusively by a long-lived transient. The absorption-time profile at different wavelength (i.e. 500 nm, 600 nm, and 650 nm) have been plotted to analysis the possible lifetime of excited states in Fig. 4.5, and as indicated, showing no significant decay over the time scale of the experiments.

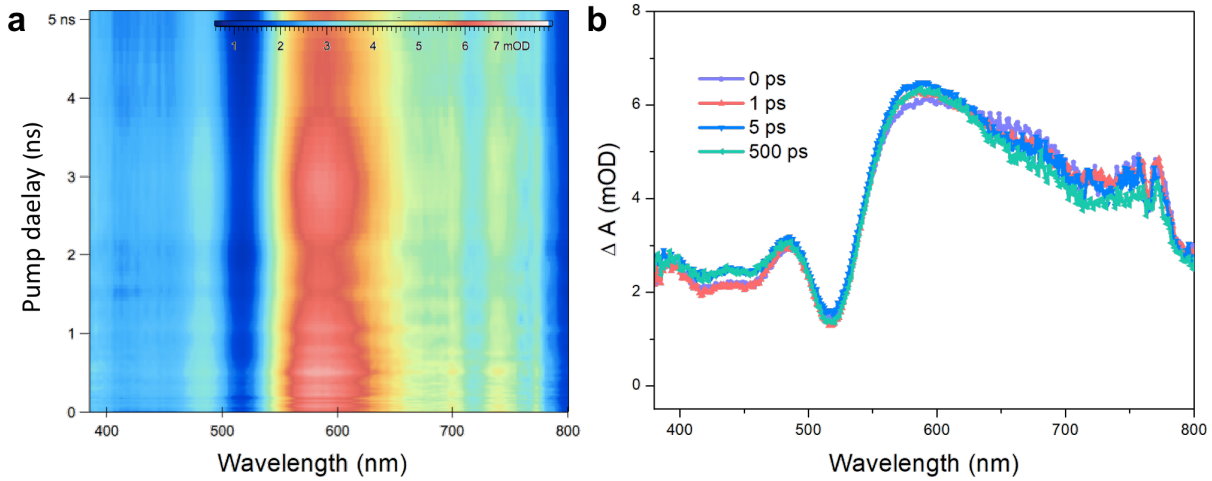

Fig. 4.4. The fsTA spectra mapping. **a.** The TA mapping in 0-5 ns time window, depicting the ESA in broad visible range. **b.** Similar spectra of TA recorded at 0, 50 ps, 100 ps, and 500 ps.

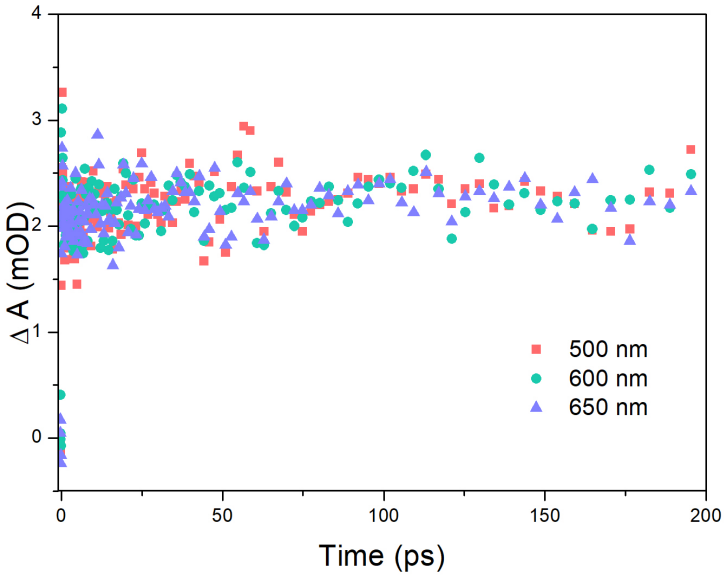

Fig. 4.5. Absorption-time profile at different wavelength. The decay profile recorded at 500 nm, 600 nm, and 650 nm within 200 ps.

This long-lived excited state (>2 ns), which is too long to be resolved in fsTA measurements, was probed in the nsTA measurements with a 350 nm laser excitation. The detection time window is extent to 8 μs. Generally, for the Au nanoparticles of 10-100 nm diameter with plasmonic behavior, the photoexcited electrons undergo fast relaxation *via* electron-electron scattering (~ 100 fs), and then followed by electron-phonon coupling (1-5 ps) and heat dissipation into the environment (10-100 ps)[21,25]. The two-temperature model is general used to describe the electron dynamics of metal nanoparticles, where the electron-phonon (e-p) coupling slows down with pump fluence increases. Jin and co-workers have synthesized Au nanoparticles with different sizes and mapped out three distinct states: metallic, transition regime, and nonmetallic (or excitonic state) based on the pump-power-dependent electron dynamics of gold nanoparticles. The e–p coupling time increases more dramatically with increasing pump fluences for larger gold nanoparticles. By contrast, the molecular-like AuNCs (i.e. Au_{144}) behaves power insensitive, which could be described by exciton relaxation. Based on such theory, the pump power-dependent experiments have been carried out on the $Au_{22}(SR)_{18}$ samples, ranging from 75 nJ/cm^2 to 600 nJ/cm^2. Normalized decay-kinetics at 600 nm under different pump power maintain the same with each other, and raising the pump power will not alter the excited state dynamics (Fig. 4.6). More excitons were generated with increased pump power, implying the molecular-like property of $Au_{22}(SR)_{18}$.

The nsTA spectral features of ΔA probed within 400 ns under 400 nJ/cm^2 pump power are consistent with the steady-state absorption and fsTA. The absorption-time profile monitored at 600 nm was fit to a biexponential kinetic expression and gives a lifetime of 361 ± 21.8 ns, confirming the dominance of ligand-to-metal charge transfer process (Fig. 4.7). Such long-lived excited states make AuNCs attractive in terms of photocatalysts and photoelectrochemistry. One typical example that using AuNCs as the sensitizer for TiO_2 solar cell, demonstrates the ability of AuNCs converting photons to electrons with high conversion efficiency[5].

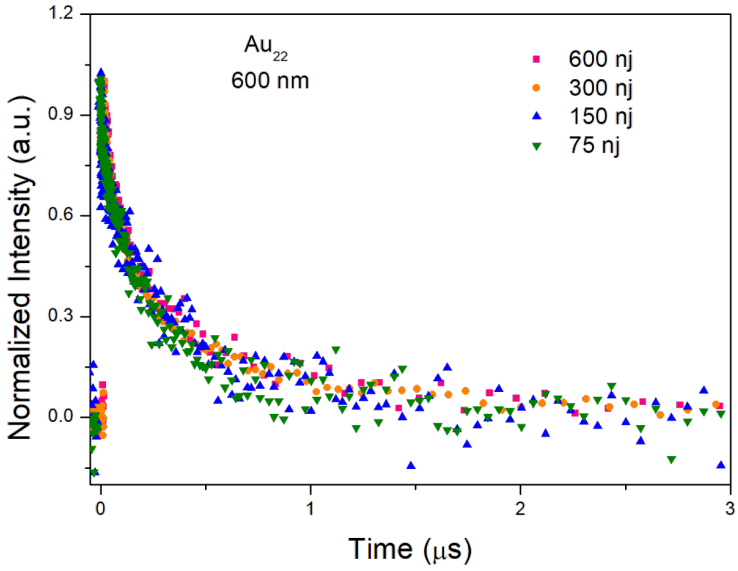

Fig. 4.6. Pump power-dependent electron dynamics of $Au_{22}(SR)_{18}$ power dependent spectra.

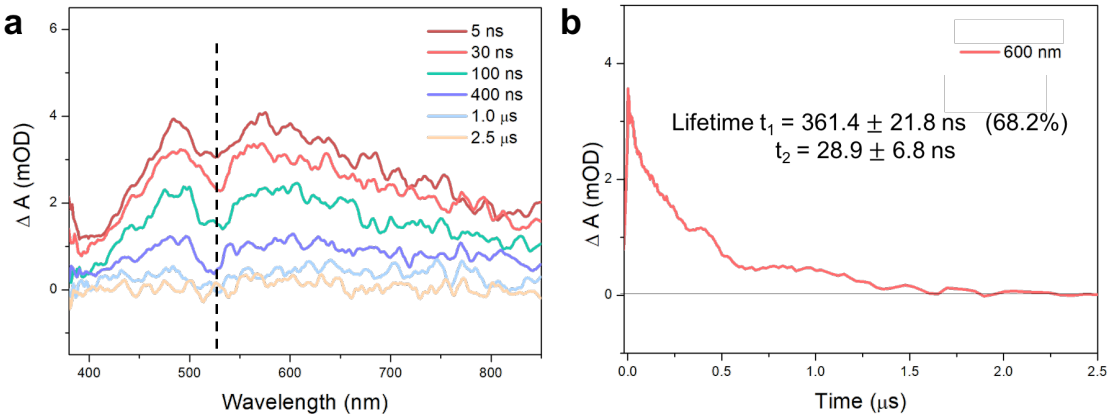

Fig. 4.7. $Au_{22}(SR)_{18}$ nsTA spectra. **a.** the nsTA spectra recorded at different time points after the laser excitation. **b.** The absorption-time profile probed at 600 nm with the fit lifetime, 361 ns and 28.9 ns.

Section: 4.3.2 Photoinduced electron transfer within $Au_{22}(SR)_{18}$

AuNCs were proposed the possibility for the photochemistry application, including dye-sensitized-solar-cell, photoanode for water splitting, and the forth[4-8]. Therefore, AuNCs are regard as the photoinduced electron donors and capable of transferring electron to reduce other species.

In the model system, methyl viologenare (MV^{2+}) is used as an electron donor[26,27], which could probe the electron-donating ability of AuNCs. Upon reduced MV^{2+} to $MV^{+\bullet}$ radicals, the rising absorption peaks at 394 nm and 605 nm affirm the successful charge transfer process during laser pulse excitation. As the scheme depicted in Fig. 4.8, the reduction of MV^{2+} to $MV^{+\bullet}$ radicals is a fast reaction, whereas the back reaction from $MV^{+\bullet}$ to MV^{2+} is very slow. Moreover, the yield of generated $MV^{+\bullet}$ could reflect the efficiency of the charge transfer, which provide a convenient tool to evaluate the photocatalytic activity.

The nsTA map shown in Fig. 4.9 presents the absorption-time profile within 8 μs after 350 nm laser pulse excitation of a deaerated solution of bare $Au_{22}(SR)_{18}$ and $Au_{22}(SR)_{18}$ with 0.1 mM MV^{2+}. The appearance of absorption bands at 394 nm and broad ESA centered at 605 nm confirm the formation of $MV^{+\bullet}$ during the decay of excited states. The blank control of MV^{2+} and glutathione mixture under the same pulse condition has been carried out, and no any noticeable $MV^{+\bullet}$ radicals have been observed. Hence, the photoinduced excited states of $Au_{22}(SR)_{18}$ involve the MV^{2+} reduction process, indicating its ability of electron-donating property. Furthermore, the absorption-time profile recorded at 394 nm of $Au_{22}(SR)_{18}$ and $Au_{22}(SR)_{18}$ with 0.1 mM MV^{2+} points out the growth of transient absorption, and the growth kinetics contribute the positive ΔA over 8 μs, which agrees well with the long lifetime of $MV^{+\bullet}$ radicals. Varying the MV^{2+} concentration, the concentration of formed radicals could be calculated. The initial MV^{2+} concentration changes from 0.8 to 1.1 mM, and these three systems all reveal the formation of $MV^{+\bullet}$ radicals in Fig. 4.10. Combined the absorption-time profiles at 394 nm, more detailed charge transfer kinetics could be elucidated.

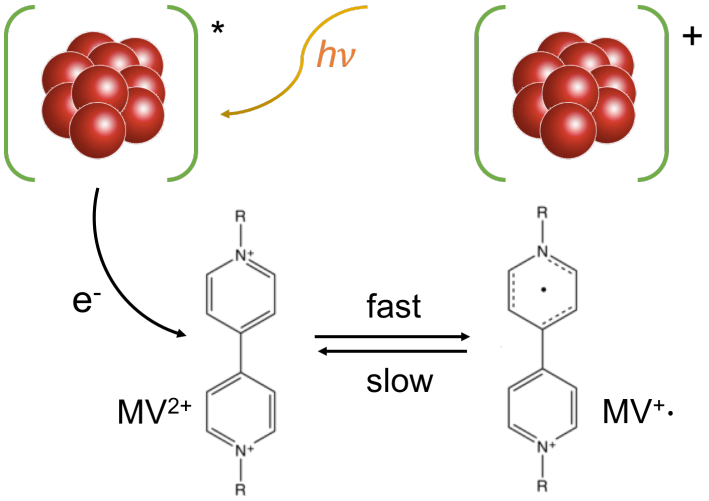

Fig. 4.8. The scheme of possible electron transfer process between AuNCs and MV^{2+}, where pumped electron from AuNCs could reduce MV^{2+} to its reduce format $MV^{+\bullet}$.

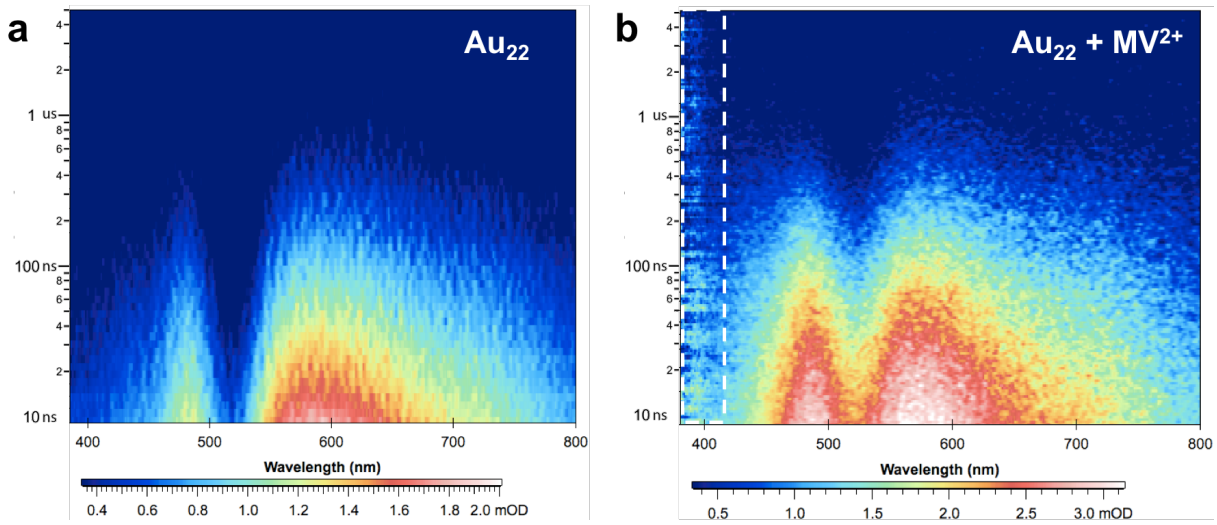

Fig. 4.9. nsTA map of $Au_{22}(SR)_{18}$ and $Au_{22}(SR)_{18}$ with MV^{2+} systems. The generation peak of $MV^{+\bullet}$ at 394 nm (**b**) was clearly detected in the presence of MV^{2+}, indicating the successful charge transfer process between $Au_{22}(SR)_{18}$ and MV^{2+}.

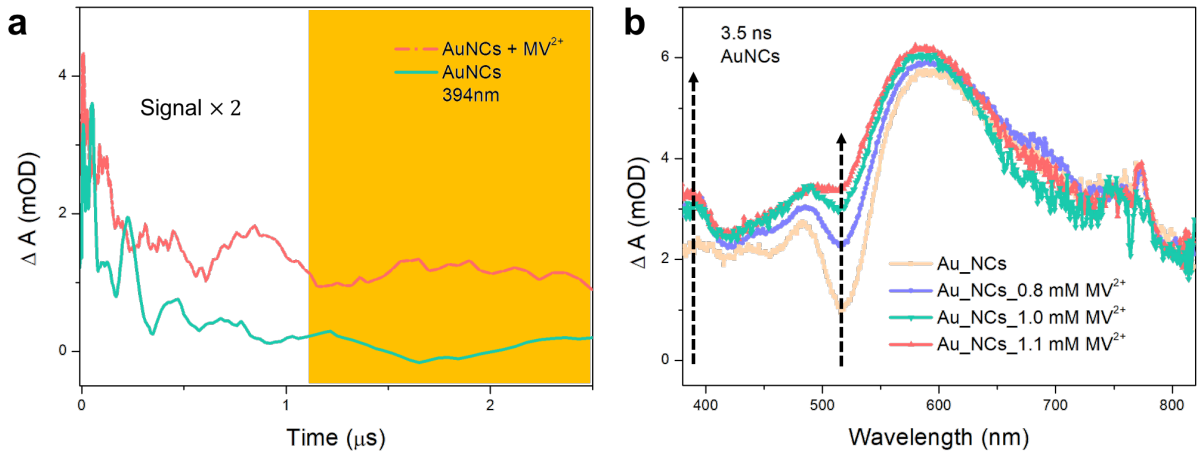

Fig. 4.10. nsTA spectra of $Au_{22}(SR)_{18}$ and MV^{2+} systems. **a.** The absorption-time profile at 394 nm of bare $Au_{22}(SR)_{18}$ and $Au_{22}(SR)_{18}$-MV^{2+}. **b.** nsTA spectra of $Au_{22}(SR)_{18}$ with various MV^{2+} concentration probed after 3.5 ns

Section 4.3.3 Excited states properties of $Au_{18}(SR)_{14}$

As discussed above, $Au_{18}(SR)_{14}$ is also a good candidate for most photochemistry reactions. Therefore, studying the $Au_{18}(SR)_{14}$ could obtain more insights on the structure effects of AuNCs. Different from $Au_{22}(SR)_{18}$, $Au_{18}(SR)_{14}$ is composed with 18 Au atoms and 14 glutathione, with greenish color. Due to the possible different structure, $Au_{18}(SR)_{14}$ is a non-emissive cluster with little understanding. People have proposed the possible structures for $Au_{22}(SR)_{18}$ and $Au_{18}(SR)_{14}$ with the analysis of X-ray absorption XANES and EXAFS, and the most reasonable structure for

$Au_{22}(SR)_{18}$ is a Au_8 core protected by two trimeric and two tetrameric staple motifs, simplify as $Au_{22}(SR)_{18}$ = Au_8 + 2 [$RS(AuSR)_3$] + 2 [$RS(AuSR)_4$]. As for Au18 stabilized by 14 (SC_6H_{11}) ligands, they have Au_9 bi-octahedral kernel that protected by dimeric and tetrameric staple motifs[28].

We further probed the long-lived excited states deactivation of $Au_{18}(SR)_{14}$ using nsTA measurements with a 350 nm laser at 400 nJ/cm^2. Interesting, the long-time component of $Au_{18}(SR)_{14}$ at 600 nm is around 240 ± 18.2 ns, which is a little bit faster compared to $Au_{22}(SR)_{18}$. From the TA map in Fig. 4.11b, $Au_{18}(SR)_{14}$ behaves a large portion of ESA and no significant GSB. All these physical behaviors reveal the structure information, providing the possibility to study the size and structure dependent effects of AuNCs library. The electron-donating property was also observed in the $Au_{18}(SR)_{14}$ and MV^{2+} system. The absorption-time profile of $Au_{18}(SR)_{14}$ with 0.1 mM MV^{2+} in Fig.4.11 displays the first 8 μs decay spectrum after laser pulse excitation. Compared with the bare $Au_{18}(SR)_{14}$, where a broad peak at around 394 nm is from the ligands-to-metal transition, the mixture system with MV^{2+} turned out a sharp and longer lived excited state at 394 nm. Hence, the photoinduced excited states of $Au_{18}(SR)_{14}$ could reduce MV^{2+} to its radical format, confirming its electron-donating ability. Furthermore, the absorption-time profile recorded at 394 nm of $Au_{18}(SR)_{14}$ and $Au_{18}(SR)_{14}$ with 0.1 mM MV^{2+} points out the growth of transient absorption, and the growth kinetics contribute the positive ΔA over 8 μs, which agrees well with the long lifetime of $MV^{+\bullet}$ radicals(Fig.4.11c).

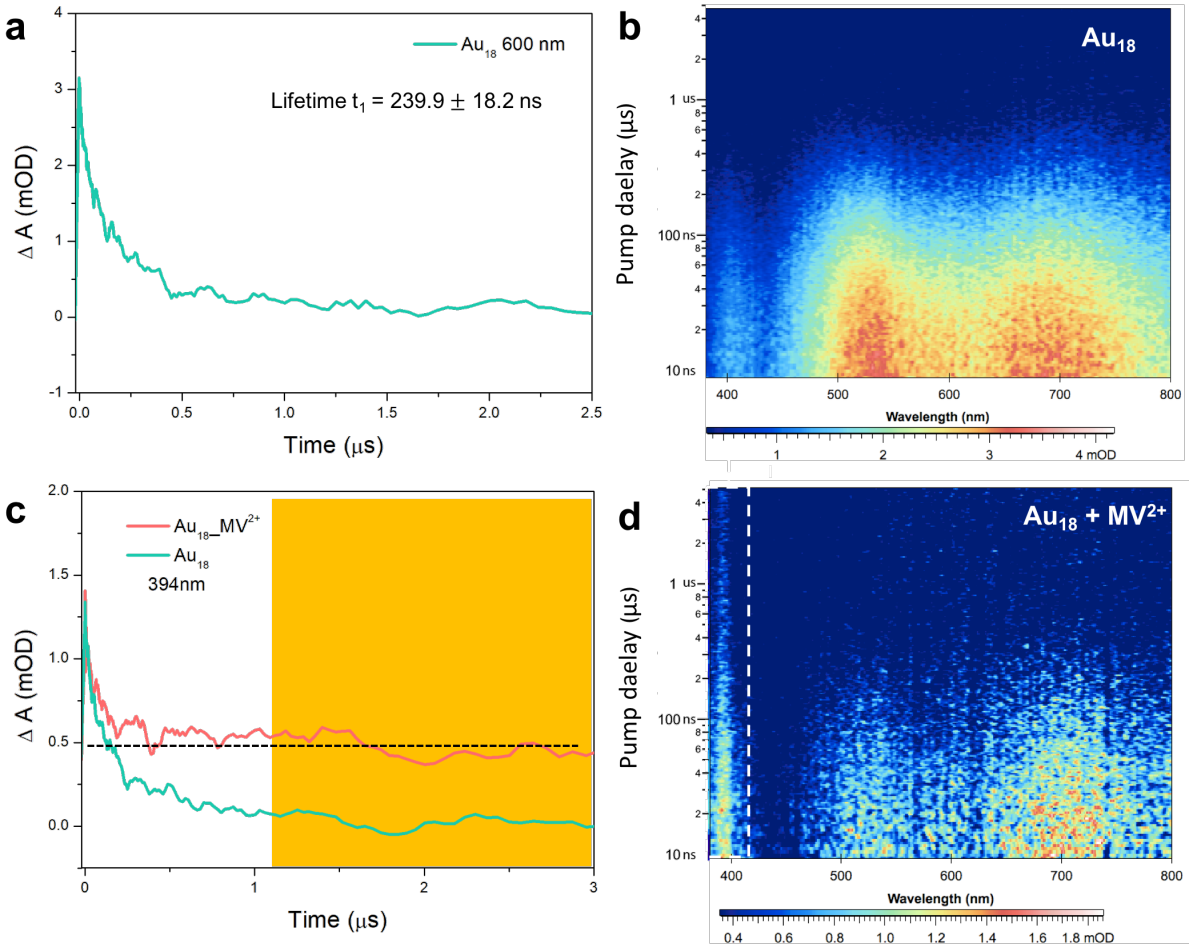

Fig. 4.11. nsTA spectra of $Au_{18}(SR)_{14}$. a. The absorption-time profile of bare $Au_{18}(SR)_{14}$ recorded at 600 nm, with the lifetime fit to 240 ns. **b.** The nsTA map of bare $Au_{18}(SR)_{14}$ with broad ESA in visible range. **c.** The absorption-time profile comparison of bare $Au_{18}(SR)_{14}$ and $Au_{18}(SR)_{14}$ with MV^{2+} recorded at 394 nm, showing a sharp and longer lived absorption(**d**).

Section 4.4 Conclusions

The emerging glutathione-stabilized $Au_{22}(SR)_{18}$ and $Au_{18}(SR)_{14}$ have been studied in terms of the excited states and electron-donating properties, and different size and structure could result in various excited states dynamics. Both $Au_{22}(SR)_{18}$ and $Au_{18}(SR)_{14}$ exhibit strong ESA and that matches with their static-state absorption, and the long-lived components in the excited states decay was confined as ~240 ns and ~361 ns for $Au_{18}(SR)_{14}$ and $Au_{22}(SR)_{18}$, respectively. The photoactivities of these AuNCs in reducing MV^{2+} have been verified, which yields the high potential for them as a sensitizer for light harvesting. Therefore, changing the size and ligands brings more opportunities to obtain insights on excited states properties of AuNCs, and high quantum yield for electron transfer with strong visible light absorption could be optimized with such understanding. The numerous emerging AuNCs extends the applications in photochemistry and photocatalysts serving as the sensitizers with tunability.

Section 4.5 References

1. Zhao, Shuo, *et al.* "Gold nanoclusters promote electrocatalytic water oxidation at the nanocluster/$CoSe_2$ interface." *J. Am. Chem. Soc.* **139.3.** 1077-1080 (2017).
2. Green, T. D, *et al.* Temperature-dependent photoluminescence of structurally precise quantum-confined $Au_{25}(SC_8H_9)_{18}$ and $Au_{38}(SC_{12}H_{25})_{24}$ metal nanoparticles. *J. Phys. Chem. A*. **118,** 10611−10621 (2014).
3. Zeng, C., Chen, Y., Kirschbaum, K., Appavoo, K., Sfeir, M. Y., & Jin, R. Structural patterns at all scales in a nonmetallic chiral $Au1_{33}(SR)_{52}$ nanoparticle. *Sci. Adv*. ***1*(2),** e1500045 (2015).
4. Sakai, N., Tatsuma, T. Photovoltaic properties of glutathione protected gold clusters adsorbed on TiO_2 electrodes. *Adv. Mater*. **22**, 3185−3188 (2010).
5. Chen, Y.S., Choi, H., Kamat, P. V. Metal cluster sensitized solar cells. a wew class of thiolated gold sensitizers delivering efficiency greater than 2%. *J. Am. Chem. Soc*. **135**, 8822−8825 (2013).
6. Stamplecoskie, K. G., Swint, A. Optimizing molecule-like gold clusters for light energy conversion. *J. Mater. Chem. A*. **4**, 2075−2081 (2016).
7. Yu, C.; Li, G., Kumar, S., Kawasaki, H., Jin, R. Stable $Au_{25}(SR)_{18}/TiO_2$ composite nanostructure with enhanced visible light photocatalytic activity. *J. Phys. Chem. Lett*. **4**, 2847−2852 (2013).
8. Stamplecoskie, K. G., Kamat, P. V. Size-dependent excited state behavior of glutathione-capped gold clusters and their light harvesting capacity. *J. Am. Chem. Soc.* **136,** 11093−11099 (2014).

9. Liu, S., Xu, Y. J. Photo-induced transformation process at gold clusters-semiconductor interface: Implications for the complexity of cold clusters-based photocatalysis. *Sci. Rep.* **6,** 22742 (2016).
10. Aikens, C. M., Li, S., & Schatz, G. C. From discrete electronic states to plasmons: TDDFT optical absorption properties of Ag_n (n = 10, 20, 35, 56, 84, 120) tetrahedral clusters. *J. Phys. Chem. C*, ***112*(30),** 11272-11279 (2008).
11. Aikens, C. M. Electronic structure of ligand-passivated gold and silver nanoclusters. *J. Phys. Chem. Lett.* ***2*(2),** 99-104 (2010).
12. Yau, S. H., Varnavski, O., & Goodson III, T. An ultrafast look at Au nanoclusters. *Acc. Chem. Res.* ***46*(7),** 1506-1516 (2013).
13. Devadas, M. S. *et. al.* Temperature Dependent Optical Absorption Properties of Monolayer-Protected Au_{25} and Au_{38} Clusters. *J. Phys. Chem. Lett*. **2**, 2752−2758 (2011).
14. Varnavski, O., Ramakrishna, G., Kim, J., Lee, D., & Goodson, T. Critical size for the observation of quantum confinement in optically excited gold clusters. *J. Am. Chem. Soc.* ***132*(1),** 16-17 (2009).
15. Miller, S. A., Womick, J. M., Parker, J. F., Murray, R. W., Moran, A. M. Femtosecond relaxation dynamics of $Au_{25}L_{18}$ - monolayer protected clusters. *J. Phys. Chem. C.* **113,** 9440−9444 (2009).
16. Miller, S. A., Fields-Zinna, C. A., Murray, R. W., Moran, A. M. Nonlinear optical signatures of core and ligand electronic states in $Au_{24}PdL_{18}$. *J. Phys. Chem. Lett*. **1,** 1383−1387 (2010).
17. Devadas, M. S., Kim, J., Sinn, E., Lee, D., Goodson, T., Ramakrishna, G. Unique ultrafast visible luminescence in monolayer-protected Au_{25} clusters. *J. Phys. Chem. C.* **114,** 22417−22423, (2010).
18. Green, T. D., Knappenberger, K. L., Jr. Relaxation dynamics of $Au_{25}L_{18}$ nanoclusters studied by femtosecond time-resolved near infrared transient absorption spectroscopy. *Nanoscale,* **4,** 4111−4118 (2012).
19. Shang, L., Dong, S., & Nienhaus, G. U. Ultra-small fluorescent metal nanoclusters: synthesis and biological applications. *Nano today*, ***6*(4),** 401-418, (2011).
20. Kwak, K., Thanthirige, V. D., Pyo, K., Lee, D., & Ramakrishna, G. Energy Gap Law for Exciton Dynamics in Gold Cluster Molecules. *J. Phys. Chem. Lett.* ***8*(19)**, 4898-4905 (2017).
21. Qian, H., Sfeir, M. Y., & Jin, R. Ultrafast relaxation dynamics of $[Au_{25}(SR)_{18}]_q$ nanoclusters: Effects of charge state. *J. Phys. Chem. C.* ***114*(47),** 19935-19940 (2010).
22. Stamplecoskie, K. G., & Kamat, P. V. Size-dependent excited state behavior of glutathione-capped gold clusters and their light-harvesting capacity. *J. Am. Chem. Soc.* ***136*(31),** 11093-11099 (2014).
23. Stamplecoskie, K. G., Chen, Y. S., & Kamat, P. V. Excited-state behavior of luminescent glutathione-protected gold clusters. *J. Phys. Chem. C.* ***118*(2),** 1370-1376 (2014).
24. Yu, Yong, *et al.* Identification of a highly luminescent $Au_{22}(SG)_{18}$ nanocluster. *J. Am. Chem. Soc.* **136.4,** 1246-1249 (2014).
25. Zhou, Meng, *et al.* Evolution from the plasmon to exciton state in ligand-protected atomically precise gold nanoparticles. *Nature comm.* **7,** 13240 (2016).
26. Peon, J., Tan, X., Hoerner, J. D., Xia, C., Luk, Y. F., Kohler, B. Excited state dynamics of methyl viologen: ultrafast photoreduction in methanol and fluorescence in ccetonitrile. *J. Phys. Chem. A*. **105,** 5768−5777, (2001).

27. Watanabe, T., Honda, K. Measurement of the Extinction Coefficient of the Methyl Viologen Cation Radical and the Efficiency of Its Formatlon by Semiconductor Photocatalysis. *J. Phys. Chem.* **86**, 2617−2619 (1982).
28. Chen, Shuang, *et al.* The structure and optical properties of the $[Au_{18}(SR)_{14}]$ nanocluster. *Angewandte.* **54.10**, 3145-3149 (2015).